UNDERSTANDING THE VAPOR-LIQUID-SOLID AND VAPOR-SOLID-SOLID MECHANISMS OF SI NANOWIRE GROWTH TO SYNTHETICALLY ENCODE PRECISE NANOSCALE MORPHOLOGY

Christopher William Pinion

A dissertation submitted to the faculty at the University of North Carolina at Chapel Hill in partial fulfillment of the requirements for the degree of Doctor of Philosophy in the Department of Chemistry in the College of Arts and Sciences.

Chapel Hill
2017

Approved by:

James Cahoon

Yosuke Kanai

Scott Warren

Joanna Atkin

Frank Leibfarth

ABSTRACT

Christopher William Pinion: Understanding the Vapor-Liquid-Solid and Vapor-Solid-Solid Mechanism of Si Nanowire Growth to Synthetically Encode Precise Nanoscale Morphology
(Under the direction of James Cahoon)

Precise patterning of semiconductor materials utilizing top-down lithographic techniques is integral to the advanced electronics we use on a daily basis. However, continuing development of these lithographic technologies often results in the trade-off of either high cost or low throughput, and three-dimensional (3D) patterning can be difficult to achieve. Bottom-up, chemical methods to control the 3D nanoscale morphology of semiconductor nanostructures have received significant attention as a complementary technique. Semiconductor nanowires, nanoscale filaments of semiconductor material ~10-500 nm in diameter and ~1-50 microns in length, are an especially promising platform because the wire composition can be modulated during growth and the high aspect ratio, one-dimensional structure enables integration in a range of devices.

In this thesis, we first report a bottom-up method to break the conventional "wire" symmetry and synthetically encode a high-resolution array of arbitrary shapes along the nanowire growth axis. Rapid modulation of phosphorus doping combined with selective wet-chemical etching enables morphological features as small as 10 nm to be patterned over wires more than 50 μm in length. Next, our focus shifts to more fundamental studies of the nanowire synthetic mechanisms. We presented comprehensive experimental measurements on the growth rate of Au catalyzed Si nanowires and developed a kinetic model of vapor-liquid-solid growth. Our analysis revealed an abrupt transition from a diameter-independent growth rate that is limited by incorporation to a diameter-dependent growth rate that is limited by crystallization.

While investigating the vapor-liquid-solid mechanism, we noticed instances of unique catalyst behavior. Upon further study, we showed that it is possible to instantaneously and reversibly switch the phase of the catalyst between a liquid and superheated solid state under isothermal conditions above the eutectic temperature. The solid catalyst induces a vapor-solid-solid growth mechanism, which provides atomic-level control of dopant atoms in the nanowire.

Finally, we explored a promising application of nanowires by investigating the potential for complex silicon nanowires to serve as a platform for next-generation photovoltaic devices. We reviewed the synthesis, electrical, and optical characteristics of core/shell Si nanowires that are sub-wavelength in diameter and contain radial p-n junctions. We highlighted the unique features of these nanowires, such as optical antenna effects that concentrate light and intense built-in electric fields that enable ultrafast charge-carrier separation. Based on these observations we advocate for a paradigm in which nanowires are arranged in periodic horizontal arrays to form ultrathin devices.

TABLE OF CONTENTS

LIST OF FIGURES ..... **ix**

LIST OF TABLES ..... **xi**

LIST OF ABBREVIATIONS ..... **xii**

CHAPTER 1: INTRODUCTION **1**

1.1 Semiconductor Nanowires 1

1.2 Nanowire Synthesis 2

1.2.1 Vapor-Liquid-Solid Mechanism 2

1.2.2 Vapor-Solid-Solid Mechanism 3

1.3 Understanding Nanowire Growth Mechanisms 4

1.4 Characterizing and Modeling Nanowire Growth 5

1.5 Controlling Nanowire Composition 5

References 8

CHAPTER 2: SYNTHETICALLY ENCODING 10-NM MORPHOLOGY IN SILICON NANOWIRES **13**

2.1 Introduction 13

2.2 Nanowire Synthesis and Etching 15

2.3 Optimization of ENGRAVE Technique 16

2.4 Applications of ENGRAVE 19

2.5 Conclusion 23

2.6 Detailed Methods 24

2.6.1 Nanowire Growth 24

2.6.2 Etching and Device Fabrication 25

2.6.3 Electron and Raman Microscopy 26

2.6.4 Finite-Element simulations 26

References 27

CHAPTER 3: IDENTIFYING CRYSTALLIZATION AND INCORPORATION LIMITED REGIMES DURING VAPOR-LIQUID-SOLID GROWTH OF SI NANOWIRES 32

3.1 Introduction 32

3.2 Experimental Design 36

3.3 Results 38

3.4 Kinetic Modeling 41

3.5 Analysis and Discussion 45

3.6 Conclusions 49

3.7 Detailed Methods 50

3.7.1 Nanowire Growth 50

3.7.2 Image Analysis 51

3.8 Derivation of Nanowire growth rate 51

3.9 Growth Rate Data 55

References 62

CHAPTER 4: INSTANTANEOUS SWITCHING BETWEEN A LIQUID AND SUPERHEATED SOLID CATALYST DURING NANOWIRE GROWTH 66

4.1 Introduction 66

4.2 Experimental 67

4.3 Analysis, Thermodynamic Modeling, and Discussion 74

4.4 Conclusion 80

4.5 Detailed Methods 81

4.5.1 Nanowire Growth and Etching 81

4.5.2 Electron Microscopy and Elemental Mapping 81

4.6 Thermodynamic Model of Catalyst-Nanowire System 82

4.7 Thermodynamic Model of Catalyst Solidification 83

4.8 Thermodynamic Model of Catalyst Liquefaction 84

References 85

CHAPTER 5: HORIZONTAL SILICON NANOWIRES WITH RADIAL P-N JUNCTIONS: A PLATFORM FOR UNCONVENTIONAL SOLAR CELLS 88

5.1 Introduction 88

5.2 Experimental 92

5.3 Analysis and Discussion 96

5.4 Conclusion 105

5.5 Detailed Methods 105

5.5.1 Hexagonal 2D Electrostatics Finite-Element Modeling 105

5.5.2 Optical Simulations 106

5.5.3 Si Nanowire growth 107

5.5.4 Device fabrication 107

5.5.5 Device measurements 108

References 110

CHAPTER 6: CONCLUSION 114

6.1 Summary 114

6.2 Future Work 115

6.2.1 Morphology Control: Si-Ge Heterostructures & Dry Etchants 115

6.2.2 Technological Applications: Si NW Thermoelectrics 116

References 119

LIST OF FIGURES

Figure 1.1 Au-Si Binary Phase Diagram 2

Figure 2.1: Synthesis of Si NWs with encoded morphology 15

Figure 2.2: Characterization of NW growth, etching, and morphology 17

Figure 2.3: SEM images and phosphine flow profiles for the synthesis of Si NWs with complex morphology 19

Figure 2.4: Nanogap-encoded NWs for plasmonics 21

Figure 2.5: Nanorod-encoded NWs for non-volatile memory 23

Figure 3.1: VLS growth of Si NWs by CVD 34

Figure 3.2: Determination of Si NW VLS growth rates using dopant modulation 37

Figure 3.3: Temperature-dependent Si NW VLS growth rates 38

Figure 3.4: Diameter-dependent Si NW VLS growth rates 40

Figure 3.5: Si NW growth rates at 390 ^{o}C for various partial pressures. 41

Figure 3.6: The kinetics and energetics of VLS NW growth. 43

Figure 3.7. Identification of crystallization-limited and incorporation-limited regimes during VLS NW growth. 46

Figure 3.8. Catalyst morphology and contact angle at 420 ^{o}C and 480 ^{o}C. 48

Figure 3.9: Growth rate vs. temperature for a variety of NW diameters 55

Figure 3.10: Histograms of growth rate data for various synthetic conditions 57

Figure 4.1: Reversible switching of catalyst phase under isothermal conditions above T_{eu} 69

Figure 4.2: Evidence of a solid catalyst and VSS mechanism above T_{eu} 71

Figure 4.3: Mechanism of catalyst solidification and liquefaction 73

Figure 4.4: Absence of SLV etching under hydrogen atmosphere 76

Figure 4.5: Catalyst liquefaction and sub-eutectic NW growth from surface chlorination 79

Figure 5.1: Overview of geometries used for semiconductor p-n junction PV devices 89

Figure 5.2: Overview of the general strategy for development of NW PV devices that use radial Si p-n junctions as the charge-separating scaffold for advanced solar cell architectures 92

Figure 5.3: Time-scale of carrier separation in radial p-i-n devices 94

Figure 5.4: Synthesis and characteristics of core/shell p-i-n junction Si NWs 95

Figure 5.5: Performance of single core/shell p-i-n Si NW photovoltaic devices 97

Figure 5.6: Optical absorption characteristics of individual Si NWs 99

Figure 5.7: Absorption efficiency spectra of single NWs demonstrating EQE values greater than unity as a result of the optical antennae effect and effect of cross-sectional shape on NW absorption properties. 100

Figure 5.8: Optical absorption characteristics of extended arrays of Si NWs 102

Figure 5.9: Concepts for PV devices using more complex nanostructures based on a Si NW platform 104

LIST OF TABLES

Table 3.1: Nanowire Growth Rate for each Diameter, Temperature, and Partial Pressure……..57

LIST OF ABBREVIATIONS

2DEG two–dimensional electron gas

3D three-dimensional

BHF buffered hydrofluoric acid

CVD chemical–vapor–deposition

EBL electron–beam lithography

EDS energy–dispersive x–ray spectroscopy

ENGRAVE Encoded Nanowire GRowth and Appearance through VLS and Etching

FF fill factor

FIB focused ion beam

$\mathbf{I_{SC}}$ short–circuit current

IPA isopropyl alcohol

IQE internal quantum efficiency

IR infrared

$\mathbf{J_{SC}}$ short–circuit current density

LED light-emitting diode

MIBK methyl isobutyl ketone

MMA methyl methacrylate

NPGS Nanometer Pattern Generation System NW nanowire

PML perfectly matched layer

PMMA polymethyl methacrylate

QD quantum dot

sccm standard cubic centimeters per minute

SEM scanning electron microscope

SERS surface–enhanced Raman spectroscopy

SLS solution-liquid-solid

SPP surface plasmon polariton

SRH Shockley–Read–Hall

SRV surface recombination velocity

STEM scanning transmission electron microscope

TEM transmission electron microscope

$\mathbf{T_{eu}}$ eutectic temperature

UV ultraviolet

$\mathbf{V_{OC}}$ open–circuit voltage

VLS vapor–liquid–solid

VS vapor–solid

VSS vapor–solid–solid

CHAPTER 1: INTRODUCTION

1.1 Semiconductor Nanowires

Precise patterning of semiconductor materials utilizing top-down lithographic techniques is integral to the advanced electronics we use on a daily basis. However, continued development of these lithographic technologies often results in the trade off of either high cost or low throughput.[1-2] Bottom-up, chemical methods to control the 3D nanoscale morphology of semiconductor nanostructures have received significant attention as a complementary technique. Semiconductor nanowires (NWs), nanoscale filaments of semiconductor material ~10-500 nm in diameter and ~1-50 microns in length, are an especially promising platform because the wire composition can be modulated during growth and the high aspect ratio, one-dimensional structure enables integration in a range of devices.[3-4] To date, many NW-based technologies have been demonstrated, including photovoltaic devices,[5-7] waveguides,[8-9] sensors,[10] and thermoelectrics.[11-12] These devices are often limited by the "wire" morphology and inability to create the diverse range of arbitrary structures and shapes routinely fabricated by top-down methods.

The primary focus of this thesis is to develop a deep understanding of NW synthetic processes, then utilize that understanding to enable new NW-based technologies. To this end, Chapter 2 introduces a new strategy to encode sub-10 nm morphology in Si NWs and presents two applications enabled by this morphological control. Chapters 3 and 4 examine more fundamental aspects of NW synthetic processes to further improve the resolution and quality of the technique introduced in Chapter 2. Finally, Chapter 5 discusses how the unique physical properties of NWs can be leveraged in next-generation solar energy devices.

1.2 Nanowire Synthesis

Semiconductor NWs may be synthesized by a variety of techniques, such as vapor-liquid-solid (VLS) growth, vapor-solid-solid (VSS) growth, or solution-liquid-solid (SLS) growth. These synthetic techniques typically utilize a metallic nanoparticle to facilitate growth along a particular crystallographic orientation of the semiconductor material, which produces wire-like structures with high aspect ratios. As such, metal-semiconductor binary phase diagrams, such as the Au-Si phase diagram depicted in Fig. 1.1, play an important role in choosing proper synthetic conditions. The Au-Si phase diagram was chosen because all NWs discussed in this thesis are Si with an Au catalyst. Also, the Au-Si system is a model system for semiconductor NW growth. The concepts learned from studying this system can be applied to other semiconductor-metal combinations to produce NWs of other semiconductor materials, such as Ge or GaAs.

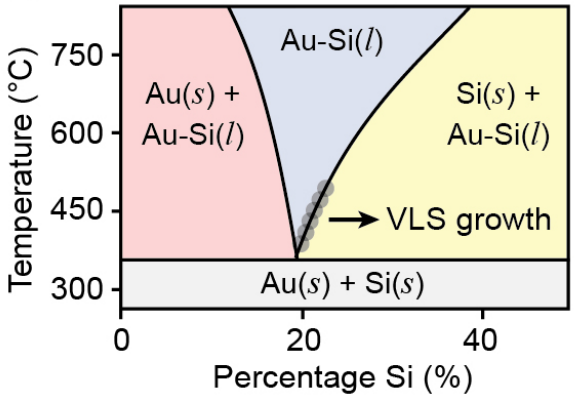

Figure 1.1 Au-Si Binary Phase Diagram

1.2.1 Vapor-Liquid-Solid Mechanism

The VLS mechanism is the most common and most refined technique for producing semiconductor NWs. It was originally reported by Wagner and Ellis of Bell Labs in 1964,[13] and

has become the most popular technique because it enables precise control of important nanowire properties, such as diameter[14] or composition.[15] Au-catalyzed VLS growth of Si NWs begins with a solid Au nanoparticle of a specified diameter. The Au nanoparticle is heated above the eutectic temperature (363 °C) in an inert atmosphere. To initiate VLS growth, a vapor phase Si precursor (e.g. SiH_4, Si_2H_6, or $SiCl_4$) is introduced. The Au nanoparticle catalyzes the decomposition of the Si precursor and a AuSi liquid alloy forms. With the continued supply of the Si precursor, the Si concentration in the liquid alloy catalyst particle increases, eventually supersaturating the alloy with Si (i.e. the system is forced to the right of the liquidus line in Fig. 1.1). At this point, solid Si crystallizes from the liquid catalyst and the NW begins to grow. The duration of Si precursor flow controls the NW length, while the Au catalyst size determines the NW diameter.

1.2.2 Vapor-Solid-Solid Mechanism

While the VLS mechanism is the most widely used synthetic technique to produce NWs, it comes with a few drawbacks. Most notably, it is unable to provide atomic scale control over the NW composition. To achieve this level of control, one cannot use a liquid catalyst because it acts as a reservoir of material when changing the NW composition (see section 1.5 for a more detailed discussion of this effect).[16] The VSS growth mechanism, which uses a solid catalyst instead of a liquid, circumvents the problems associated with a liquid catalyst and enables atomic scale control over NW composition.[17] However, VSS growth rates (~0.1-1 nm/min) are approximately two orders of magnitude slower than VLS growth rates, which precludes its widespread use despite the increased level of synthetic control.[18] The reduced growth rates are a result of the lower temperatures required to achieve a solid catalyst (typically below the eutectic temperature) and the decreased catalytic activity of a solid catalyst.[18] Chapter 4 discusses an alternative strategy for NW growth that enables one to reversibly switch between a liquid and solid catalyst under isothermal

conditions. The ability to repeatedly switch between VLS and VSS mechanisms allows one utilize the advantages of each while avoiding their respective drawbacks.

1.3 Understanding Nanowire Growth Mechanisms

To produce NWs of sufficient quality for technological applications, one must precisely control the NW physical properties, such as diameter, crystallinity, uniformity, and composition. The VLS and VSS mechanisms provide the necessary synthetic control to achieve this through controlling reaction parameters such as the catalyst size, temperature, pressure, precursor flow rates, or precursor chemistry. However, this is predicated on a thorough understanding of the nuances associated with these growth mechanisms. For instance, the crystallographic direction a NW grows along depends on the temperature,[19-21] pressure,[22-24] catalyst composition,[25-26] and NW sidewall chemistry[25, 27-29] (which is controlled through precursor chemistry). A change in growth direction, commonly referred to as kinking, is detrimental in device applications where straight NWs are needed; however, controlled kinking enables the design of more complex devices built around NWs, such as Si NW FETs that can probe individual cells.[30]

Much like kinking, non-catalytic deposition of semiconductor material on the NW sidewalls, often referred to as vapor-solid (VS) growth, is detrimental for some applications, but can also be leveraged to produce unique NW devices. For example, VS growth is catastrophic for the technique to control NW morphology introduced in Chapter 2, while Chapter 5 leverages controlled VS growth to produce high-efficiency NW-based photovoltaics. As the name suggests, VS growth occurs when the semiconductor precursor adds material directly to the NW sidewall, bypassing the liquid catalyst. The NW sidewall surface chemistry strongly affects the rate of VS growth.[31-33] Adsorbates such as H, Cl, or CH_3 can block VS growth.[29, 31-34] Unintended VS growth, which often occurs when the reaction temperature is too high, can lead to NWs with undesirable

properties, such as tapered sidewalls, unintentional doping, or low-resistance leakage pathways in electronic devices.

1.4 Characterizing and Modeling Nanowire Growth

To develop an understanding of NW synthetic processes one needs tools to characterize them and models to provide a framework for describing them. For NWs, techniques to quantify growth kinetics are central to understanding the underlying growth mechanisms. For example, studies centered around characterizing and interpreting NW growth kinetics have examined the rate-limiting step in the VLS mechanism,[35-43] probed the importance of surface chemistry on NW growth,[29, 32-33, 44-46] explored alternative catalyst materials,[18] studied the role of O in NW growth,[27] and provided detailed models of NW growth mechanisms.[16, 43, 47-52]

These studies have leveraged both *in situ* and *ex situ* techniques to measure NW growth rates. In general, *in situ* techniques have the advantage of ascertaining the instantaneous NW growth rate at all points along the wire. However, they require highly specialized equipment that interfaces an electron microscope with a CVD chamber. Consequently, all studies are done under UHV conditions, which do not accurately reflect synthetic conditions in standard hot-walled CVD reactors (~0.1-100 Torr). *Ex situ* techniques are far more common due to their practicality and are still useful for developing a deep understanding of NW growth mechanisms. For example, Chapters 3 and 4 of this thesis utilize *ex situ* characterization of NW growth kinetics to contribute new models for understanding the VLS and VSS growth mechanisms.

1.5 Controlling Nanowire Composition

As stated earlier, control of semiconductor composition at the nanometer scale is integral to many semiconductor technologies. When compared with other bottom-up device fabrication strategies, NWs provide unparalleled control over composition and morphology across multiple

length scales. This is largely due to the unique ability of the VLS mechanism to reliably produce structures with micron-scale dimensions but nanometer-scale control over composition across a wide variety of semiconductor materials. For example, Chapter 2 describes a technique for imparting sub-10 nm morphology to Si NWs by coupling precise control of the P concentration along the length of a NW with a selective etch.

Compositional NW heterostructures are formed by altering the supply of vapor-phase precursors during VLS growth. In Si NWs, this has been demonstrated with dopant atoms (*e.g.* NW p-n junctions[53]) and a wide variety of material combinations that share a similar crystal structure (*e.g.* Si/Ge[54] or Si/InP[55]). The ability to modulate the composition along a NW enables the creation of unique NW devices, but the abruptness of these material transitions is central to creating useful devices. When changing the composition of a NW, the liquid droplet can act as a reservoir of material even after a precursor gas is removed, causing the heterojunction to be broadened by a phenomenon termed the "reservoir effect".[17, 54, 56-62] Without taking special precautions to mitigate this phenomenon, the broadening is comparable to the NW diameter, which is too broad for many applications.

There are multiple strategies to mitigate the reservoir effect. For instance, the width of the material transition is related to the amount of material in the liquid catalyst, which makes reducing the solubility of the material in the catalyst an effective strategy. For liquid catalysts, this has been demonstrated with AuGa alloys.[63] Similarly, the VSS mechanism produces a solid catalyst, which has minimal (<<1%) solubility for the semiconductor.[17, 47] Abrupt compositional changes in Si NWs using the VSS mechanism have been demonstrated with dopants in Au-catalyzed NWs[64] and with Ge in AuAl- and AuAg-catalyzed NWs.[17-18] Alternatively, one can choose synthetic conditions that promote the removal of a particular species from the catalyst to

shorten the transition width, opposed to limiting its solubility. For example, properly tuned VLS growth conditions enable sub-5 nm dopant transitions in Au-catalyzed Si NWs by promoting associative desorption of P-containing species (e.g. PH_x) at the catalyst surface.[16, 46]

REFERENCES

1. Deotare, P. B.; McCutcheon, M. W.; Frank, I. W.; Khan, M.; Lončar, M., High quality factor photonic crystal nanobeam cavities. *Appl. Phys. Lett.* **2009,** *94* (12), 121106.

2. Novotny, L.; van Hulst, N., Antennas for light. *Nature Photonics* **2011,** *5* (2), 83-90.

3. Lieber, C. M., Nanoscale science and technology: building a big future from small things. *MRS Bull.* **2003,** *28* (07), 486-491.

4. Yang, P.; Yan, R.; Fardy, M., Semiconductor nanowire: what's next? *Nano Lett.* **2010,** *10* (5), 1529-36.

5. Hochbaum, A. I.; Yang, P., Semiconductor nanowires for energy conversion. *Chem. Rev.* **2010,** *110* (1), 527-46.

6. Kempa, T. J.; Day, R. W.; Kim, S.-K.; Park, H.-G.; Lieber, C. M., Semiconductor nanowires: a platform for exploring limits and concepts for nano-enabled solar cells. *Energy Environ. Sci.* **2013,** *6* (3), 719-733.

7. Zhang, X.; Pinion, C. W.; Christesen, J. D.; Flynn, C. J.; Celano, T. A.; Cahoon, J. F., Horizontal Silicon Nanowires with Radial p–n Junctions: A Platform for Unconventional Solar Cells. *J. Phys. Chem. Lett.* **2013,** *4* (12), 2002-2009.

8. Qian, F.; Li, Y.; Gradečak, S.; Wang, D.; Barrelet, C. J.; Lieber, C. M., Gallium Nitride-Based Nanowire Radial Heterostructures for Nanophotonics. *Nano Lett.* **2004,** *4* (10), 1975-1979.

9. Law, M.; Sirbuly, D. J.; Johnson, J. C.; Goldberger, J.; Saykally, R. J.; Yang, P. D., Nanoribbon waveguides for subwavelength photonics integration. *Science* **2004,** *305* (5688), 1269-1273.

10. Cui, Y.; Wei, Q. Q.; Park, H. K.; Lieber, C. M., Nanowire nanosensors for highly sensitive and selective detection of biological and chemical species. *Science* **2001,** *293* (5533), 1289-1292.

11. Boukai, A. I.; Bunimovich, Y.; Tahir-Kheli, J.; Yu, J. K.; Goddard, W. A., 3rd; Heath, J. R., Silicon nanowires as efficient thermoelectric materials. *Nature* **2008,** *451* (7175), 168-71.

12. Hochbaum, A. I.; Chen, R.; Delgado, R. D.; Liang, W.; Garnett, E. C.; Najarian, M.; Majumdar, A.; Yang, P., Enhanced thermoelectric performance of rough silicon nanowires. *Nature* **2008,** *451* (7175), 163-7.

13. Wagner, R. S.; Ellis, W. C., Vapor-Liquid-Solid Mechanism of Single Crystal Growth. *Applied Physics Letters* **1964,** *4* (5), 89.

14. Cui, Y.; Lauhon, L. J.; Gudiksen, M. S.; Wang, J. F.; Lieber, C. M., Diameter-controlled synthesis of single-crystal silicon nanowires. *Applied Physics Letters* **2001,** *78* (15), 2214-2216.

15. Lauhon, L. J.; Gudiksen, M. S.; Lieber, C. M., Semiconductor nanowire heterostructures. *Philos T Roy Soc A* **2004,** *362* (1819), 1247-1260.

16. Christesen, J. D.; Pinion, C. W.; Zhang, X.; McBride, J. R.; Cahoon, J. F., Encoding Abrupt and Uniform Dopant Profiles in Vapor-Liquid-Solid Nanowires by Suppressing the Reservoir Effect of the Liquid Catalyst. *Acs Nano* **2014,** *8* (11), 11790-11798.

17. Wen, C. Y.; Reuter, M. C.; Bruley, J.; Tersoff, J.; Kodambaka, S.; Stach, E. A.; Ross, F. M., Formation of Compositionally Abrupt Axial Heterojunctions in Silicon-Germanium Nanowires. *Science* **2009,** *326* (5957), 1247-1250.

18. Chou, Y. C.; Wen, C. Y.; Reuter, M. C.; Su, D.; Stach, E. A.; Ross, F. M., Controlling the growth of Si/Ge nanowires and heterojunctions using silver-gold alloy catalysts. *ACS Nano* **2012,** *6* (7), 6407-15.

19. Wagner, R. S.; Doherty, C. J., Mechanism of Branching and Kinking during Vls Crystal Growth. *J Electrochem Soc* **1968,** *115* (1), 93-&.

20. Madras, P.; Dailey, E.; Drucker, J., Kinetically Induced Kinking of Vapor-Liquid-Solid Grown Epitaxial Si Nanowires. *Nano Lett* **2009,** *9* (11), 3826-3830.

21. Lee, G.; Woo, Y. S.; Yang, J. E.; Lee, D.; Kim, C. J.; Jo, M. H., Directionally Integrated VLS Nanowire Growth in a Local Temperature Gradient. *Angew Chem Int Edit* **2009,** *48* (40), 7366-7370.

22. Dailey, E.; Madras, P.; Drucker, J., Composition and growth direction control of epitaxial vapor-liquid-solid-grown SiGe nanowires. *Applied Physics Letters* **2010,** *97* (14).

23. Lugstein, A.; Steinmair, M.; Hyun, Y. J.; Hauer, G.; Pongratz, P.; Bertagnolli, E., Pressure-induced orientation control of the growth of epitaxial silicon nanowires. *Nano Lett* **2008,** *8* (8), 2310-2314.

24. Tian, B. Z.; Xie, P.; Kempa, T. J.; Bell, D. C.; Lieber, C. M., Single-crystalline kinked semiconductor nanowire superstructures. *Nat Nanotechnol* **2009,** *4* (12), 824-829.

25. Kawashima, T.; Mizutani, T.; Nakagawa, T.; Torii, H.; Saitoh, T.; Komori, K.; Fujii, M., Control of surface migration of gold particles on Si nanowires. *Nano Lett* **2008,** *8* (1), 362-368.

26. Wang, J.; Plissard, S. R.; Verheijen, M. A.; Feiner, L. F.; Cavalli, A.; Bakkers, E. P. A. M., Reversible Switching of InP Nanowire Growth Direction by Catalyst Engineering. *Nano Lett* **2013,** *13* (8), 3802-3806.

27. Kodambaka, S.; Hannon, J. B.; Tromp, R. M.; Ross, F. M., Control of Si nanowire growth by oxygen. *Nano Lett* **2006,** *6* (6), 1292-1296.

28. Musin, I. R.; Filler, M. A., Chemical Control of Semiconductor Nanowire Kinking and Superstructure. *Nano Lett* **2012,** *12* (7), 3363-3368.

29. Shin, N.; Filler, M. A., Controlling Silicon Nanowire Growth Direction via Surface Chemistry. *Nano Lett* **2012,** *12* (6), 2865-2870.

30. Xu, L.; Jiang, Z.; Qing, Q.; Mai, L. Q.; Zhang, Q. J.; Lieber, C. M., Design and Synthesis of Diverse Functional Kinked Nanowire Structures for Nanoelectronic Bioprobes. *Nano Lett* **2013,** *13* (2), 746-751.

31. Gentile, P.; Solanki, A.; Pauc, N.; Oehler, F.; Salem, B.; Rosaz, G.; Baron, T.; Den Hertog, M.; Calvo, V., Effect of HCl on the doping and shape control of silicon nanowires. *Nanotechnology* **2012,** *23* (21).

32. Musin, I. R.; Boyuk, D. S.; Filler, M. A., Surface chemistry controlled diameter-modulated semiconductor nanowire superstructures. *J Vac Sci Technol B* **2013,** *31* (2).

33. Musin, I. R.; Shin, N.; Filler, M. A., Diameter modulation as a route to probe the vapour-liquid-solid growth kinetics of semiconductor nanowires. *Journal of Materials Chemistry C* **2014,** *2* (17), 3285-3291.

34. Sivaram, S. V.; Shin, N.; Chou, L. W.; Filler, M. A., Direct Observation of Transient Surface Species during Ge Nanowire Growth and Their Influence on Growth Stability. *Journal of the American Chemical Society* **2015,** *137* (31), 9861-9869.

35. Bootsma, G. A.; Gassen, H. J., A Quantitative Study on the Growth of Silicon Whiskers from Silane and Germanium Whiskers from Germane. *J. Cryst. Growth* **1971,** *10* (3), 223-234.

36. Givargizov, E. I., Fundamental Aspects of Vls Growth. *Journal of Crystal Growth* **1975,** *31* (Dec), 20-30.

37. Weyher, J., Some Notes on the Growth Kinetics and Morphology of VLS Silicon Crystals Grown with Platinum and Gold as Liquid-Forming Agents. *J. Cryst. Growth* **1978,** *43* (2), 235-244.

38. Kikkawa, J.; Ohno, Y.; Takeda, S., Growth rate of silicon nanowires. *Applied Physics Letters* **2005,** *86* (12), 123109.

39. Kodambaka, S.; Tersoff, J.; Reuter, M. C.; Ross, F. M., Diameter-Independent Kinetics in the Vapor-Liquid-Solid Growth of Si Nanowires. *Phys. Rev. Lett.* **2006,** *96* (9), 096105.

40. Lew, K.-K.; Redwing, J. M., Growth characteristics of silicon nanowires synthesized by vapor–liquid–solid growth in nanoporous alumina templates. *Journal of Crystal Growth* **2003,** *254* (1-2), 14-22.

41. Schmidt, V.; Senz, S.; Gösele, U., Diameter Dependence of the Growth Velocity of Silicon Nanowires Synthesized via the Vapor-Liquid-Solid Mechanism. *Phys. Rev. B* **2007,** *75* (4), 045335.

42. Dubrovskii, V.; Sibirev, N.; Cirlin, G.; Soshnikov, I.; Chen, W. H.; Larde, R.; Cadel, E.; Pareige, P.; Xu, T.; Grandidier, B.; Nys, J. P.; Stievenard, D.; Moewe, M.; Chuang, L.; Chang-Hasnain, C., Gibbs-Thomson and Diffusion-Induced Contributions to the Growth rate of Si, InP, and GaAs Nanowires. *Phys. Rev. B* **2009,** *79* (20), 205316.

43. Dubrovskii, V. G.; Sibirev, N. V.; Cirlin, G. E., Kinetic model of the growth of nanodimensional whiskers by the vapor-liquid-crystal mechanism. *Technical Physics Letters* **2004,** *30* (8), 682-686.

44. Musin, I. R.; Shin, N.; Filler, M. A., Diameter modulation as a route to probe the vapour–liquid–solid growth kinetics of semiconductor nanowires. *Journal of Materials Chemistry C* **2014**.

45. Shin, N.; Filler, M. A., Controlling silicon nanowire growth direction via surface chemistry. *Nano Lett* **2012,** *12* (6), 2865-70.

46. Kim, S.; Hill, D. J.; Pinion, C. W.; Christesen, J. D.; McBride, J. R.; Cahoon, J. F., Designing Morphology in Epitaxial Silicon Nanowires: The Role of Gold, Surface Chemistry, and Phosphorus Doping. *Acs Nano* **2017**.

47. Wen, C. Y.; Tersoff, J.; Reuter, M. C.; Stach, E. A.; Ross, F. M., Step-Flow Kinetics in Nanowire Growth. *Phys Rev Lett* **2010,** *105* (19).

48. Pinion, C. W.; Hill, D. J.; Christesen, J. D.; McBride, J. R.; Cahoon, J. F., Barrierless Switching between a Liquid and Superheated Solid Catalyst during Nanowire Growth. *J Phys Chem Lett* **2016,** *7* (20), 4236-4242.

49. Pinion, C. W.; Nenon, D. P.; Christesen, J. D.; Cahoon, J. F., Identifying crystallization- and incorporation-limited regimes during vapor-liquid-solid growth of Si nanowires. *ACS Nano* **2014,** *8* (6), 6081-8.

50. Givargizov, E. I.; Chernov, A. A., Growth-Rate of Whiskers Grown by Vapor-Liquid-Solid Mechanism, and Role of Surface-Energy. *Kristallografiya* **1973,** *18* (1), 147-153.

51. Dubrovskii, V. G.; Sibirev, N. V.; Cirlin, G. E.; Harmand, J. C.; Ustinov, V. M., Theoretical analysis of the vapor-liquid-solid mechanism of nanowire growth during molecular beam epitaxy. *Physical Review E* **2006,** *73* (2).

52. Dubrovskii, V. G.; Sibirev, N. V.; Suris, R. A.; Cirlin, G. E.; Ustinov, V. M.; Tchernysheva, M.; Harmand, J. C., The role of surface diffusion of adatoms in the formation of nanowire crystals. *Semiconductors* **2006,** *40* (9), 1075-1082.

53. Kempa, T. J.; Tian, B. Z.; Kim, D. R.; Hu, J. S.; Zheng, X. L.; Lieber, C. M., Single and Tandem Axial p-i-n Nanowire Photovoltaic Devices. *Nano Lett* **2008,** *8* (10), 3456-3460.

54. Wu, Y.; Fan, R.; Yang, P., Block-by-Block Growth of Single-Crystalline Si/SiGe Superlattice Nanowires. *Nano Lett* **2002,** *2* (2), 83-86.

55. Hocevar, M.; Immink, G.; Verheijen, M.; Akopian, N.; Zwiller, V.; Kouwenhoven, L.; Bakkers, E., Growth and optical properties of axial hybrid III-V/silicon nanowires. *Nat. Commun.* **2012,** *3*.

56. Ross, F. M., Controlling nanowire structures through real time growth studies. *Rep. Prog. Phys.* **2010,** *73* (11).

57. Dick, K. A.; Bolinsson, J.; Borg, B. M.; Johansson, J., Controlling the Abruptness of Axial Heterojunctions in III-V Nanowires: Beyond the Reservoir Effect. *Nano Lett* **2012,** *12* (6), 3200-3206.

58. Amit, I.; Givan, U.; Connell, J. G.; Paul, D. F.; Hammond, J. S.; Lauhon, L. J.; Rosenwaks, Y., Spatially Resolved Correlation of Active and Total Doping Concentrations in VLS Grown Nanowires. *Nano Lett* **2013**.

59. Hilse, M.; Ramsteiner, M.; Breuer, S.; Geelhaar, L.; Riechert, H., Incorporation of the dopants Si and Be into GaAs nanowires. *Applied Physics Letters* **2010,** *96* (19).

60. Clark, T. E.; Nimmatoori, P.; Lew, K. K.; Pan, L.; Redwing, J. M.; Dickey, E. C., Diameter dependent growth rate and interfacial abruptness in vapor-liquid-solid Si/Si(1-x)Ge(x) heterostructure nanowires. *Nano Lett* **2008,** *8* (4), 1246-1252.

61. Amato, M.; Palummo, M.; Rurali, R.; Ossicini, S., Silicon-Germanium Nanowires: Chemistry and Physics in Play, from Basic Principles to Advanced Applications. *Chem. Rev.* **2014,** *114* (2), 1371-1412.

62. Ohlsson, B. J.; Bjork, M. T.; Persson, A. I.; Thelander, C.; Wallenberg, L. R.; Magnusson, M. H.; Deppert, K.; Samuelson, L., Growth and characterization of GaAs and InAs nano-whiskers and InAs/GaAs heterostructures. *Physica E-Low-Dimensional Systems & Nanostructures* **2002,** *13* (2-4), 1126-1130.

63. Perea, D. E.; Li, N.; Dickerson, R. M.; Misra, A.; Picraux, S. T., Controlling Heterojunction Abruptness in VLS-Grown Semiconductor Nanowires via in situ Catalyst Alloying. *Nano Lett* **2011,** *11* (8), 3117-3122.

64. Cohen-Karni, T.; Casanova, D.; Cahoon, J. F.; Qing, Q.; Bell, D. C.; Lieber, C. M., Synthetically Encoded Ultrashort-Channel Nanowire Transistors for Fast, Pointlike Cellular Signal Detection. *Nano Lett* **2012,** *12* (5), 2639-2644.

CHAPTER 2: SYNTHETICALLY ENCODING 10-nm MORPHOLOGY IN SILICON NANOWIRES [1]

2.1 Introduction

Most semiconductor technologies rely on the ability to pattern materials with nanometer-scale features using top-down lithographic tools. Over the last decade, however, bottom-up chemical methods to control the size, shape, and composition of nanoscale materials have progressed rapidly, resulting in a diverse set of well-controlled morphologies including dots, rods, ribbons, and wires.[1-3] Semiconductor NWs are recognized as an especially important technological building block because the high aspect ratio can be used for longitudinal transport of electrical or optical signals.[1,2] A variety of devices have been demonstrated, including sensors,[4] waveguides,[5] phase-change memory,[6] light-emitting diodes,[7] and solar cells.[8-11] Nevertheless, current NW-based technology has been limited by the material's translational symmetry and the inability to pattern arbitrary, nanometer-scale morphological features.

NWs are typically synthesized using the VLS mechanism,[12] in which a metal nanoparticle catalyzes one-dimensional growth of a single-crystalline semiconductor material. Advancements in VLS-based technologies have generally involved synthesis of new materials or heterostructures.[13] For instance, NW superlattices, in which the composition of a NW is modulated along the growth axis, have been reported for Si/SiGe,[14] GaAs/GaP,[15] InAs/InP,[16,17] Zn-doped

[1] This chapter previously appeared as an article in Nano Letters. The original citation is as follows: Christesen, J. D.; Pinion, C. W.; Grumstrup, E. M.; Papanikolas, J. M.; Cahoon, J. F. Synthetically Encoding 10 nm Morphology in Silicon Nanowires. Nano Lett. 2013, 13, 6281–6286.

InP,[18] CdSe/ZnSe,[19] and P-doped Si.[20] Modulation of NW composition often results in faceting of the NW surface, providing some capability to control morphology during synthesis.[17,18,21] In addition, NW superstructures have been reported in the form of controllably kinked NWs that break the one-dimensional shape.[22,23] Nevertheless, only a handful of reports describe efforts to alter the NW geometry and encode specific morphology. For example, controlled vapor-solid over-coating on the NW surface has been used to create tapered structures[24] and periodic variations in morphology.[25] In addition, modulation of the size of the metal catalyst during growth has been shown to provide control over the NW diameter.[26,27] For metal NWs, electrodeposition in metal oxide templates followed by wet-chemical etching has been used to create wires with alternating, nanoscale structures.[28,29] However, a method for accurate, nanometer-scale control of morphology in single-crystalline semiconductor NWs has not been developed. Here, we demonstrate a new method to achieve this type of high-fidelity shape control, a process which we term "ENGRAVE" for "Encoded Nanowire GRowth and Appearance through VLS and Etching." The key aspects and capabilities of this method are illustrated in Fig. 2.1 and elaborated below.

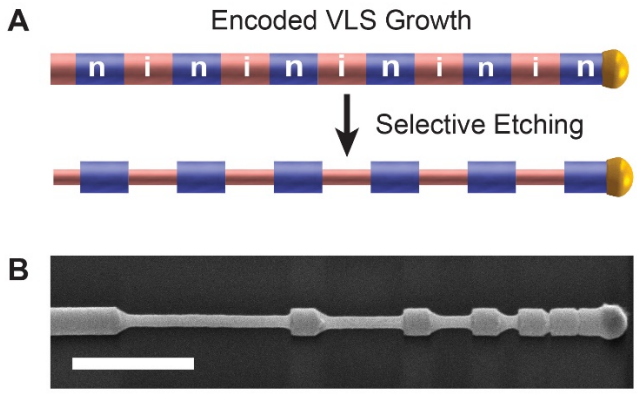

Figure 2.1: Synthesis of Si NWs with encoded morphology

(A) Schematic illustration of NW growth including rapid modulation of P dopant incorporation to form heavily-doped n-type (n) and undoped intrinsic (i) segments that are selectively etched using wet-chemical methods to form a grating. (B) SEM image of a NW grating encoded (from left to right) with sequential intrinsic segments for 200, 100, 50, 25, 10, and 5 s; scale bar, 500 nm.

2.2 Nanowire Synthesis and Etching

Si NWs were grown by a VLS mechanism in a home-built, hot-wall chemical vapor deposition (CVD) system at 420 °C using Au nanoparticles as catalysts, silane (SiH_4) as the source of Si, and hydrogen (H_2) as the carrier gas (see section 2.6.1 for details). As illustrated schematically in Fig. 2.1A, an additional flow of phosphine (PH_3) was rapidly modulated during growth[20] to encode varying levels of P, an n-type substitutional dopant with high solubility in Si.[30-32] The etch rate of doped Si with aqueous KOH solution is well-known to decrease with higher dopant concentration.[33] This effect has been observed in doped Si NWs, producing changes in diameter along the axis.[34,35] Here, we develop this effect as a tool to encode arbitrary, high-resolution morphology along the NW growth axis, enabling new technological applications of Si NWs.

2.3 Optimization of ENGRAVE Technique

To delineate the spatial resolution of the ENGRAVE process, we synthesized NWs with six intrinsic segments encoded along the axis for increasingly short time scales. As shown in Fig. 2.1B, wet-chemical etching of these segments yielded an abrupt and conformal reduction in the NW diameter. The largest segment, encoded for 200 s, produced a feature ~700 nm in length while the smallest segment, encoded for 5 s, produced a feature ~10 nm in length, defining the lower limit of the spatial resolution for this process. This example also demonstrates that NW growth time is directly proportional to spatial length scale. Quantitative analysis of the NW growth rate yielded a value of 213 ± 6 nm/min, which was used throughout this work to convert growth times to length scales. This rate is comparatively slow because of the low CVD temperature, 420 °C, chosen to minimize radial over-coating and doping of the NW surface, a known problem during Si NW synthesis.[36,37] By minimizing the over-coating, we could encode high-fidelity nanoscale features over macroscopic length scales, as exemplified in Fig. 2.2A by the 400 nm-pitch grating encoded over 50 μm of a single NW.

For the synthesis of NWs with complex morphology we measured the etch rate of Si NWs encoded with P doping levels ranging from 5.0×10^{20} to less than 1.0×10^{19} dopants/cm^3, as depicted in Fig. 2.2B. Note that these doping levels were calculated from the gas-phase ratio of Si to P during CVD growth and the actual values could be lower as a result of incomplete P incorporation.[32] Quantitative evaluation of the etch rate reveals a non-linear dependence on doping level that is well approximated with a single exponential function and varies from 2.1 nm/s for 'intrinsic' segments with doping levels $<1.0 \times 10^{19}$ cm^{-3} to negligible etching (<0.1 nm/s) with heavily doped segments. The exponential dependence is most likely a result of the logarithmic

dependence of the Fermi level position on the doping level, which modulates the rate of Si oxidation and dissolution at the semiconductor-solution interface.[33]

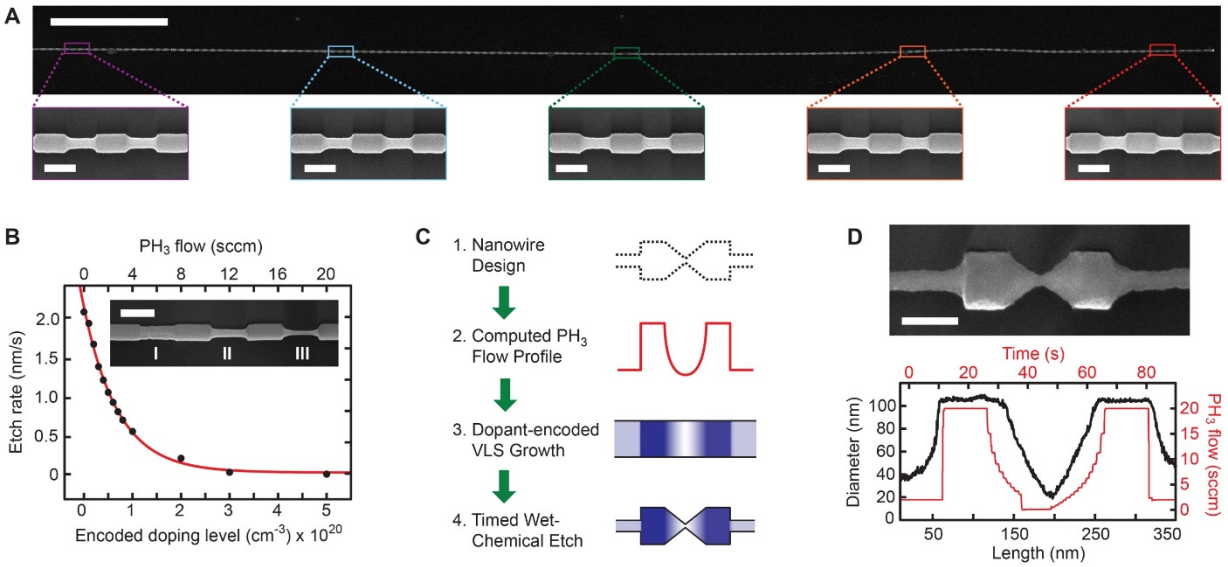

Figure 2.2: Characterization of NW growth, etching, and morphology

(A) Upper: SEM image of a grating-encoded NW more than 50 μm in axial length; scale bar, 5 μm. Lower: Higher magnification SEM images of select sections of the NW in the upper panel; scale bars, 200 nm. (B) Radial etch rate of Si NWs as function of encoded P doping levels. Red curve represents the best fit to a single exponential function. Inset: SEM image of a NW with segments I, II, and III encoded with P doping levels of $1x10^{20}$ cm^{-3}, $5x10^{19}$ cm^{-3}, and intrinsic, respectively, and etched for 25 s; scale bar, 200 nm. (C) Schematic of the sequential process for bottom-up synthesis of complex NW morphologies. (D) Upper: SEM image of a NW encoded with a bow-tie; scale bar, 100 nm. Lower: NW diameter (black curve and left-hand axis) as a function of length for the bow-tie shown in upper panel, and measured phosphine flow rate (red curve and right-hand axis) in standard cubic centimeters per minute (sccm) as a function of time during CVD growth.

The precise calibration of the NW growth and etch rates enables rational design and synthesis of arbitrary high-resolution morphologies, as outlined schematically in Fig. 2.2C. This process involves 1) design of the morphological profile, 2) conversion of the physical profile into a dopant profile, 3) VLS growth of the dopant-encoded NW, and 4) wet-chemical etching. As an example, we used this procedure to form the bow-tie structure depicted in Fig. 2.2D. The phosphine flow profile for the bow-tie (red curve Fig. 2.2D) is complex, requiring over 25 changes in flow rate over a time scale of one minute. The diameter profile (black curve Fig. 2.2D) shows the resulting structure to be smoothly tapered with a monotonically decreasing then increasing diameter that reduces to a diameter of ~15 nm at the narrowest point. Note that the phosphine flow profile was modified to be asymmetric around the flow minimum to account for dopants retained by the Au catalyst, a phenomenon termed the reservoir effect.[38]

We used other complex doping profiles to encode the range of morphological features shown in SEM images in Fig. 2.3. These structures include periodic (images 1-4) or non-periodic (image 5) gratings, nanogaps with gap sizes as small as 10 nm (images 6-7), suspended nanorods (image 8), and sinusoidal profiles (images 9-10). These morphologies could each enable a different class of NW-based technology. For instance, the suspended nanorods could be used as mechanical oscillators for nanoelectromechanical systems,[39] periodic gratings for optical applications in nanophotonics.[40] and non-periodic gratings as a method to control thermal transport along the wires, enabling the use of Si as a thermoelectric material.[41,42] Although full development of these applications is outside the scope of this work, below, we highlight two distinct applications of ENGRAVE NWs in the areas of plasmonics (Fig. 2.4) and electronics (Fig. 2.5).

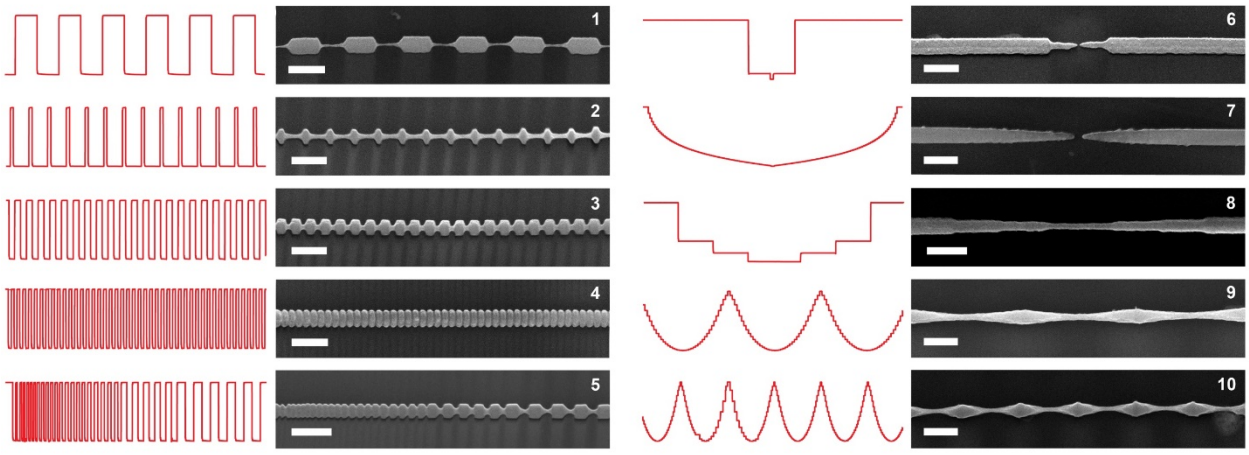

Figure 2.3: SEM images and phosphine flow profiles for the synthesis of Si NWs with complex morphology

The measured phosphine flow profile used to encode the morphology of each segment is depicted in red to the left of each SEM image; all scale bars, 200 nm. The flow rates vary from 0 to 20 sccm for each NW.

2.4 Applications of ENGRAVE

Field-enhanced spectroscopies, such as surface-enhanced Raman spectroscopy (SERS), are often performed using Noble metal nanostructures that support surface plasmon polaritons (SPPs).[43] Through careful design of the shape of a nanostructure, SPP resonances can be used to confine and amplify incident electromagnetic fields at specific wavelengths and spatial positions.[44] Following the procedure depicted in Fig. 2.4A, we used nanogap-encoded NWs as the topological templates for Noble metal films, creating Si/Au nanostructures with tunable SPP resonances. As shown by the SEM images in Fig. 2.4B, deposition of ~50 nm of Au on the NWs by physical vapor deposition preserved the high-resolution structures and nanogap morphology. We used finite-element optical simulations (see Fig. 2.4C) to design Si/Au ENGRAVE structures with specific SPP characteristics. The NWs behave as plasmonic resonator antennas,[45] in which the length of

the segments adjacent to the gap control the field enhancement as a result of constructive or destructive interference of the SPP wave along the NW axis.[46,47] For a wavelength of 633 nm, we found that segments ~775 nm in length were on-resonance, producing intense fields in the gap, while segments ~1175 nm in length were off-resonance, exhibiting weaker field enhancement. As proof-of-concept, we performed SERS imaging on the Si/Au NWs coated with methylene blue.[46,47] We observed a greater than ten-fold Raman signal enhancement from the on-resonance structure, as shown by the spectra in Fig. 2.4D. In addition, Raman imaging (see Fig. 2.4E) confirmed that the signal enhancement is localized to a narrow spatial region around the gap. In comparison, the off-resonance NW shows a weak Raman signal arising from both the gap and the two ends of the rods, a result that is in good agreement with the optical simulations in Fig. 2.4C. These results highlight the capability for ENGRAVE to serve as a simple route to create nanoplasmonic structures with tunable resonances for field-enhanced spectroscopy[43] and nanophotonic technologies.[44]

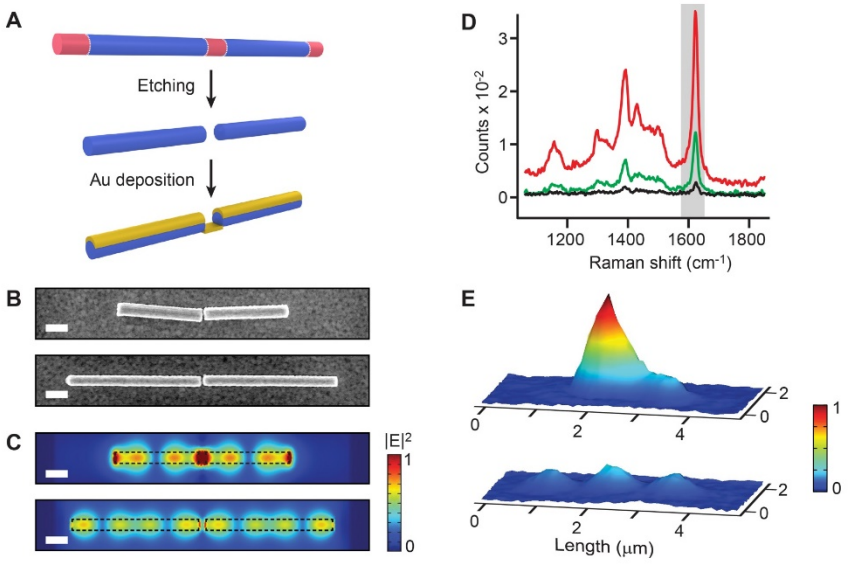

Figure 2.4: Nanogap-encoded NWs for plasmonics

(A) Schematic illustration of Au deposition on a nanogap-encoded NW. (B) SEM images of nanogap-encoded Si NWs with 50 nm Au, gaps of ~30 nm, and segment lengths of ~775 nm (upper image) and ~1175 nm (lower image); scale bars, 200 nm. (C) Finite-element optical simulations of the Si/Au nanogap structures depicted in panel B showing the scattered field ($|E|^2$) in the plane above the NW resulting from illumination at normal incidence with a transverse-magnetic plane wave at 633 nm. The optically excited SPP mode is on-resonance and off-resonance in the upper and lower images, respectively; scale bars, 200 nm. (D) Raman spectra of methylene blue collected from the planar Au film (black), the off-resonance NW (green), and on-resonance NW (red). The shaded region denotes the spectral range used to generate spatial maps of the Raman intensity. (E) Three-dimensional spatial maps of the relative Raman signal intensity generated by raster scanning a 633 nm laser over on- and off-resonance nanogap-encoded Si/Au structures with segment lengths of ~775 nm (upper) and ~1175 nm (lower), respectively.

As a second application of ENGRAVE, we fabricated core/shell Si/SiO_2 nanorod-encoded devices for use as resistive switches in non-volatile memory.[6,48,49] The fabrication steps are illustrated in Fig. 2.5A. First, an n-type/intrinsic/n-type NW was synthesized with a 50 nm intrinsic channel. Second, the channel was etched to a diameter of ~30 nm to produce a suspended nanorod, and third the wire was thermally oxidized to create a ~10 nm diameter Si core encased by an oxide shell. Fourth, electrical contacts were fabricated to the two n-type segments adjacent to the intrinsic channel, as shown by the SEM image in Fig. 2.5B. Device simulations[50] (see Fig. 2.5C) indicate that this geometry concentrates the voltage drop and electric field within the narrow channel region, enabling a resistive switching effect as observed in a planar Si/SiO_2 system.[48,49] Initial current-voltage (*I-V*) measurements showed an Ohmic response from the device with a resistance of 54.7 kΩ, indicating the presence of a thin Si filament encapsulated by the SiO_2 shell. After an electroforming process consisting of multiple *I-V* sweeps at high bias (see section 2.6.2), the device converged to the characteristic 'switching' *I-V* behavior (see Fig. 2.5D) expected from a Si/SiO_2 system.[48,49] The *I-V* curve exhibits a low voltage region that 'sets' the device to a low resistance state and a high voltage region that 'resets' the device to a high resistance state.

To use the nanorod-encoded device as non-volatile memory, we applied sequential 'set' and 'reset' voltage pulses (100 μs) of 8 V and 12 V, respectively, to reversibly change the resistance of the device. As shown in Fig. 2.5E, we cycled the NW device through ten memory states and achieved on/off current ratios of nearly 10^2. With further development, we expect that at least 100 memory bits could be encoded on a single NW and lower voltage operation achieved with smaller nanorod segments. These initial results demonstrate the facile integration of ENGRAVE structures in electronic devices and furthermore highlight the emergent electronic characteristics that can be encoded through morphology.

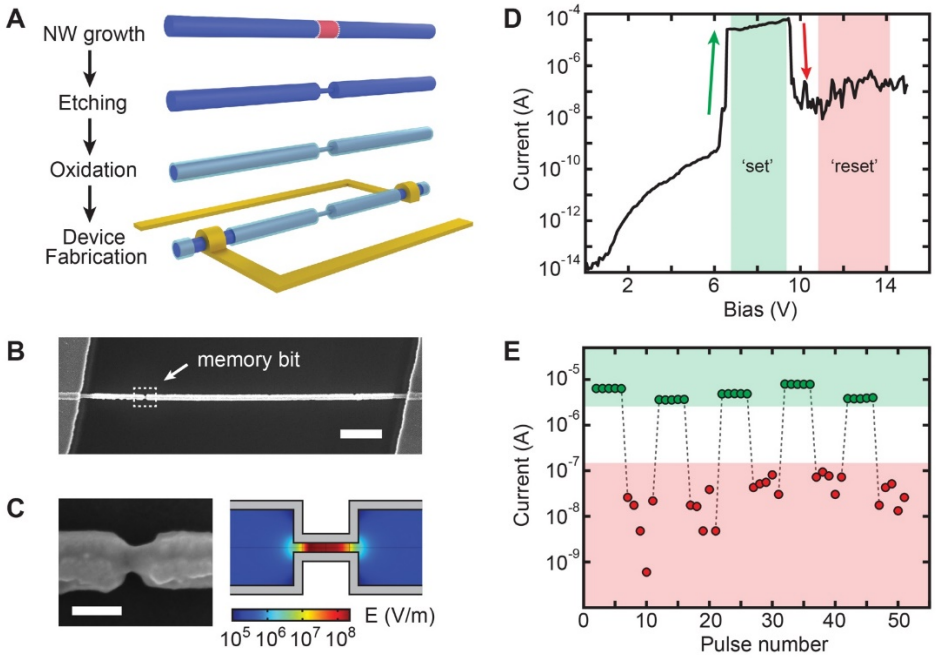

Figure 2.5: Nanorod-encoded NWs for non-volatile memory

(A) Schematic illustration of the sequential process used to fabricate a non-volatile memory bit. (B) SEM image of a NW device encoded with a non-volatile memory bit (dashed box) showing Ti/Pd Ohmic contacts on the far left and right; scale bar, 1 μm. (C) Left: SEM image of the encoded memory bit corresponding to the dashed white box in panel B; scale bar, 100 nm. Right: finite-element simulation of the electric field magnitude across the NW at an applied bias of +8 V plotted in a logarithmic color scale for a nanorod segment 50 nm in length and 10 nm in diameter. (D) Characteristic switching *I-V* curve for an ENGRAVE NW memory device. The shaded green and red regions define the 'set' and 'reset' bias ranges, respectively. (E) Resistive switching behavior over ten memory cycles. Dashed lines represent the 'set'/'reset' pulses between current readings, which were acquired five times at 1 V between each 'set' or 'reset' pulse.

2.5 Conclusion

In summary, we have demonstrated a method, termed ENGRAVE, to encode high-resolution morphology along the growth axis of Si NWs. We anticipate this process will be extended to other NW materials, such as GaAs/GaP[51] *et al*., that can be selectively etched with gas-phase or wet-chemical techniques and will represent a general route to encode new functionality in semiconductor NWs.

2.6 Detailed Methods

2.6.1 Nanowire Growth

Si NWs were grown with a home-built, hot-wall CVD system using SiH_4 (Voltaix), PH_3 (Voltaix; diluted to 1000 ppm in H_2), and H_2 (Matheson TriGas 5N semiconductor grade) gases. The CVD system consists of a quartz tube furnace (Lindberg Blue M) with 1 inch diameter bore, fast-responding mass-flow controllers (MKS Instruments P4B), a pressure control system (MKS Instruments 250E), and vacuum system with base pressure of $1x10^{-4}$ Torr. The CVD system was computer-controlled using custom Labview software to enable rapid and reproducible modulation of the NW growth conditions and gas flow rates. Calibration runs indicated that changes in flow rate were achieved on time scales <1 s and that complete exchange of gas within the quartz tube was achieved on a time scale of ~5 s. Thus the resolution of ENGRAVE structures was primarily limited by the kinetics of the NW growth or etching process and not by the mechanics of the CVD system. For a typical NW growth run, citrate-stabilized ~100 nm Au catalysts (BBI International) were dispersed on 2 cm x 1 cm Si wafers (University Wafer; p-type Si with 600 nm thermal oxide) that had been functionalized with poly-L-lysine solution (Aldrich). These growth substrates were inserted into the center of the tube furnace, and the furnace temperature was ramped to 450 °C to nucleate NW growth for between 5 to 60 min using 2.00 sccm SiH_4 and 200.0 sccm H_2 at 40.0 Torr total reactor pressure. The reactor temperature was then cooled (1 °C/min) to 420 °C and

ENGRAVE structures were encoded by introducing PH_3 gas with a tightly controlled flow profile, as discussed in the text.

2.6.2 Etching and Device Fabrication

To fabricate ENGRAVE structures, NWs were transferred from the growth substrates onto Si wafers coated with 100 nm thermal oxide and 200 nm Si nitride (Nova Electronic Materials). NWs, which were then lying flat on the substrate, were etched by immersing in concentrated buffered hydrofluoric acid (Transense BHF Improved) for 10 s, rinsing in water and isopropanol, etching in KOH solution (20.0 g KOH; 80.0 g water; 20 mL isopropanol as top surface layer) at 40 °C for variable times up to 90 s, and rinsing in water and isopropanol. To fabricate Si NWs with Noble metal structures, Si NWs were etched as described above and then placed in an electron-beam evaporator (Thermionics VE-100) for deposition of 50 nm Au at normal incidence with a rate of ~1 Å/s at a pressure $<1x10^{-7}$ Torr. Thermal oxidation of NWs was performed for 3 min in a quartz tube furnace with 100 Torr O_2 at 1000 °C. NW devices were fabricated by defining metal contacts to individual NWs using electron-beam lithography followed by electron-beam evaporation of 3 nm Ti and 150 nm Pd. Devices were measured under nitrogen environment using a home-built probe station equipped with W probe tips (Signatone) connected to a Keithley 2636A sourcemeter. Single voltage pulses were applied using a square wave pattern with nominal width of 100 μs, the minimum pulse width produced by our measurement system. Prior to operation as a resistive switch for non-volatile memory, an electroforming process consisting of multiple voltage sweeps to high bias was performed. A typical forming process contained two sweeps from 0-30 V, two sweeps from 0-25 V and two sweeps from 0-20 V. Following the final 0-20 V sweep, additional sweeps from 0-15 V would reproducibly yield the characteristic 'switching' *I-V* behavior shown Fig 5D.

2.6.3 Electron and Raman Microscopy

SEM imaging was performed with an FEI Helios 600 Nanolab Dual Beam system with an imaging resolution <5 nm using a typical acceleration voltage of 5 kV and imaging current of 86 pA. Raman imaging was performed with a Renishaw inVia Raman microscope using a HeNe laser source at 633 nm and 50x objective. Spectra were collected by raster scanning the sample in steps of 100 nm using an averaging time of 1.0 s. Prior to Raman image collection, the Au-coated substrates were immersed in an aqueous solution of methylene blue (Aldrich), rinsed with water, and dried with flowing N_2. Three-dimensional plots of the Raman signal were generated by summing all counts within the 1580-1650 cm^{-1} spectral window.

2.6.4 Finite-Element simulations

Optical and device simulations were performed using the Comsol Multiphysics commercial software package. Three-dimensional optical simulations were implemented using the total-field, scattered-field method. The background field was evaluated with a plane wave normally-incident on the substrate using periodic boundary conditions on the four horizontal boundaries, a perfectly matched layer (PML) on the lower boundary, and the plane wave source on the upper boundary. The scattered field was then solved after adding the Si/Au plasmonic structure to the simulation domain and replacing all boundaries with PMLs. Images of the surface plasmon modes were generated by evaluating the scattered electric field intensity ($|E|^2$) in a horizontal plane 3 nm above the top surface of the NW. Finite-element device simulations were performed using a modification of our previously published model[50] and used cylindrical symmetry to represent the three-dimensional structure. The external voltage was applied to Ohmic contacts on the n-type regions, and the simulations included realistic doping profiles as well as drift-diffusion and recombination processes to reproduce the I-V characteristics of the devices.

REFERENCES

1. Lieber, C. M., Semiconductor nanowires: A platform for nanoscience and nanotechnology. *MRS Bulletin* **2011,** *36*, 1052-1063.

2. Yang, P.; Yan, R.; Fardy, M., Semiconductor nanowire: what's next? *Nano Lett.* **2010,** *10* (5), 1529-1536.

3. Choi, C. L.; Alivisatos, A. P., From artificial atoms to nanocrystal molecules: Preparation and properties of more complex nanostructures. In *Annual Review of Physical Chemistry*, Leone, S. R.; Cremer, P. S.; Groves, J. T.; Johnson, M. A.; Richmond, G., Eds. Annual Reviews: Palo Alto, **2010**, pp 369-389.

4. Cui, Y.; Wei, Q.; Park, H.; Lieber, C. M., Nanowire nanosensors for highly sensitive and selective detection of biological and chemical species. *Science.* **2001,** *293* (5533), 1289-1292.

5. Law, M.; Sirbuly, D. J.; Johnson, J. C.; Goldberger, J.; Saykally, R. J.; Yang, P. D., Nanoribbon waveguides for subwavelength photonics integration. *Science* **2004,** *305* (5688), 1269-1273.

6. Lee, S.-H.; Jung, Y.; Agarwal, R., Highly scalable non-volatile and ultra-low-power phase-change nanowire memory. *Nat Nano* **2007,** *2* (10), 626-630.

7. Qian, F.; Li, Y.; Gradečak, S.; Wang, D.; Barrelet, C. J.; Lieber, C. M., Gallium nitride-based nanowire radial heterostructures for nanophotonics. *Nano Lett.* **2004,** *4* (10), 1975-1979.

8. Tian, B.; Kempa, T. J.; Lieber, C. M., Single nanowire photovoltaics. *Chem. Soc. Rev.* **2009,** *38* (1), 16-24.

9. Kempa, T. J.; Day, R. W.; Kim, S.-K.; Park, H.-G.; Lieber, C. M., Semiconductor nanowires: a platform for exploring limits and concepts for nano-enabled solar cells. *Energ Environ Sci* **2013,** *6* (3), 719-733.

10. Zhang, X.; Pinion, C. W.; Christesen, J. D.; Flynn, C. J.; Celano, T. A.; Cahoon, J. F., Horizontal silicon nanowires with radial p–n junctions: A platform for unconventional solar cells. *J. Phys. Chem. Lett.* **2013,** *4*, 2002-2009.

11. Hochbaum, A. I.; Yang, P. D., Semiconductor Nanowires for Energy Conversion. *Chemical reviews* **2010,** *110* (1), 527-546.

12. Wagner, R. S.; Ellis, W. C., Vapor-liquid-solid mechanism of single crystal growth. *Appl Phys Lett* **1964,** *4* (5), 89-90.

13. Li, Y.; Qian, F.; Xiang, J.; Lieber, C. M., Nanowire electronic and optoelectronic devices. *Materials Today* **2006,** *9* (10), 18-27.

14. Wu, Y. Y.; Fan, R.; Yang, P. D., Block-by-block growth of single-crystalline Si/SiGe superlattice nanowires. *Nano letters* **2002,** *2* (2), 83-86.

15. Gudiksen, M. S.; Lauhon, L. J.; Wang, J.; Smith, D. C.; Lieber, C. M., Growth of nanowire superlattice structures for nanoscale photonics and electronics. *Nature.* **2002,** *415* (6872), 617-620.

16. Bjork, M. T.; Ohlsson, B. J.; Sass, T.; Persson, A. I.; Thelander, C.; Magnusson, M. H.; Deppert, K.; Wallenberg, L. R.; Samuelson, L., One-dimensional steeplechase for electrons realized. *Nano letters* **2002,** *2* (2), 87-89.

17. Eymery, J.; Rieutord, F.; Favre-Nicolin, V.; Robach, O.; Niquet, Y. M.; Froberg, L.; Martensson, T.; Samuelson, L., Strain and shape of epitaxial InAs/InP nanowire superlattice measured by grazing incidence X-ray techniques. *Nano letters* **2007,** *7* (9), 2596-2601.

18. Algra, R. E.; Verheijen, M. A.; Borgstrom, M. T.; Feiner, L.-F.; Immink, G.; van Enckevort, W. J. P.; Vlieg, E.; Bakkers, E. P. A. M., Twinning superlattices in indium phosphide nanowires. *Nature* **2008,** *456* (7220), 369-372.

19. Laocharoensuk, R.; Palaniappan, K.; Smith, N. A.; Dickerson, R. M.; Werder, D. J.; Baldwin, J. K.; Hollingsworth, J. A., Flow-based solution-liquid-solid nanowire synthesis. *Nat Nano* **2013,** *8* (9), 660-666.

20. Yang, C.; Zhong, Z.; Lieber, C. M., Encoding Electronic Properties by Synthesis of Axial Modulation-Doped Silicon Nanowires. *Science* **2005,** *310* (5752), 1304-1307.

21. Ross, F. M.; Tersoff, J.; Reuter, M. C., Sawtooth Faceting in Silicon Nanowires. *Physical Review Letters* **2005,** *95* (14), 146104.

22. Lilach, Y.; Zhang, J. P.; Moskovits, M.; Kolmakov, A., Encoding morphology in oxide nanostructures during their growth. *Nano letters* **2005,** *5* (10), 2019-2022.

23. Tian, B.; Xie, P.; Kempa, T. J.; Bell, D. C.; Lieber, C. M., Single-crystalline kinked semiconductor nanowire superstructures. *Nat. Nanotechnol.* **2009,** *4* (12), 824-829.

24. Chueh, Y. L.; Fan, Z. Y.; Takei, K.; Ko, H.; Kapadia, R.; Rathore, A. A.; Miller, N.; Yu, K.; Wu, M.; Haller, E. E.; Javey, A., Black Ge based on crystalline/amorphous core/shell nanoneedle arrays. *Nano letters* **2010,** *10* (2), 520-523.

25. Musin, I. R.; Boyuk, D. S.; Filler, M. A., Surface chemistry controlled diameter-modulated semiconductor nanowire superstructures. *J. Vac. Sci. Technol. B* **2013,** *31* (2), 020603-5.

26. Lim, S. K.; Crawford, S.; Haberfehlner, G.; Gradečak, S., Controlled modulation of diameter and composition along individual III–V nitride nanowires. *Nano letters* **2013,** *13* (2), 331-336.

27. Crawford, S.; Lim, S. K.; Gradečak, S., Fundamental Insights into Nanowire Diameter Modulation and the Liquid/Solid Interface. *Nano letters* **2013**.

28. Kline, T. R.; Tian, M. L.; Wang, J. G.; Sen, A.; Chan, M. W. H.; Mallouk, T. E., Template-grown metal nanowires. *Inorg. Chem.* **2006,** *45* (19), 7555-7565.

29. Qin, L. D.; Park, S.; Huang, L.; Mirkin, C. A., On-wire lithography. *Science* **2005,** *309* (5731), 113-115.

30. Zheng, G. F.; Lu, W.; Jin, S.; Lieber, C. M., Synthesis and fabrication of high-performance n-type silicon nanowire transistors. *Adv. Mater.* **2004,** *16* (21), 1890-1893.

31. Wang, Y. F.; Lew, K. K.; Ho, T. T.; Pan, L.; Novak, S. W.; Dickey, E. C.; Redwing, J. M.; Mayer, T. S., Use of phosphine as an n-type dopant source for vapor-liquid-solid growth of silicon nanowires. *Nano letters* **2005,** *5* (11), 2139-2143.

32. Schmid, H.; Bjork, M. T.; Knoch, J.; Karg, S.; Riel, H.; Riess, W., Doping limits of grown in situ doped silicon nanowires using phosphine. *Nano letters* **2009,** *9* (1), 173-177.

33. Seidel, H.; Csepregi, L.; Heuberger, A.; Baumgartel, H., Anisotropic etching of crystalline silicon in alkaline solutions. 2. Influence of dopants. *Journal of the Electrochemical Society* **1990,** *137* (11), 3626-3632.

34. Kempa, T. J.; Tian, B.; Kim, D. R.; Hu, J.; Zheng, X.; Lieber, C. M., Single and tandem axial p-i-n nanowire photovoltaic devices. *Nano Lett.* **2008,** *8* (10), 3456-3460.

35. Cohen-Karni, T.; Casanova, D.; Cahoon, J. F.; Qing, Q.; Bell, D. C.; Lieber, C. M., Synthetically encoded ultrashort-channel nanowire transistors for fast, pointlike cellular signal detection. *Nano letters* **2012,** *12* (5), 2639-2644.

36. Perea, D. E.; Hemesath, E. R.; Schwalbach, E. J.; Lensch-Falk, J. L.; Voorhees, P. W.; Lauhon, L. J., Direct measurement of dopant distribution in an individual vapour-liquid-solid nanowire. *Nat. Nanotechnol.* **2009,** *4* (5), 315-319.

37. Schmid, H.; Bjork, M. T.; Knoch, J.; Riel, H.; Riess, W.; Rice, P.; Topuria, T., Patterned epitaxial vapor-liquid-solid growth of silicon nanowires on Si(111) using silane. *Journal of Applied Physics* **2008,** *103* (2), 024304.

38. Wen, C. Y.; Reuter, M. C.; Bruley, J.; Tersoff, J.; Kodambaka, S.; Stach, E. A.; Ross, F. M., Formation of compositionally abrupt axial heterojunctions in silicon-germanium nanowires. *Science.* **2009,** *326* (5957), 1247-1250.

39. He, R. R.; Feng, X. L.; Roukes, M. L.; Yang, P. D., Self-transducing silicon nanowire electromechanical systems at room temperature. *Nano letters* **2008,** *8* (6), 1756-1761.

40. Lindquist, N. C.; Nagpal, P.; McPeak, K. M.; Norris, D. J.; Oh, S. H., Engineering metallic nanostructures for plasmonics and nanophotonics. *Rep. Prog. Phys.* **2012,** *75* (3), 036501.

41. Hochbaum, A. I.; Chen, R.; Delgado, R. D.; Liang, W.; Garnett, E. C.; Najarian, M.; Majumdar, A.; Yang, P., Enhanced thermoelectric performance of rough silicon nanowires. *Nature.* **2008,** *451* (7175), 163-167.

42. Zianni, X., Diameter-modulated nanowires as candidates for high thermoelectric energy conversion efficiency. *Appl Phys Lett* **2010,** *97* (23), 233106.

43. Willets, K. A.; Van Duyne, R. P., Localized surface plasmon resonance spectroscopy and sensing. In *Annu. Rev. Phys. Chem.*, Annual Reviews: Palo Alto, **2007**, pp 267-297.

44. Schuller, J. A.; Barnard, E. S.; Cai, W.; Jun, Y. C.; White, J. S.; Brongersma, M. L., Plasmonics for extreme light concentration and manipulation. *Nature Materials* **2010,** *9* (3), 193-204.

45. Barnard, E. S.; White, J. S.; Chandran, A.; Brongersma, M. L., Spectral properties of plasmonic resonator antennas. *Optics Express* **2008,** *16* (21), 16529-16537.

46. Pedano, M. L.; Li, S. Z.; Schatz, G. C.; Mirkin, C. A., Periodic electric field enhancement along gold rods with nanogaps. *Angewandte Chemie-International Edition* **2010,** *49* (1), 78-82.

47. Li, S. Z.; Pedano, M. L.; Chang, S. H.; Mirkin, C. A.; Schatz, G. C., Gap Structure Effects on Surface-Enhanced Raman Scattering Intensities for Gold Gapped Rods. *Nano letters* **2010,** *10* (5), 1722-1727.

48. Yao, J.; Sun, Z.; Zhong, L.; Natelson, D.; Tour, J. M., Resistive switches and memories from silicon oxide. *Nano letters* **2010,** *10* (10), 4105-4110.

49. Yao, J.; Zhong, L.; Natelson, D.; Tour, J. M., In situ imaging of the conducting filament in a silicon oxide resistive switch. *Scientific Reports* **2012,** *2*.

50. Christesen, J. D.; Zhang, X.; Pinion, C. W.; Celano, T. A.; Flynn, C. J.; Cahoon, J. F., Design principles for photovoltaic devices based on Si nanowires with axial or radial p–n junctions. *Nano letters* **2012,** *12* (11), 6024-6029.

51. Kallesoe, C.; Molhave, K.; Larsen, K. F.; Engstrom, D.; Hansen, T. M.; Boggild, P.; Martensson, T.; Borgstrom, M.; Samuelson, L., Integration, gap formation, and sharpening of III-V heterostructure nanowires by selective etching. *J. Vac. Sci. Technol. B* **2010,** *28* (1), 21-26

CHAPTER 3: IDENTIFYING CRYSTALLIZATION AND INCORPORATION LIMITED REGIMES DURING VAPOR-LIQUID-SOLID GROWTH OF SI NANOWIRES[1]

3.1 Introduction

Semiconductor NWs have been widely explored as a fundamental building block of nanoscale devices[1-2] that can be used for optoelectronics,[3-4] photovoltaics,[5-8] and electronics.[9-11] NWs are typically synthesized by the VLS mechanism, which was originally proposed by Wagner and Ellis fifty years ago.[12-14] In the VLS process, vapor-phase semiconductor material is supplied to a metal catalyst, which forms a liquid alloy droplet because of a low eutectic temperature between the metal and semiconductor. For example, the eutectic temperature for Au and Si is ~363 °C (see the binary phase diagram in Figure 3.1A), enabling the formation of liquid droplets composed of ~20% Si above this temperature. During VLS growth, supersaturation of the liquid catalyst induces crystallization of the semiconductor material and elongation of the NW at the liquid-solid interface. These general aspects of the VLS mechanism are well known; however, the microscopic kinetic and physical processes that determine the overall NW growth rate remain poorly understood and debated in the literature.

The VLS process has been demonstrated with a range of semiconductor materials including group IV Si,[12-13] Ge,[15] and group III-V GaAs,[16] GaN,[17] InP,[18] etc materials as well as a range of metal catalysts including Au,[12-13] Ag,[19] Pt,[20-21] etc. For NW-based technologies, synthetic control

[1] This chapter previously appeared as an article in ACS Nano. The original citation is as follows: Pinion, C. W.; Nenon, D. P.; Christesen, J. D.; Cahoon, J. F., Identifying Crystallization- and Incorporation-Limited Regimes during Vapor-Liquid-Solid Growth of Si Nanowires. ACS Nano 2014, 8 (6), 6081-6088.

of the VLS process has been used to control NW size,[22-23] composition,[16, 24-25] and morphology[11, 26-28] in order to encode specific functionality in the NW material. For group IV NWs, low-pressure CVD with Au catalysts is often used for VLS growth in conjunction with hydride precursor gases such as silane (SiH_4), disilane (Si_2H_6), germane (GeH_4), and digermane (Ge_2H_6). The relatively low decomposition temperatures of these precursors enable nucleation and growth of NWs by the VLS process at temperatures close to, or even below,[29] the eutectic temperature.

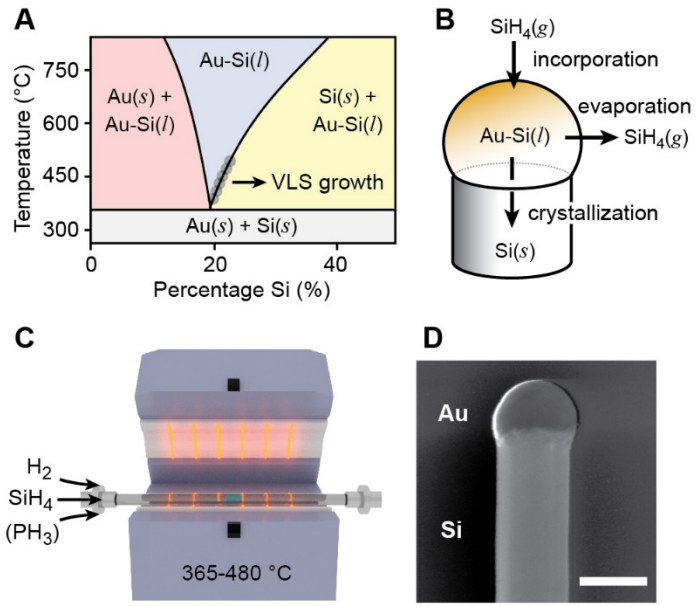

Figure 3.1: VLS growth of Si NWs by CVD

(A) Binary Au-Si phase diagram showing regions of solid Au, liquid Au-Si alloy, and solid Si as a function of weight percent Si. The approximate regions of the diagram accessed during the VLS growth are depicted by gray circles. (B) Illustration of the three key processes—incorporation, evaporation, and crystallization—that are used to model Si NW growth by the VLS mechanism. (C) Schematic of the hot-wall, low-pressure CVD system used for synthesis of Si NWs at temperatures of 365-480 °C. (D) SEM image of a Si NW grown using an Au catalyst ~150 nm in diameter; scale bar, 150 nm.

In this chapter, we discuss the VLS mechanism in the context of the three microscopic processes—incorporation, evaporation, crystallization—depicted in Fig. 3.1B. The incorporation process encompasses dissociative adsorption of silane gas on the Au-Si liquid surface and incorporation of Si into the liquid catalyst. The evaporation process corresponds to the reverse

reaction, or associative desorption of silane gas from the Au-Si liquid surface. Finally, the crystallization process describes the nucleation of solid Si crystal planes at the liquid-solid interface, which irreversibly elongates the NW. We neglect diffusion in the Au-Si liquid catalyst because it is too rapid to be a rate-limiting step in small diameter NWs[20, 30] and also neglect diffusion of adsorbed Si on the substrate or NW surface, which has been shown to be of minimal importance for Si NW growth.[31] With a few exceptions,[32-33] reports on the kinetics of Si NW VLS growth generally do not include a Si evaporation or desorption process in the analysis. However, considering the principle of microscopic reversibility there is no *a priori* rational to exclude this reaction.

The rate-limiting step for NW growth has been debated because experimental and theoretical reports have produced conflicting results.[15, 20-21, 30-31, 34-37] For instance, Bootsma and Gassen observed a growth rate proportional to the partial pressure of silane and thus proposed an incorporation-limited mechanism.[15] More recently, Lew and Redwing reported similar results, also concluding that incorporation was the rate-limiting step.[30] In contradiction, Givargizov proposed a crystallization-limited mechanism because wires growing along different crystallographic directions exhibited different growth rates.[20]

Further information on the rate-limiting step is provided by the diameter dependence of the growth rate,[31, 35] and it is widely agreed that either the curvature of the cylindrical NW or spherical catalyst droplet induces diameter dependence in the growth rate as a result of the Gibbs-Thomson effect.[20, 33, 35-36, 38] Givargizov reported a decreasing growth rate with decreasing NW diameter, which he attributed to the Gibbs-Thomson effect reducing the catalyst chemical potential and thus the crystallization rate.[20] In a more recent study by Ross *et al*., however, a diameter-independent growth rate was observed when using Si_2H_6 as the Si precursor at low pressures ($<10^{-5}$ Torr).[31]

They concluded that VLS growth proceeds by an incorporation-limited mechanism. In addition, several recent theoretical studies have shown that the NW growth process involves coupled processes and cannot necessarily be reduced to a single rate-limiting step.[33, 35]

3.2 Experimental Design

To help resolve the long-standing ambiguities about the VLS growth process, we performed precise experimental measurements on the growth rate of Au catalyzed Si NWs over a range of temperatures (365-480 °C), diameters (30-200 nm), and pressures (0.1-1.6 Torr SiH_4). NWs were synthesized in a hot-wall, quartz-tube CVD reactor (see schematic in Fig. 3.1C) using silane as the Si precursor, phosphine (PH_3) for n-type doping with phosphorus, and hydrogen (H_2) as the carrier gas (see section 3.7.1 details of NW growth). The NW diameter was controlled by the size of the Au catalysts deposited on growth substrates. The CVD apparatus and growth conditions used for our experiments are similar to those used widely within the NW community for group IV materials.[22, 39-40] All synthetic conditions used in this study produce high-quality, single-crystalline NWs, as exemplified by the scanning electron microscopy (SEM) image in Fig. 3.1D.

As shown in Fig. 3.2, growth rate data was generated using a modification of our recently reported method, ENGRAVE (Encoded Nanowire GRowth and Appearance using VLS and Etching),[11] to sequentially encode n-type and intrinsic sections in the NWs at various temperatures and SiH_4 partial pressures. Selective wet-chemical etching of the intrinsic sections (see Fig. 3.2A) was used to reveal the length of individual sections, and quantitative SEM image analysis (see Fig. 3.2B) yielded the measured growth rate for each section. For each unique combination of temperature, pressure, and diameter, more than 50 individual measurements of the growth rate were made across 10 or more NWs to ensure the statistical significance of the results. No

significant difference in the growth rate of n-type and intrinsic sections was observed. This method has previously been used to measure NW growth rates in both VLS[11] and VSS[41] mechanisms.

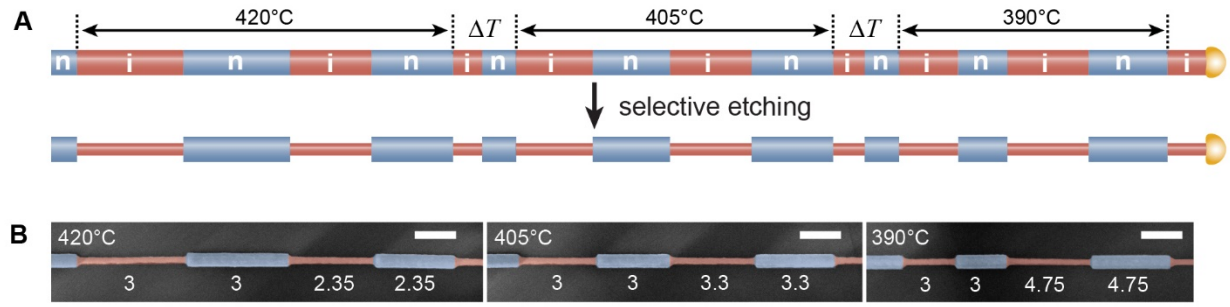

Figure 3.2: Determination of Si NW VLS growth rates using dopant modulation

(A) Upper: Schematic illustration of alternating n-type (n) and intrinsic (i) segments encoded sequentially during VLS NW growth at temperatures of 420, 405, and 390 °C. Sections denoted ΔT are not drawn to scale and correspond to regions over which the temperature was lowered at a rate of 1 °C/min. Lower: Illustration of the NW morphology that results from etching in aqueous KOH solution, which selectively removes intrinsic sections (red) of the NW. (B) False-colored SEM images of a Si NW ~80 nm in diameter with sequential segments encoded at 420 (left), 405 (middle), and 390 °C (right). Growth times in minutes are denoted beneath each segment, and all segments were grown at a SiH_4 partial pressure of 0.4 Torr and total pressure of 40 Torr; scale bars, 250 nm. Analysis of these type of SEM images yielded quantitative temperature- and diameter-dependent growth rates.

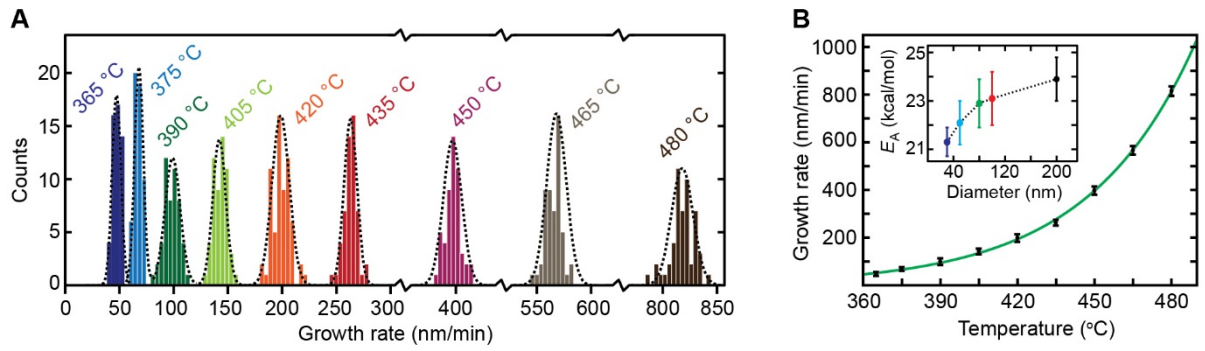

Figure 3.3: Temperature-dependent Si NW VLS growth rates

(A) Histogram of measured VLS growth rates acquired at temperatures ranging from 365 to 480 °C for NWs 80 nm in diameter at an SiH_4 partial pressure of 0.4 Torr. Dashed lines represent a fit of the data at each temperature to a Gaussian distribution. (B) Plot of growth rate vs. temperature for the data contained in panel A; error bars reflect two standard deviations (2σ). The solid green line represents a fit to the Arrhenius expression. Inset: activation energy as a function of NW diameter, as determined by fits to growth rate data for NWs 30 to 200 nm in diameter.

3.3 Results

Growth rate data collected at one diameter (80 nm) and one partial pressure (0.4 Torr SiH_4) for a range of temperatures are depicted as histograms in Fig. 3.3A. The data at each temperature are well fit to a Gaussian distribution, producing a standard deviation of <8% of the average growth rate value. The dependence of growth rate on temperature (Fig. 3.3B) is well fit to the Arrhenius expression, yielding an activation energy of 22.9 ± 1.0 kcal/mol that is in good agreement with literature values.[15, 30-31, 34, 42-43] Similar analysis was performed for other diameters and partial pressures (see Figs. 3.9 and 3.10). Interestingly, we observe a diameter-dependent activation energy (see inset Fig. 3.3B), which, to our knowledge, has not been previously observed and is

consistent with the enhanced catalytic activity observed with small-diameter Noble metal nanoparticles.[44-45]

Growth rate data for diameters of 30-200 nm at a SiH_4 partial pressure of 0.4 Torr are displayed as a function of temperature in Fig. 3.4A. For temperatures of 390 °C and below, we observed no statistically significant differences in the growth rates for NWs of different diameter. However, for temperatures of 435 °C and above, we observed definitively faster growth rates for larger diameter NWs. Growth rate data is plotted as a function of NW diameter in Fig. 3.4B. Low temperatures show no dependence on diameter whereas higher temperatures show a non-linear dependence, exhibiting growth rates that asymptotically increase with increasing diameter.

As shown in Fig. 3.4C, we also examined the effect of SiH_4 partial pressure on the Si NW growth rate. The pressure-dependent growth rates are not linear over the full range of synthetic conditions examined—an observation in disagreement with previous studies that reported a purely linear dependence.[30-31] For the 420 °C data at low partial pressures (<0.2 Torr), the growth rate is diameter independent but at higher partial pressures (>0.2 torr) becomes diameter dependent (see inset in Fig. 3.4C). However, at 390 °C the growth rate is diameter-independent for all SiH_4 partial pressures measured (see Fig. 3.5).

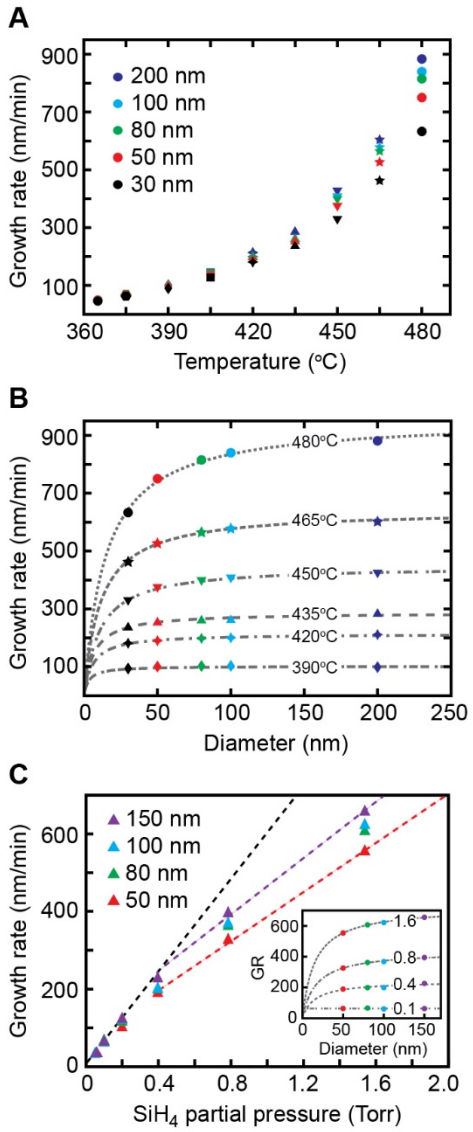

Figure 3.4: Diameter-dependent Si NW VLS growth rates

(A) Diameter-dependent growth rates as a function of temperature for Si NWs with diameters of 30 (black), 50 (red), 80 (green), 100 (blue), and 200 nm (indigo) at a SiH_4 partial pressure of 0.4 Torr. (B) NW growth rate as a function of diameter for temperatures of 390 (diamond), 420 (square), 435 (triangle), 450 (inverted triangle), 465 (star), and 480 °C (circle). Dashed lines represent a fit of the data at each temperature to equation 9. (C) NW growth rate as a function of silane partial pressure for NW diameters of 50 (red), 80 (green), 100 (blue), and 150 nm (purple).

Dashed lines represent linear fits to the data. For partial pressures <0.3 Torr, all diameters were fit simultaneously (dashed black line). For partial pressures >0.3 Torr, the 150 nm (dashed purple) and 50 nm (dashed red) data were fit separately. Inset: NW growth rate (GR; nm/min) at 420 °C as a function of diameter for SiH_4 partial pressures ranging from 0.1-1.6 Torr. Dashed gray lines represent fits to equation 9. For all panels A-C, error bars are comparable in size to the marker symbols and omitted for clarity.

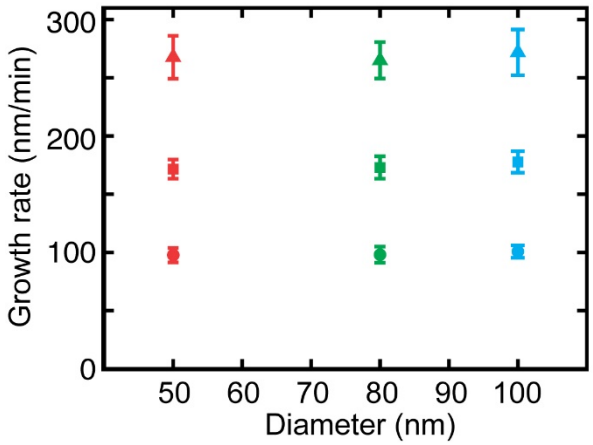

Figure 3.5: Si NW growth rates at 390 °C for various partial pressures.

Diameter-independent growth kinetics at 390 °C for partial pressures of 0.4 Torr (circles), 0.8 Torr (squares), and 1.6 Torr (triangles). Plot marker color indicates NW diameter. Error bars are one standard deviation.

3.4 Kinetic Modeling

To interpret the measured growth rate data, a kinetic analysis of VLS growth in the context of the three microscopic processes depicted in Fig. 3.1B—incorporation, evaporation, and crystallization—is developed below. This analysis builds most directly on the work of Shakthivel and Raghavan.[33] An illustration of the kinetic processes and energy landscape for the VLS process

in this analysis is depicted in Fig. 3.6.

We consider a mechanism in which the incorporation step is reversible:

$$\mathrm{SiH_4}(g) \underset{k_e}{\overset{k_i}{\rightleftharpoons}} \mathrm{Si}(l) + 4\mathrm{H}\text{-}, \qquad \text{(eq. 3.1)}$$

and the crystallization step is irreversible:

$$\mathrm{Si}(l) \xrightarrow{k_c} \mathrm{Si}(s), \qquad \text{(eq. 3.2)}$$

where H- represents surface adsorbed hydrogen, k_i the incorporation rate constant (units of s^{-1}), k_e the evaporation rate constant (units of $nm \cdot s^{-1}$), and k_c the crystallization rate constant (units of $nm \cdot s^{-1}$). The irreversible reaction in equation 2 implicitly assumes that the supersaturation of the Au-Si droplet and the liquid-solid chemical potential, μ_{LS}, are sufficiently high to irreversibly drive the crystallization process under all synthetic conditions. A full analysis of equations 1 and 2 under steady-state conditions, which includes the effects of surface-confined reactions at the liquid-vapor and liquid-solid interfaces (which introduces units of length to k_e and k_c), yields a NW growth rate, G, of (see section 3.8 for a full derivation):

$$G = \frac{k_c\, k_i}{k_e + k_c/2}\, \Omega\, \rho_{sites}\, K_{a/d}\, P\,, \qquad \text{(eq. 3.3)}$$

where Ω is the volume per atom for Si, $K_{a/d}$ is the silane adsorption/desorption equilibrium constant (units of inverse pressure), ρ_{sites} is the density of surface sites available for SiH_4 adsorption, and P is the partial pressure of SiH_4 in the reactor. Note the quantity $K_{a/d} \cdot P$ equals the fractional saturation, θ, of SiH_4 adsorption sites and would be expected to saturate (i.e. $\theta = 1$) at sufficiently high P. Equation 3.3 also assumes that the NW and liquid droplet diameters are equal, introducing the factor of 2 in the denominator.

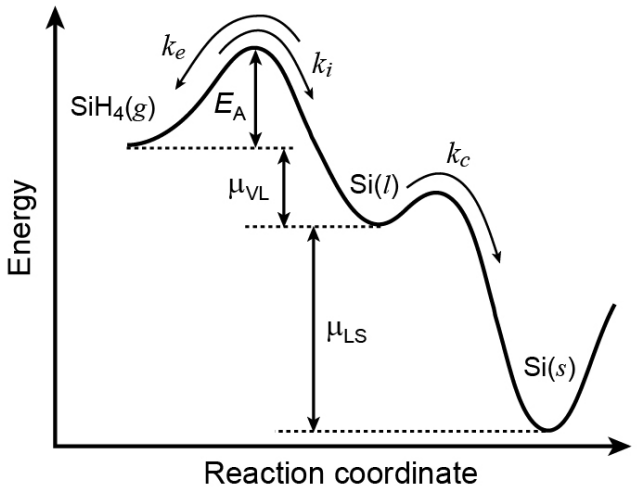

Figure 3.6: The kinetics and energetics of VLS NW growth.

Energy landscape for the VLS mechanism, depicting the barriers and rate constants associated with incorporation, evaporation, and crystallization processes that govern the kinetics leading from gaseous SiH_4 to liquid AuSi to solid diamond-cubic Si.

Each rate constant in equation 3 can potentially have dependencies on temperature and diameter. In this analysis, however, we assume k_i is simply described by the Arrhenius expression, yielding the activation energies, E_A, depicted in the inset of Fig. 3.3B. Although k_c may have a similar Arrhenius-type dependence on temperature that depends on the mechanism of crystallization,[33] we assume that the barrier to crystallization is substantially lower than the incorporation barrier[46] and thus neglect this temperature dependence for the temperature range examined in this study and treat k_c as a constant value.

The Gibbs-Thomson effect, which changes the chemical potential of Si within the catalyst droplet, appears through the dependence of k_e on NW diameter. The chemical potential difference between Si in the vapor and liquid phases, μ_{VL}, is given by:[33]

$$\mu_{VL} = k_B T \ln\left(\frac{P}{P_o}\right) - k_B T \ln\left(\frac{C_{Si(l)}}{C_o}\right) - \frac{4\,\Omega\,\gamma_{VL}}{d}, \qquad \text{(eq. 3.4)}$$

where k_B is the Boltzmann constant, T is the temperature, P_o is the vapor pressure of Si in the solid NW, $C_{Si(l)}$ is the concentration of Si in the supersaturated liquid droplet, C_o is the equilibrium concentration of Si in the liquid droplet, γ_{VL} is the vapor-liquid surface tension of the droplet, and d is the diameter of the NW. The final term in equation 3.4, which scales as d^{-1}, accounts for the decrease of μ_{VL} as a result of the curved liquid surface, which is commonly referred to as the Gibbs-Thomson effect. As indicated by the plot in Fig. 3.6, the energetic barrier for the evaporation process is the summation of E_A and μ_{VL}, yielding an Arrhenius-type expression for k_e of:[33]

$$k_e = A \exp\left(\frac{-(E_A+\mu_{VL})}{kT}\right), \quad \text{(eq. 3.5)}$$

where A is a pre-factor with units of nm·s^{-1}. Substituting equation 3.4 into equation 3.5 and simplifying to first order yields:

$$k_e = A \exp\left(\frac{-E_A}{kT}\right)\left(\frac{P_o}{P}\right)\left(\frac{C_{Si(l)}}{C_o}\right)\exp\left(\frac{4\,\Omega\,\gamma_{VL}}{d\,kT}\right) \approx A \exp\left(\frac{-E_A}{kT}\right)\left(\frac{P_o}{P}\right)\left(\frac{C_{Si(l)}}{C_o}\right)\left(1+\frac{4\,\Omega\,\gamma_{VL}}{d\,kT}\right). \quad \text{(eq 3.6)}$$

Therefore, k_e includes a d^{-1} dependence as a result of the Gibbs-Thomson effect. Note that we assume pseudo first-order kinetics with the respect the adsorbed hydrogen concentration (*i.e.* we assume saturated H- coverage); thus, the pre-factor in equation 6 includes a term proportional to the hydrogen coverage (see section 3.8).

Based on this analysis, two limits of equation 3.3 can be examined. First, for $k_c > 2k_e$, the growth rate becomes:

$$G \approx 2\,k_i\,\Omega\,\rho_{sites}\,K_{a/d}P\,, \quad \text{(eq 3.7)}$$

and a diameter dependence is not expected as k_e does not appear in the expression. This limit can be considered an incorporation-limited regime because only k_i appears in the expression. Second, for the limit $k_c < 2k_e$, the growth rate becomes:

$$G \approx \frac{k_i\,k_c}{k_e}\Omega\,K_{a/d}\,\rho_{sites}P = K_{eq}k_c\Omega\,K_{a/d}\,\rho_{sites}P, \quad \text{(eq 3.8)}$$

where $K_{eq} = k_i \cdot k_e^{-1}$ (units of nm^{-1}) is the equilibrium constant for incorporation/evaporation, and, as a result, the growth rate is dependent on diameter and scales as $(1+4\Omega\gamma_{VL}/dk_BT)^{-1}$. This limit can be considered a crystallization-limited regime because the slower rate of crystallization relative to incorporation/evaporation induces an equilibrium between incorporation/evaporation; consequently, the growth rate scales as $K_{eq} \cdot k_c$.

3.5 Analysis and Discussion

The kinetic analysis presented above yields a diameter-independent, incorporation-limited regime (equation 3.7) and a diameter-dependent, crystallization-limited regime (equation 3.8). The key mechanistic aspects of each regime are illustrated in Fig. 3.7A and 3.7B, respectively. By classifying our experimental data into these two regimes using the measured diameter dependence, we can generate the 'phase' diagram depicted in Fig. 3.7C, in which the incorporation-limited regime (red region) is observed at low temperatures and SiH_4 partial pressures and the crystallization-limited regime (green region) is observed at higher temperatures and pressures. There is a narrow window (blue region) over which we cannot conclusively discern the diameter dependence and thus cannot classify the growth regime.

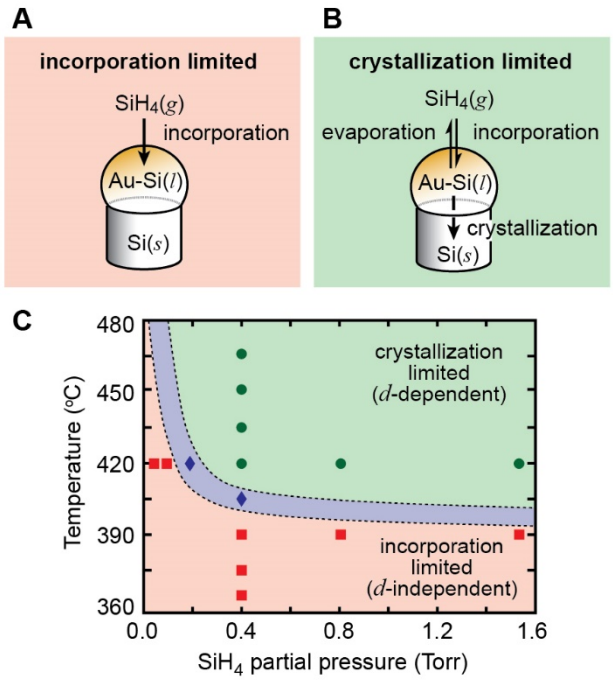

Figure 3.7. Identification of crystallization-limited and incorporation-limited regimes during VLS NW growth.

(A) Illustration of the key kinetic processes for the incorporation-limited (diameter-independent) regime, which is dominated by the rate of Si incorporation from the gas phase. (B) Illustration of the key kinetic processes for the crystallization-limited (diameter-dependent) regime, which includes rapid gas-liquid equilibration and slower Si crystallization. (C) 'Phase' diagram depicting regions of temperature and silane partial pressure in which VLS growth is crystallization limited (shaded green), incorporation limited (shaded red), or intermediate (shaded blue). Red squares denote synthetic conditions with a diameter-independent growth rate, green circles a diameter-dependent growth rate, and blue diamonds the transition between diameter-independent and diameter-dependent regimes.

The appearance of the incorporation-limited regime at low temperature is consistent with the limit ($2k_e < k_c$) taken for equation 3.7 because k_e is expected to be suppressed at lower

temperatures as a result of the large energetic barrier, $E_A+\mu_{VL}$, for evaporation. Interestingly, at an intermediate temperature of 420 °C, we observe a transition from the incorporation-limited to crystallization-limited regime as the SiH_4 partial pressure increases. This observation is consistent with the results of Ross *et al.,*[31] in which an incorporation-limited and diameter-independent regime was observed for very low ($<10^{-5}$ Torr) partial pressures at all temperatures. The transition observed here at higher (>0.2 Torr) partial pressures implies the limit $2k_e > k_c$ at higher pressures. The dependence of k_e on partial pressure, P, is complex, because the catalyst supersaturation and hydrogen surface coverage should both increase with P, potentially offsetting the P_o/P dependence in equation 3.6. This observation suggests the need for additional pressure-dependent studies in the transitional region shown in blue in Fig. 3.7C to further understand the details of the processes that control the transition from diameter-independent to dependent regimes at constant temperature.

For data collected in the crystallization-limited regime, the diameter dependence of the growth rate can be fit using a simplification of equation 3.8 to:

$$G \approx \frac{B}{1+d_o/d}, \qquad \text{(eq. 3.9)}$$

where $d_o = 4\Omega\gamma_{VL}/k_BT$ (units of nm) and B is a proportionality constant. Fits of diameter-dependent data to this expression are shown in Fig. 3.4B and reproduce the diameter-dependent increase in G with increasing NW diameter. Using the values for d_o from these fits, we can estimate the vapor-liquid surface tension, γ_{VL}, yielding values of 0.7 ± 0.3, 0.8 ± 0.5, 1.3 ± 0.2, 1.4 ± 0.2, and 1.9 ± 0.5 J/m^2 for temperatures of 420, 435, 450, 465, and 480 ^oC, respectively. These values are in reasonably good agreement with reported values for liquid Si, 0.7-0.8 J/m^2,[47] and liquid Au, 1.0-1.2 J/m^2,[48] near their melting temperatures. The increasing γ_{VL} with temperature suggests that the liquid contact angle at the VLS triple junction should decrease with temperature.[49] SEM images

of Au catalysts at 420 and 480 °C (see Fig. 3.8) show a decrease in the contact angle by ~15°, confirming the trend observed with γ_{VL}. These changes in γ_{VL} with temperature may suggest a change in composition of the AuSi liquid catalyst surface with temperature.[46, 50]

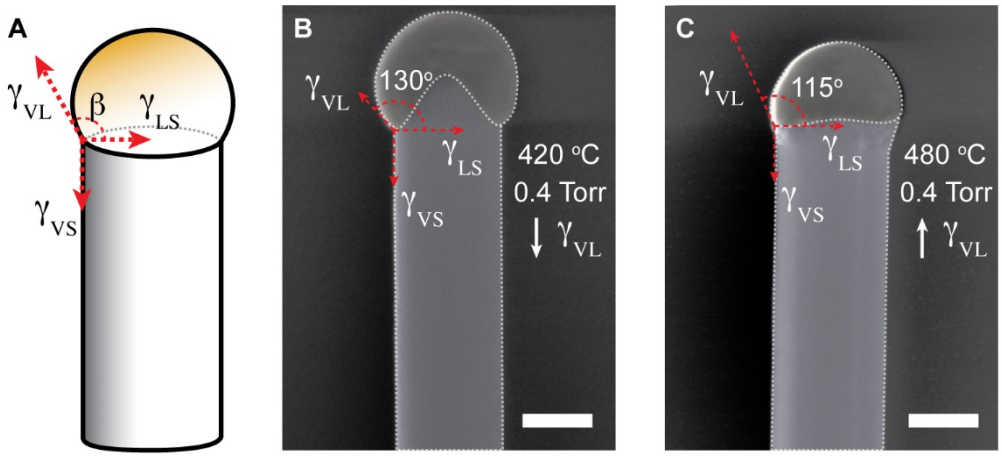

Figure 3.8. Catalyst morphology and contact angle at 420 °C and 480 °C.

(A) Schematic illustration of the three surface energies, γ_{VL}, γ_{VS}, γ_{LS} that dictate the catalyst contact angle, β, according to Young's Equation. (B) False-colored SEM image of a representative Si NW demonstrating the catalyst morphology and contact angle after quenching NW growth at 420 °C and 0.4 Torr SiH_4 partial pressure; scale bar, 100 nm. (C) False-colored SEM image of a representative Si NW demonstrating the catalyst morphology and contact angle after quenching NW growth at 480 °C and 0.4 Torr SiH_4 partial pressure; scale bar, 100 nm. When deriving the kinetic analysis we assumed a contact angle of $\beta = 90^{o}$ because the catalyst and NW diameters were assumed to be equal. If equation 9 from the main text is supplemented with a term to account for the contact angle, $d_o = 4\Omega\gamma_{VL}\sin(\beta)/k_BT$, the extracted values for γ_{VL} would change by ~10-30% based on the measured contact angles. However, we observe changes in γ_{VL} of more than a factor of two, implying the increasing γ_{VL} cannot solely be attributed to the absence of the sin(β)

term in d_o. Therefore, the decreased contact angle for higher temperatures is consistent with an increased liquid-vapor surface tension.

The appearance of incorporation- and crystallization-limited regimes also explains the non-linear dependence of growth rate on partial pressure that is apparent in Fig. 3.4C. An examination of equations 3.7 and 3.8 shows that the slopes of growth rate vs. pressure should be different in the two regimes. Separate fits of the pressure-dependent data for partial pressures below 0.3 Torr (dashed black) and above 0.3 Torr (dashed purple and dashed red lines) are shown in Fig. 3.4C, and approximately linear behavior is observed in both regimes. Furthermore, above 0.3 Torr, data from smaller diameter NWs exhibits a lower slope (red dashed line) relative to larger NWs (purple dashed line). This result is predicted by equation 8 because k_e increases with smaller diameters, reducing the slope for small diameter NWs in the crystallization-limited regime.

3.6 Conclusions

We performed comprehensive measurements of the Si NW VLS growth rate over a range of temperatures, pressures, and diameters that are widely used for development of NW-based technologies using CVD synthesis. By developing a kinetic analysis that includes the microscopic processes of incorporation, evaporation, and crystallization, NW growth was classified into a diameter-dependent, crystallization-limited regime and diameter-independent, incorporation-limited regime. Analysis of the experimental growth rate data revealed the incorporation regime to dominate at low temperatures and pressures whereas the crystallization-limited regime dominates at higher temperatures and pressures. The growth regime changes over a surprisingly narrow region of temperature and pressure during CVD growth.

In addition to fundamental insights on the mechanism of the VLS process, our analysis may be used to choose the synthetic conditions needed for specific technological applications. For

instance, if NWs of uniform length but different diameters are required, the incorporation-limited regime is appropriate. However, if NWs with abrupt axial transitions are needed, such as for heterostructures, the crystallization-limited regime is more appropriate because the liquid-vapor equilibrium will facilitate fast exchange of material in the liquid catalyst. Finally, we expect crystallization-limited and incorporation-limited regimes to be accessible for a range of semiconductor materials and metal catalysts. Thus, although the specific growth conditions may be different, we expect the insights into VLS growth discussed in this article to be applicable to a range NW systems.

3.7 Detailed Methods

3.7.1 Nanowire Growth

Si NWs were grown by a VLS mechanism in a home-built, hot-wall chemical vapor deposition (CVD) system using Au nanoparticles as catalysts, SiH_4 (Voltaix) as the source of Si, PH_3 (Voltaix; diluted to 1000 ppm in H_2) as the source of P for n-type doping, and H_2 (Matheson TriGas 5N semiconductor grade) as the carrier gas. The CVD system has been described in detail elsewhere.[11] For a typical NW growth run, citrate-stabilized Au catalysts (BBI International) of the indicated diameter were dispersed on 1 x 2 cm Si wafers (University Wafer; p-type Si with 600 nm thermal oxide) that had been functionalized with poly-L-lysine solution (Aldrich). These growth substrates were inserted into the center of a 1-inch diameter quartz-tube furnace (Lindberg Blue M), and the furnace temperature was ramped to 450 °C to nucleate NW growth for 5 min using 2.00 standard cubic centimeters per minute (sccm) SiH_4 and 200.0 sccm H_2 at 40.0 Torr total reactor pressure. Note that the reactor pressure and all partial pressures noted in the text correspond to external, room-temperature measurements of the pressure. The reactor temperature was altered in a stepwise manner as described in the text (see Fig. 3.2A). To prevent disruption of the NW

growth, all changes in temperature were performed at a rate of 1 °C/min. Similarly, changes in SiH_4 partial pressure were performed by incrementally altering the SiH_4 flow in sequential steps that increased the partial pressure by a factor of two or less. All n-type segments were encoded using a PH_3 flow rate needed to achieve a SiH_4:PH_3 gas-phase ratio of 400:1 or less.

3.7.2 Image Analysis

SEM imaging was performed with an FEI Helios 600 Nanolab Dual Beam system with an imaging resolution of less than 5 nm. The length of each n-type or intrinsic segment was determined from SEM images using home-written MATLAB image analysis software. An edge-finding algorithm was used to extract the NW diameter as a function of axial position, and the n-type/intrinsic boundary (*e.g.* from left to right in Fig. 3.2) was defined as the onset of a decrease in diameter. The subsequent intrinsic/n-type boundary was defined as the onset of an increase in diameter. We estimate the uncertainty in segment length to be ± 5 nm from repeated imaging and analysis of the same segments. The growth rate was calculated from the measured segment length and the growth time. The diameter of each NW (defined as the diameter of the Si wire at the base of the Au catalyst) was also measured in order to bin NWs into diameters of 30, 50, 80, 100, 150, and 200 nm corresponding to measured diameter ranges of 25-35, 45-55, 75-85, 95-105, 140-160, and 190-210 nm, respectively.

3.8 Derivation of Nanowire growth rate

We consider a mechanism in which the incorporation step is reversible whereas the crystallization step is irreversible:

$$\mathrm{SiH_4}(g) \underset{k_e}{\overset{k_i}{\rightleftharpoons}} \mathrm{Si}(l) + 4\ (\mathrm{H\text{-}}) \qquad \text{(eq. 3.10)}$$

$$\mathrm{Si}(l) \xrightarrow{k_c} \mathrm{Si}(s), \qquad \text{(eq 3.11)}$$

where H- represents surface adsorbed hydrogen, k_i is the incorporation rate constant, k_e the 'evaporation' rate constant, and k_c the crystallization rate constant. Each reaction is surface-confined, and the surface reaction rates must be converted into volumetric rates in order to calculate the NW growth rate. We consider the liquid catalyst to be a hemisphere with diameter equal to that of the NW, which gives a surface to volume ratio of $3/r$, where r is the radius of the NW. We begin with the surface rate of incorporation, which is given by:

$$\text{surface rate of incorporation} = k_i\, C_{SiH_4} = k_i\, \theta\, \rho_{sites} \qquad \text{(eq. 3.12)}$$

where k_i is the incorporation rate constant with units of inverse seconds, C_{SiH4} is the surface concentration of adsorbed SiH_4 species (#/nm^2), θ is the surface coverage, and ρ_{sites} is the density of surface sites (#/nm^2). The volumetric rate of incorporation is then:

$$\text{volumetric rate of incorporation} = k_i\, C_{SiH_4} \left(\frac{Area}{Volume}\right) = \frac{3\, k_i\, \theta\, \rho_{sites}}{r}, \qquad \text{(eq. 3.13)}$$

where r is the radius of the droplet. Within the context of the CVD system used to control the NW growth, we have direct control over the partial pressure of the SiH_4, which dictates the surface coverage, θ. Thus we express θ in terms of the SiH_4 partial pressure:

$$\text{volumetric rate of incorporation} = \frac{3\, k_i\, C_{SiH_4}}{r} = \frac{3\, k_i\, \rho_{sites}\, K_{a/d}\, P}{r} \qquad \text{(eq. 3.14)}$$

where $K_{a/d}$ is the adsorption/desorption equilibrium constant, with units of inverse pressure, and P is the SiH_4 partial pressure.

We now consider the evaporation process. The evaporation rate constant, k_e, defines the rate of surface evaporation as:

$$\text{surface rate of evaporation} = k_e\, C_{\mathrm{Si}(l)}, \qquad \text{(eq. 3.15)}$$

where k_e, as earlier, is given as:

$$k_e = A \exp\left(\frac{-E_A}{kT}\right) \left(\frac{P_o}{P}\right) \left(\frac{C_{\mathrm{Si}(l)}}{C_o}\right) \exp\left(\frac{4\, \Omega\, \gamma_{VL}}{d\, kT}\right), \qquad \text{(eq. 3.16)}$$

where P_o is the vapor pressure of solid Si in the NW, $C_{\mathrm{Si}(l)}$ is the concentration of Si in the liquid droplet, C_o is the equilibrium concentration of Si in the liquid droplet, γ_{VL} is the vapor-liquid surface tension of the liquid droplet, Ω is the volume/atom for Si, and d is the diameter of the NW ($d = 2r$). A is a constant with units of nm/s that includes surface adsorbed hydrogen concentration:

$$A = B\ [\mathrm{H}\text{-}]^4. \qquad \text{(eq. 3.17)}$$

From the surface rate of evaporation we arrive at the volumetric rate of evaporation:

$$\text{volumetric rate of evaporation} = k_e\ C_{\mathrm{Si}(l)} \left(\frac{Area}{Volume}\right) = \frac{3\ k_e\ C_{\mathrm{Si}(l)}}{r} \qquad \text{(eq. 3.18)}$$

We now consider the crystallization process. The surface rate of crystallization is given by:

$$\text{surface rate of crystallization} = k_c\ C_{\mathrm{Si}(l)} \qquad \text{(eq. 3.19)}$$

where k_c is the crystallization rate constant with units of nm/s. The volumetric rate of disappearance for $C_{\mathrm{Si}(l)}$ as a result of crystallization is:

$$\begin{matrix}\text{volumetric rate} \\ \text{of } C_{\mathrm{Si}(l)} \text{disappearance}\end{matrix} = k_c\ C_{\mathrm{Si}(l)} \left(\frac{Area}{Volume}\right) = k_c\ C_{\mathrm{Si}(l)} \left(\frac{\pi\ r^2}{2/3\pi\ r^3}\right) = \frac{3\ k_c\ C_{\mathrm{Si}(l)}}{2\ r}, \qquad \text{(eq. 3.10)}$$

where we assume the diameter (and radius) of the droplet and NW are equal. The volumetric rate of crystallization is given by:

$$\text{volumetric rate of crystallization} = k_c\ C_{\mathrm{Si}(l)}\ \pi\ r^2\ \Omega\ , \qquad \text{(eq. 3.11)}$$

Finally, we arrive at the NW growth rate, G, in nm/s by dividing the volumetric rate of crystallization by the area per crystal plane added:

$$G = \text{NW growth rate} = \Omega\ k_c\ C_{\mathrm{Si}(l)}\ . \qquad \text{(eq. 3.12)}$$

Therefore, in order to determine the growth rate, we require $C_{\mathrm{Si}(l)}$, which may be found by considering the volumetric rate of appearance and disappearance of each Si species:

$$\frac{dC_{SiH_4}}{dt} = -\frac{3\ k_i}{r}\ C_{SiH_4} + \frac{3\ k_e}{r}\ C_{\mathrm{Si}(l)}\ = 0 \qquad \text{(eq. 3.13)}$$

$$\frac{dC_{Si\ (l)}}{dt} = \frac{3\ k_i}{r}\ C_{SiH_4} - \frac{3\ k_e}{r} C_{Si\ (l)}\ - \frac{3\ k_c}{2r}\ C_{\mathrm{Si}(l)} \qquad \text{(eq. 3.14)}$$

$$\frac{dC_{\mathrm{Si}(s)}}{dt} = \frac{G}{\Omega} = k_c\, C_{\mathrm{Si}(l)} \qquad \text{(eq. 3.15)}$$

First, $\frac{dC_{SiH_4}}{dt}$ must be zero as a result of the SiH_4 partial pressure being fixed by the CVD system; thus, the value of C_{SiH_4} is a constant. This allows the direct integration of equation S15 to determine $C_{\mathrm{Si}(l)}(t)$:

$$C_{\mathrm{Si}(l)}(t) = \frac{k_i\, C_{SiH_4}}{\left(k_e + \frac{k_c}{2}\right)} \left(1 - \exp\left(-\frac{3\left(k_e + \frac{k_c}{2}\right)}{r}\, t\right)\right). \qquad \text{(eq. 3.16)}$$

Taking the long-time limit to arrive at steady-state conditions:

$$\lim_{t\to\infty} C_{\mathrm{Si}(l)}(t) = \frac{k_i}{\left(k_e + \frac{k_c}{2}\right)}\, C_{SiH_4} = \frac{k_i}{\left(k_e + \frac{k_c}{2}\right)} K_{a/d}\, \rho_{sites}\, P\,. \qquad \text{(eq. 3.17)}$$

Substituting this expression into Equation 3.12 yields Equation 3.3 from which the kinetic analysis is developed:

$$G = \Omega\, k_C\, C_{\mathrm{Si}(l)} = \frac{k_c\, k_i}{k_e + \frac{k_c}{2}}\, \Omega\, K_{a/d}\, \rho_{sites}\, P \qquad \text{(eq. 3.18)}$$

3.9 Growth Rate Data

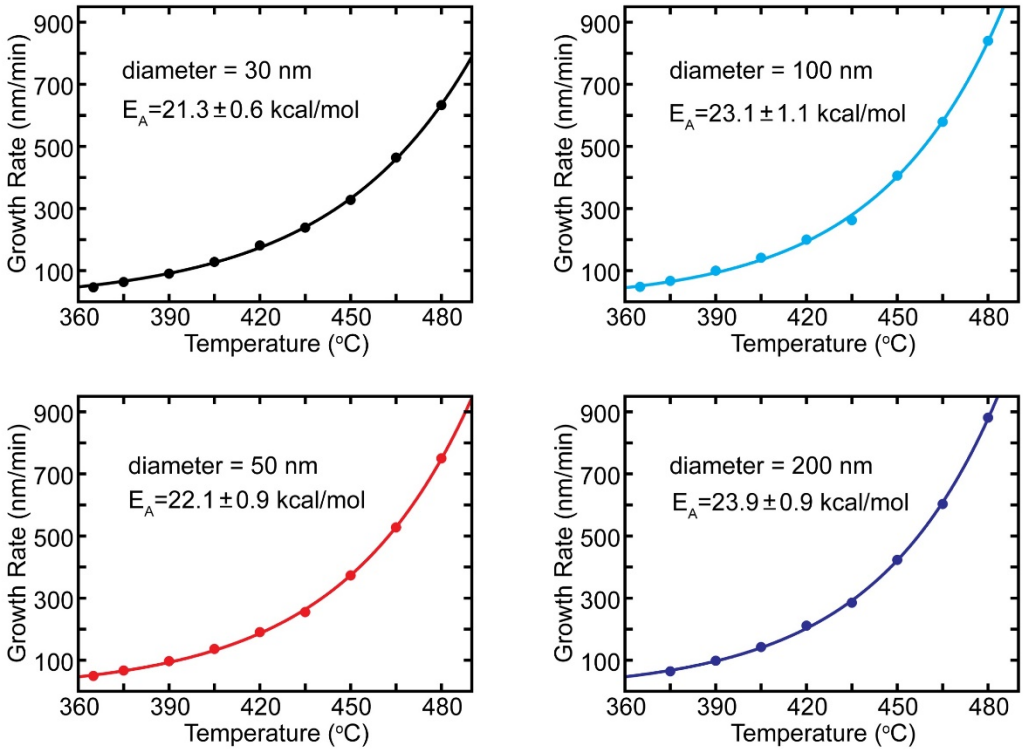

Figure 3.9: Growth rate vs. temperature for a variety of NW diameters

Solid lines are fits to the Arrhenius equation; diameter and activation energy are denoted in the plots. Error bars are the same size as the plot markers and were omitted for clarity. All data were collected at a silane partial pressure of 0.4 Torr.

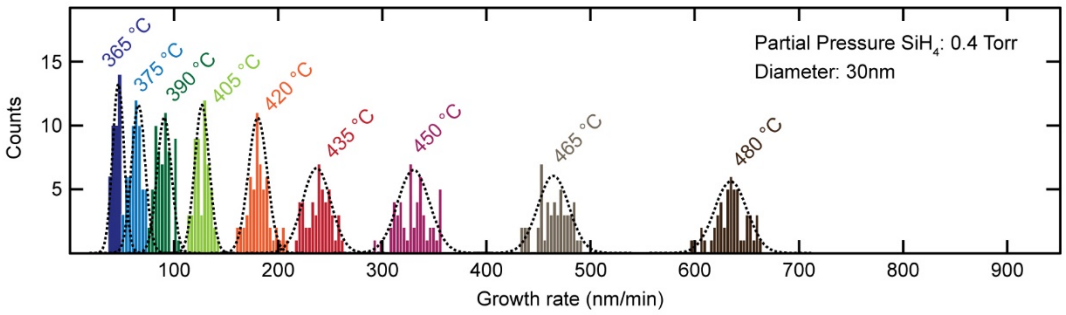
365 °C
375 °C
390 °C
405 °C
420 °C
435 °C
450 °C
465 °C
480 °C
Partial Pressure SiH_4: 0.4 Torr
Diameter: 30nm
Counts
Growth rate (nm/min)

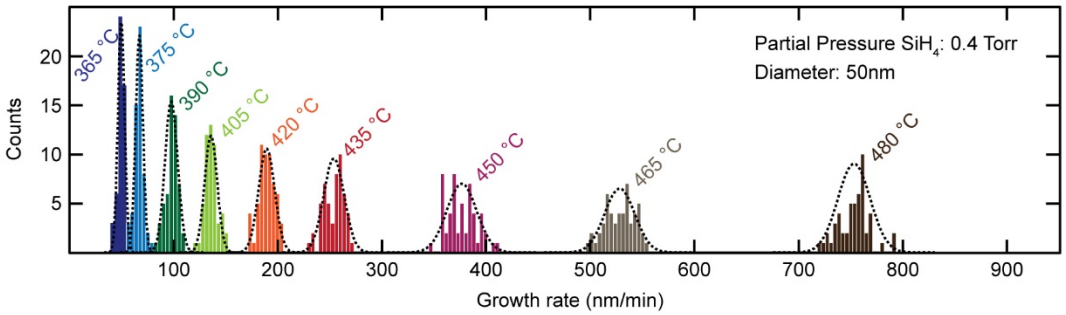
365 °C
375 °C
390 °C
405 °C
420 °C
435 °C
450 °C
465 °C
480 °C
Partial Pressure SiH_4: 0.4 Torr
Diameter: 50nm
Counts
Growth rate (nm/min)

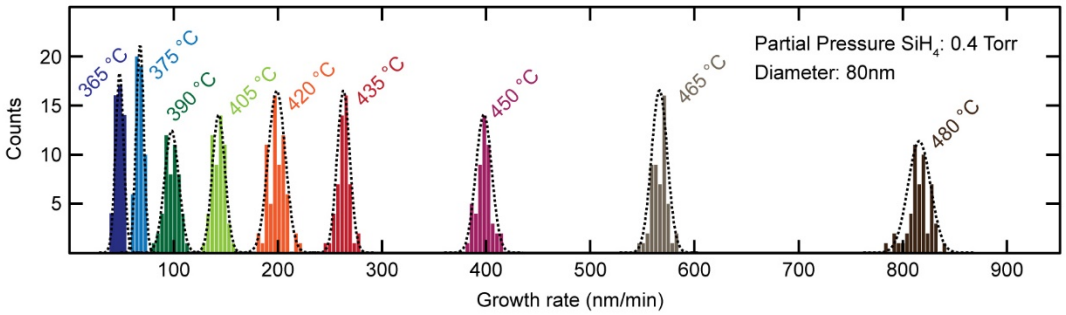
365 °C
375 °C
390 °C
405 °C
420 °C
435 °C
450 °C
465 °C
480 °C
Partial Pressure SiH_4: 0.4 Torr
Diameter: 80nm
Counts
Growth rate (nm/min)

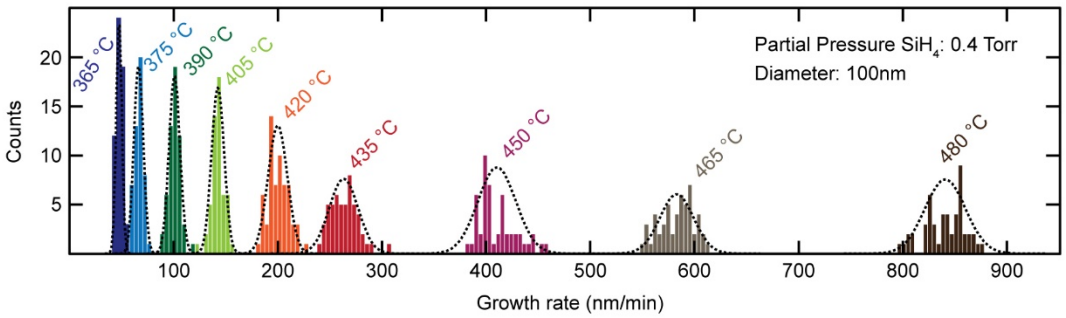
365 °C
375 °C
390 °C
405 °C
420 °C
435 °C
450 °C
465 °C
480 °C
Partial Pressure SiH_4: 0.4 Torr
Diameter: 100nm
Counts
Growth rate (nm/min)

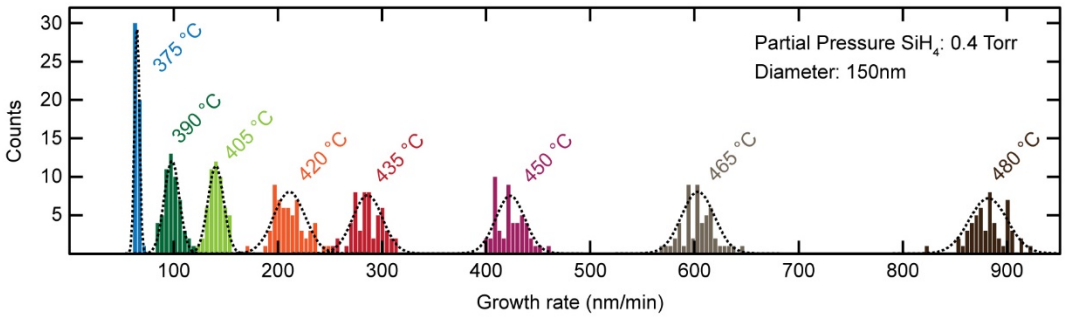
375 °C
390 °C
405 °C
420 °C
435 °C
450 °C
465 °C
480 °C
Partial Pressure SiH_4: 0.4 Torr
Diameter: 150nm
Counts
Growth rate (nm/min)

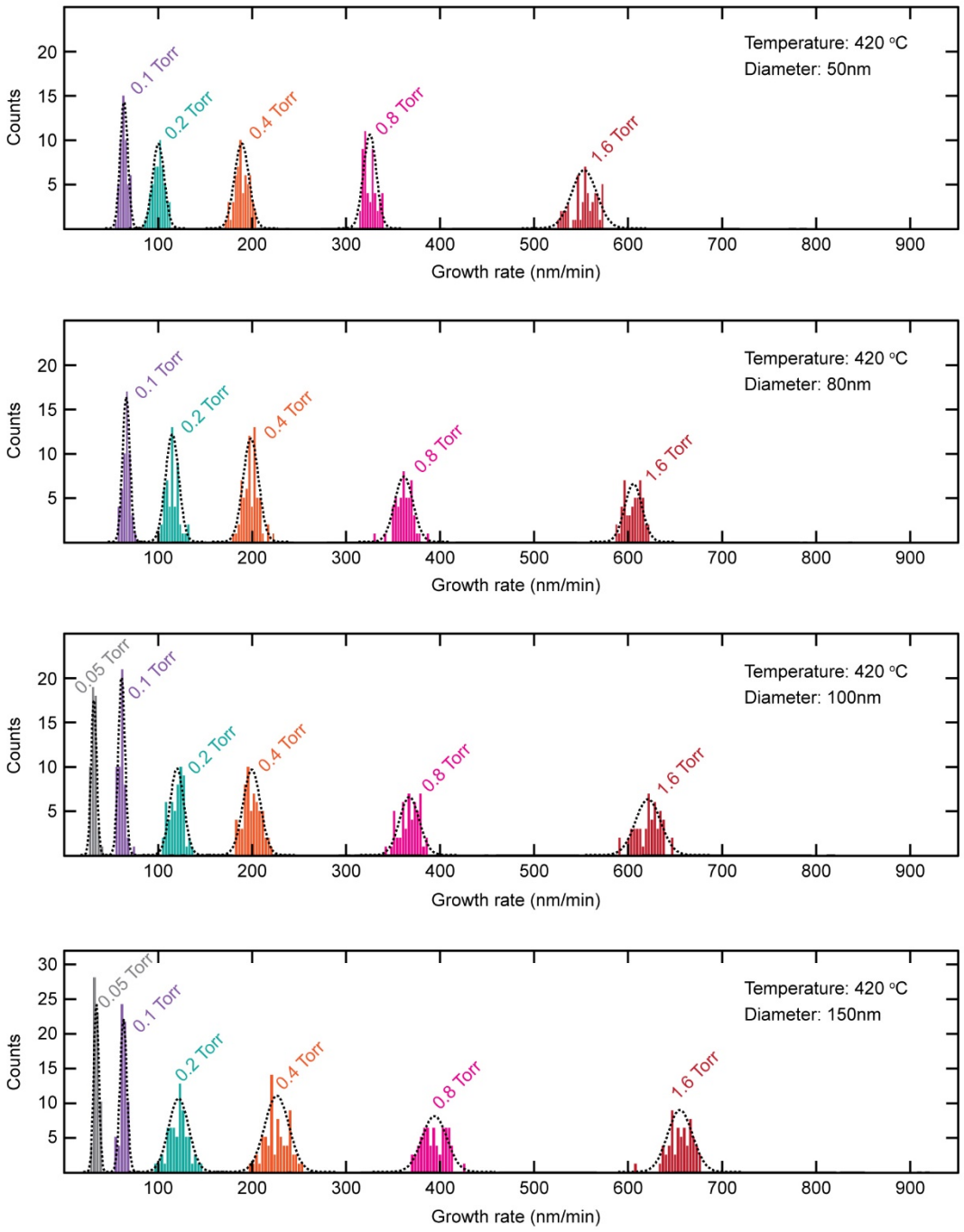

Figure 3.10: Histograms of growth rate data for various synthetic conditions

Temperature, SiH_4 partial pressure and diameter are indicated in each figure for each set of data. The dashed black lines are Gaussian fits to the data.

Table 3.1: Nanowire Growth Rate for each Diameter, Temperature, and Partial Pressure

Temperature (^{o}C)	Partial Pressure (Torr)	Diameter (nm)	Growth Rate (nm/min)
365	0.4	30	46 ± 6
375	0.4	30	66 ± 7
390	0.4	30	90 ± 7
405	0.4	30	127 ± 7
420	0.4	30	180 ± 9
435	0.4	30	237 ± 14
450	0.4	30	330 ± 15
465	0.4	30	464 ± 15
480	0.4	30	635 ± 16

365	0.4	50	50 ± 3
375	0.4	50	67 ± 4
390	0.4	50	98 ± 6
405	0.4	50	136 ± 6
420	0.4	50	189 ± 8
435	0.4	50	254 ± 10
450	0.4	50	376 ± 14
465	0.4	50	528 ± 14
480	0.4	50	753 ± 16

365	0.4	80	48 ± 4

375	0.4	80	68 ± 4
390	0.4	80	98 ± 7
405	0.4	80	143 ± 6
420	0.4	80	199 ± 8
435	0.4	80	263 ± 6
450	0.4	80	397 ± 8
465	0.4	80	566 ± 8
480	0.4	80	815 ± 11

365	0.4	100	48 ± 3
375	0.4	100	66 ± 4
390	0.4	100	101 ± 5
405	0.4	100	142 ± 6
420	0.4	100	200 ± 9
435	0.4	100	263 ± 14
450	0.4	100	410 ± 18
465	0.4	100	583 ± 16
480	0.4	100	840 ± 19

375	0.4	200	65 ± 2
390	0.4	200	98 ± 7
405	0.4	200	140 ± 8
420	0.4	200	211 ± 15

435	0.4	200	286 ± 14
450	0.4	200	423 ± 14
465	0.4	200	603 ± 16
480	0.4	200	881 ± 18
Temperature (^{o}C)	Partial Pressure (Torr)	Diameter (nm)	Growth Rate (nm/min)
420	0.1	50	64 ± 4
420	0.2	50	100 ± 6
420	0.4	50	189 ± 8
420	0.8	50	326 ± 7
420	1.6	50	554 ± 13

420	0.1	80	66 ± 4
420	0.2	80	115 ± 7
420	0.4	80	199 ± 8
420	0.8	80	362 ± 10
420	1.6	80	607 ± 9

420	0.05	100	31 ± 3
420	0.1	100	61 ± 4
420	0.2	100	120 ± 7
420	0.4	100	200 ± 9
420	0.8	100	368 ± 11
420	1.6	100	622 ± 13

420	0.05	150	34 ± 3
420	0.1	150	63 ± 4
420	0.2	150	122 ± 11
420	0.4	150	226 ± 13
420	0.8	150	395 ± 13
420	1.6	150	656 ± 13

390	0.4	50	98 ± 6
390	0.8	50	172 ± 8
390	1.6	50	268 ± 18

390	0.4	80	98 ± 7
390	0.8	80	173 ± 10
390	1.6	80	265 ± 16

390	0.4	100	101 ± 5
390	0.8	100	178 ± 9
390	1.6	100	271 ± 19

REFERENCES

1. Lieber, C. M., Semiconductor Nanowires: A Platform for Nanoscience and Nanotechnology. *MRS Bull.* **2011,** *36*, 1052-1063.

2. Yang, P.; Yan, R.; Fardy, M., Semiconductor Nanowire: What's Next? *Nano Lett.* **2010,** *10* (5), 1529-36.

3. Law, M.; Sirbuly, D. J.; Johnson, J. C.; Goldberger, J.; Saykally, R. J.; Yang, P., Nanoribbon Waveguides for Subwavelength Photonics Integration. *Science.* **2004,** *305* (5688), 1269-73.

4. Qian, F.; Li, Y.; Gradečak, S.; Wang, D.; Barrelet, C. J.; Lieber, C. M., Gallium Nitride-Based Nanowire Radial Heterostructures for Nanophotonics. *Nano Lett.* **2004,** *4* (10), 1975-1979.

5. Zhang, X.; Pinion, C. W.; Christesen, J. D.; Flynn, C. J.; Celano, T. A.; Cahoon, J. F., Horizontal Silicon Nanowires with Radial p–n Junctions: A Platform for Unconventional Solar Cells. *J. Phys. Chem. Lett.* **2013,** *4* (12), 2002-2009.

6. Tian, B.; Kempa, T. J.; Lieber, C. M., Single Nanowire Photovoltaics. *Chem. Soc. Rev.* **2009,** *38* (1), 16-24.

7. Kempa, T. J.; Day, R. W.; Kim, S.-K.; Park, H.-G.; Lieber, C. M., Semiconductor Nanowires: A Platform for Exploring Limits and Concepts for Nano-Enabled Solar Cells. *Energy Environ. Sci.* **2013,** *6* (3), 719-733.

8. Hochbaum, A. I.; Yang, P., Semiconductor Nanowires for Energy Conversion. *Chem. Rev.* **2010,** *110* (1), 527-46.

9. Lee, S. H.; Jung, Y.; Agarwal, R., Highly Scalable Non-Volatile and Ultra-Low-Power Phase-Change Nanowire Memory. *Nat. Nanotechnol.* **2007,** *2* (10), 626-30.

10. Yao, J.; Yan, H.; Das, S.; Klemic, J. F.; Ellenbogen, J. C.; Lieber, C. M., Nanowire Nanocomputer as a Finite-State Machine. *Proc. Natl. Acad. Sci. U.S.A.* **2014,** *111* (7), 2431-5.

11. Christesen, J. D.; Pinion, C. W.; Grumstrup, E. M.; Papanikolas, J. M.; Cahoon, J. F., Synthetically Encoding 10 nm Morphology in Silicon Nanowires. *Nano Lett.* **2013,** *13* (12), 6281-6.

12. Wagner, R. S.; Ellis, W. C., Vapor-Liquid-Solid Mechanism of Single Crystal Growth. *Appl. Phys. Lett.* **1964,** *4* (5), 89-90.

13. Wagner, R. S.; Ellis, W. C., Vapor-Liquid-Solid Mechanism of Crystal Growth and Its Application to Silicon. *T. Metall. Soc. Aime* **1965,** *233* (6), 1053-1064.

14. Wagner, R. S.; Ellis, W. C.; Jackson, K. A.; Arnold, S. M., Study of the Filamentary Growth of Silicon Crystals from the Vapor. *J. Appl. Phys.* **1964,** *35* (10), 2993-3000.

15. Bootsma, G. A.; Gassen, H. J., A Quantitative Study on the Growth of Silicon Whiskers from Silane and Germanium Whiskers from Germane. *J. Cryst. Growth* **1971,** *10* (3), 223-234.

16. Gudiksen, M. S.; Lauhon, L. J.; Wang, J.; Smith, D. C.; Lieber, C. M., Growth of Nanowire Superlattice Structures for Nanoscale Photonics and Electronics. *Nature.* **2002,** *415* (6872), 617-20.

17. Huang, Y.; Duan, X.; Cui, Y.; Lieber, C. M., Gallium Nitride Nanowire Nanodevices. *Nano Lett.* **2002,** *2* (2), 101-104.

18. Duan, X.; Huang, Y.; Cui, Y.; Wang, J.; Lieber, C. M., Indium Phosphide Nanowires as Building Blocks for Nanoscale Electronic and Optoelectronic Devices. *Nature.* **2001,** *409* (6816), 66-9.

19. Wittemann, J. V.; Münchgesang, W.; Senz, S.; Schmidt, V., Silver Catalyzed Ultrathin Silicon Nanowires Grown by Low-Temperature Chemical-Vapor-Deposition. *J. Appl. Phys.* **2010,** *107* (9), 096105.

20. Givargizov, E. I., Fundamental Aspects of VLS growth. *J. Cryst. Growth* **1975,** *31* (Dec), 20-30.

21. Weyher, J., Some Notes on the Growth Kinetics and Morphology of VLS Silicon Crystals Grown with Platinum and Gold as Liquid-Forming Agents. *J. Cryst. Growth* **1978,** *43* (2), 235-244.

22. Cui, Y.; Lauhon, L. J.; Gudiksen, M. S.; Wang, J. F.; Lieber, C. M., Diameter-Controlled Synthesis of Single-Crystal Silicon Nanowires. *Appl. Phys. Lett.* **2001,** *78* (15), 2214-2216.

23. Wu, Y.; Cui, Y.; Huynh, L.; Barrelet, C. J.; Bell, D. C.; Lieber, C. M., Controlled Growth and Structures of Molecular-Scale Silicon Nanowires. *Nano Lett.* **2004,** *4* (3), 433-436.

24. Yang, C.; Zhong, Z. H.; Lieber, C. M., Encoding Electronic Properties by Synthesis of Axial Modulation-Doped Silicon Nanowires. *Science.* **2005,** *310* (5752), 1304-1307.

25. Bjork, M. T.; Ohlsson, B. J.; Sass, T.; Persson, A. I.; Thelander, C.; Magnusson, M. H.; Deppert, K.; Wallenberg, L. R.; Samuelson, L., One-Dimensional Steeplechase for Electrons Realized. *Nano Lett.* **2002,** *2* (2), 87-89.

26. Tian, B.; Xie, P.; Kempa, T. J.; Bell, D. C.; Lieber, C. M., Single-Crystalline Kinked Semiconductor Nanowire Superstructures. *Nat. Nanotechnol.* **2009,** *4* (12), 824-9.

27. Crawford, S.; Lim, S. K.; Gradecak, S., Fundamental Insights into Nanowire Diameter Modulation and the Liquid/Solid Interface. *Nano Lett.* **2013,** *13* (1), 226-232.

28. Lim, S. K.; Crawford, S.; Haberfehlner, G.; Gradecak, S., Controlled Modulation of Diameter and Composition along Individual III-V Nitride Nanowires. *Nano Lett.* **2013,** *13* (2), 331-336.

29. Kodambaka, S.; Tersoff, J.; Reuter, M. C.; Ross, F. M., Germanium Nanowire Growth Below the Eutectic Temperature. *Science.* **2007,** *316* (5825), 729-32.

30. Lew, K.-K.; Redwing, J. M., Growth Characteristics of Silicon Nanowires Synthesized by Vapor–Liquid–Solid Growth in Nanoporous Alumina Templates. *J. Cryst. Growth* **2003,** *254* (1-2), 14-22.

31. Kodambaka, S.; Tersoff, J.; Reuter, M. C.; Ross, F. M., Diameter-Independent Kinetics in the Vapor-Liquid-Solid Growth of Si Nanowires. *Phys. Rev. Lett.* **2006,** *96* (9), 096105.

32. Dubrovskii, V. G.; Sibirev, N. V., General Form of the Dependences of Nanowire Growth Rate on the Nanowire Radius. *J. Cryst. Growth* **2007,** *304* (2), 504-513.

33. Shakthivel, D.; Raghavan, S., Vapor-Liquid-Solid Growth of Si Nanowires: A Kinetic Analysis. *J. Appl. Phys.* **2012,** *112* (2), 024317.

34. Kikkawa, J.; Ohno, Y.; Takeda, S., Growth Rate of Silicon Nanowires. *Appl. Phys. Lett.* **2005,** *86* (12), 123109.

35. Schmidt, V.; Senz, S.; Gösele, U., Diameter Dependence of the Growth Velocity of Silicon Nanowires Synthesized via the Vapor-Liquid-Solid Mechanism. *Phys. Rev. B* **2007,** *75* (4), 045335.

36. Dubrovskii, V.; Sibirev, N.; Cirlin, G.; Soshnikov, I.; Chen, W. H.; Larde, R.; Cadel, E.; Pareige, P.; Xu, T.; Grandidier, B.; Nys, J. P.; Stievenard, D.; Moewe, M.; Chuang, L.; Chang-Hasnain, C., Gibbs-Thomson and Diffusion-Induced Contributions to the Growth rate of Si, InP, and GaAs Nanowires. *Phys. Rev. B* **2009,** *79* (20), 205316.

37. Dubrovskii, V. G.; Sibirev, N. V.; Cirlin, G. E., Kinetic Model of the Growth of Nanodimensional Whiskers by the Vapor-Liquid-Crystal Mechanism. *Tech. Phys. Lett.* **2004,** *30* (8), 682-686.

38. Dubrovskii, V. G., Refinement of the Wagner-Ellis Formula for the Minimum Radius and the Givargizov-Chernov Formula for the Growth Rate of Nanowire. *Tech. Phys. Lett.* **2013,** *39* (2), 157-160.

39. Allen, J. E.; Hemesath, E. R.; Perea, D. E.; Lensch-Falk, J. L.; Li, Z. Y.; Yin, F.; Gass, M. H.; Wang, P.; Bleloch, A. L.; Palmer, R. E.; Lauhon, L. J., High-Resolution Detection of Au catalyst atoms in Si nanowires. *Nat. Nanotechnol.* **2008,** *3* (3), 168-73.

40. Bjork, M. T.; Schmid, H.; Knoch, J.; Riel, H.; Riess, W., Donor Deactivation in Silicon Nanostructures. *Nat. Nanotechnol.* **2009,** *4* (2), 103-7.

41. Cohen-Karni, T.; Casanova, D.; Cahoon, J. F.; Qing, Q.; Bell, D. C.; Lieber, C. M., Synthetically Encoded Ultrashort-Channel Nanowire Transistors for Fast, Pointlike Cellular Signal Detection. *Nano Lett.* **2012,** *12* (5), 2639-44.

42. Schmid, H.; Björk, M. T.; Knoch, J.; Riel, H.; Riess, W.; Rice, P.; Topuria, T., Patterned Epitaxial Vapor-Liquid-Solid Growth of Silicon Nanowires on Si(111) Using Silane. *J. Appl. Phys.* **2008,** *103* (2), 024304.

43. Schmidt, V.; Wittemann, J. V.; Gosele, U., Growth, Thermodynamics, and Electrical Properties of Silicon Nanowires. *Chem. Rev.* **2010,** *110* (1), 361-88.

44. Haruta, M., When Gold is not Noble: Catalysis by Nanoparticles. *Chem. Rec.* **2003,** *3* (2), 75-87.

45. Tsunoyama, H.; Sakurai, H.; Negishi, Y.; Tsukuda, T., Size-Specific Catalytic Activity of Polymer-Stabilized Gold Nanoclusters for Aerobic Alcohol Oxidation in Water. *J. Am. Chem. Soc.* **2005,** *127* (26), 9374-5.

46. Wang, H.; Zepeda-Ruiz, L. A.; Gilmer, G. H.; Upmanyu, M., Atomistics of Vapour-Liquid-Solid Nanowire Growth. *Nat. Commun.* **2013,** *4*, 1956.

47. Millot, F.; Sarou-Kanian, V.; Rifflet, J. C.; Vinet, B., The Surface Tension of Liquid Silicon at High Temperature. *Mater. Sci. Eng., A* **2008,** *495* (1-2), 8-13.

48. Lide, D. R., *CRC Handbook of Chemistry and Physics*. 72nd ed.; CRC Press: Boca Racon, **1991**.

49. Roper, S. M.; Anderson, A. M.; Davis, S. H.; Voorhees, P. W., Radius Selection and Droplet Unpinning in Vapor-Liquid-Solid-Grown Nanowires. *J. Appl. Phys.* **2010,** *107* (11), 114320.

50. Shpyrko, O. G.; Streitel, R.; Balagurusamy, V. S.; Grigoriev, A. Y.; Deutsch, M.; Ocko, B. M.; Meron, M.; Lin, B.; Pershan, P. S., Surface Crystallization in a Liquid AuSi Alloy. *Science.* **2006,** *313* (5783), 77-80.

CHAPTER 4: INSTANTANEOUS SWITCHING BETWEEN A LIQUID AND SUPERHEATED SOLID CATALYST DURING NANOWIRE GROWTH[1]

4.1 Introduction

Enabling atomic-scale control of composition, size, morphology, and crystal phase is a primary goal in the bottom-up synthesis of semiconductor nanomaterials. Materials with nanometer dimensions, however, often exhibit unexpected phase behavior that cannot necessarily be predicted from bulk properties and equilibrium phase diagrams. In nanocrystals, for instance, the nanoscale Kirkendall effect induces the formation of hollow nanoparticles [1], and periodic phase domains form during partial cation exchange reactions [2]. For NWs, GaAs NWs exhibit a wurtzite crystal structure that is thermodynamically unstable [3] while InGaN NWs can support high In compositions that would phase separate in a bulk material [4]. In each of these cases, the unique phase behavior has led to new technological applications of the materials.

Semiconductor NWs have been widely developed as a bottom-up technological platform for nanoscale electronic [5-6], photonic [7-8], and alternative energy [9-11] devices. A common approach to NW synthesis is VLS growth [12], in which a liquid eutectic alloy of semiconductor and metal catalyzes the growth of a one-dimensional NW above the eutectic temperature (T_{eu}) of the alloy (see the binary eutectic AuSi phase diagram in Fig. 4.1A). The VLS growth process is known to exhibit surprising phase behavior. For example, nucleation and growth of Au-catalyzed Ge NWs is possible well below the bulk T_{eu} [13-15]. In addition, the liquid can host solid metal silicide

[1] This chapter previously appeared as an article in the Journal of Physical Chemistry Letters. The original citation is as follows: Pinion, C. W.; Hill, D. J.; Christesen, J. D.; McBride, J. R.; Cahoon, J. F., Barrierless Switching between a Liquid and Superheated Solid Catalyst during Nanowire Growth. J Phys Chem Lett 2016, 7 (20), 4236-4242

nanoparticles that are incorporated into the NW crystal structure.[16] In addition to VLS growth, vapor-solid-solid (VSS) NW growth has been demonstrated using solid metal catalysts below T_{eu}. VSS growth has the advantage of producing near atomically abrupt junctions but the disadvantage of exceedingly slow growth rates two orders of magnitude lower than VLS growth. [17-18] This problem has led to efforts to identify alternate metal catalysts with higher eutectic temperatures that can facilitate faster VSS growth. [19]

Here, we show that VSS growth of Si NWs with Au catalysts can be performed above T_{eu} and that the phase of the catalyst can be reversibly switched (Fig. 4.1B) between a liquid and superheated solid under isothermal conditions up to 25-30 °C above T_{eu}. This unexpected switching effect is enabled by control of the NW surface chemistry and surface-mediated reactions, which change the dynamics of nanoparticle liquefaction and solidification to near-barrierless processes under the appropriate synthetic conditions. The switching effect directly couples conventional VLS growth with VSS growth under isothermal conditions, enabling the facile synthesis of atomic-scale transitions that cannot be achieved by traditional VLS processes. [19-20] We also find that the surface chemistry enables sub-eutectic growth of Si NWs at temperatures ~25 °C below T_{eu}, analogous to the phenomenon observed in Ge NWs.[13-15]

4.2 Experimental

NWs were grown in a hot-walled chemical vapor deposition system at 390 °C and 40 Torr total pressure in an atmosphere of H_2 unless noted otherwise.[21-22] The scanning electron microscopy (SEM) image in Fig. 4.1C shows a NW with multiple transitions between a liquid and solid catalyst. P dopant modulation and NW etching produces the diameter modulated regions in Fig. 4.1C that are used to determine the NW growth rate, as described previously. [21-22] A two orders of magnitude change in growth rate is observed, indicative of switching between a VLS and

VSS mechanism.[19, 23] Long sections with high growth rates correspond to a liquid catalyst and short sections with low growth rates to a solid catalyst, as will be proven below.

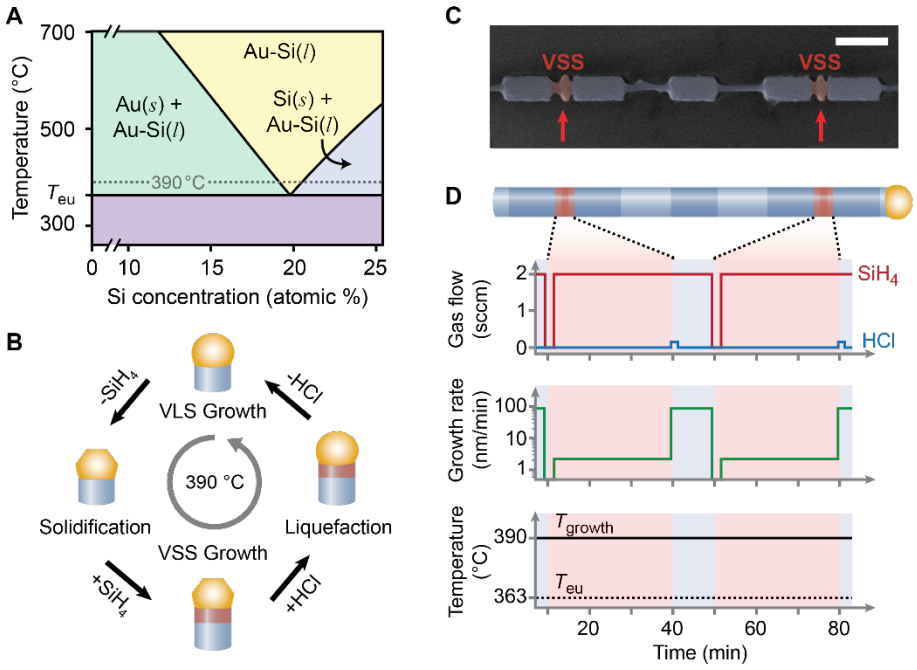

Figure 4.1: Reversible switching of catalyst phase under isothermal conditions above T_{eu}

(A) AuSi binary phase diagram showing the eutectic isotherm, T_{eu}, and the reactor temperature at which switching was observed, 390 °C. (B) Schematic illustration of the reversible switching process. Nanowire segments shaded blue and red correspond to regions grown with VLS and VSS mechanisms, respectively. (C) False-colored SEM image of a modulation-doped and etched Si NW, showing two VSS sections, shaded red and marked by arrows, grown with a solid catalyst; scale bar, 200 nm. (D) Upper: schematic diagram of the NW in panel C. The darker blue and darker red shading correspond to heavily P-doped regions, which resist etching during post-growth processing. Lower: plots of reaction conditions versus time, showing gas flow rates (top) for SiH_4 (red trace) and HCl (blue trace), NW growth rate (middle), and reaction temperature (bottom).

As illustrated in Fig. 4.1B, the switching process begins with a liquid catalyst in VLS growth and involves four cyclic steps all performed isothermally: catalyst solidification by removal of SiH_4 for 30 seconds, VSS growth by reintroduction of SiH_4, catalyst liquefaction by introduction of HCl for 30 seconds, and return to standard VLS growth by removal of HCl. The solidification and liquefaction processes are fully reversible, as illustrated by the two VSS segments in Fig. 4.1C surrounded by VLS segments. Several steps in this switching process are surprising. First, the solidification occurs ~30 °C above T_{eu} at a temperature for which a liquid rather than solid catalyst should be the thermodynamically stable phase. Second, VSS growth above T_{eu} is unexpected because the catalyst is substantially superheated and not expected to remain in the solid state. Third, the liquefaction of the catalyst upon the introduction of HCl has no obvious precedent in the literature. Below, we prove that the catalyst has transitioned between liquid and solid states and explain the kinetic and thermodynamic origins of each step in the switching process.

To confirm that the catalyst has solidified and that NW growth transitions from a VLS to VSS mechanism in the fast and slow growth regimes, respectively, we examined the diameter dependence, activation energy, and dopant transition width during the growth process, as shown in Fig. 4.2. Diameter-dependent growth kinetics (Fig. 4.2A) from the two regimes show opposite trends with NW diameter. The fast growth regime exhibits a diameter-independent growth rate, which is expected for incorporation-limited VLS growth.[22] In contrast, the kinetics from the slow growth regime are inversely proportional to diameter, which is consistent with the VSS growth mechanism.[24]

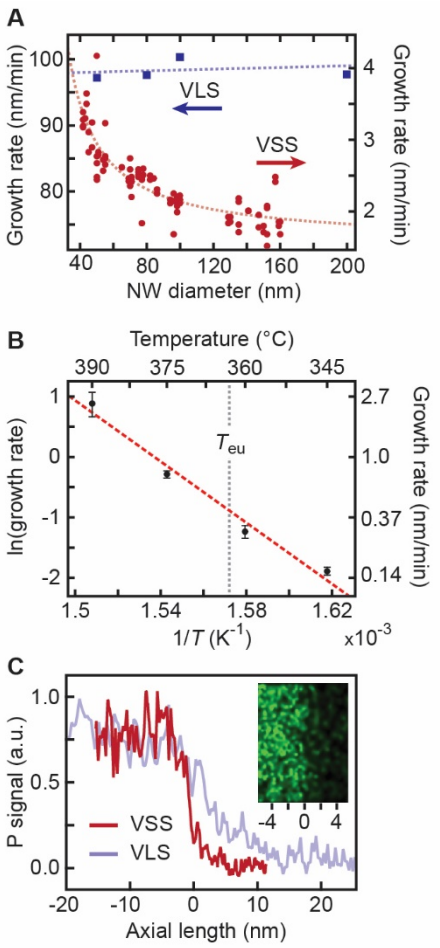

Figure 4.2: Evidence of a solid catalyst and VSS mechanism above T_{eu}

(**A**) NW growth rate as a function of diameter from the slow (red circles) and fast (blue squares) regimes at 390 °C, showing opposite trends with NW diameter, indicative of VSS and VLS growth, respectively. Dashed lines are best fits of the data. (**B**) Arrhenius plot of VSS growth rates at temperatures above and below T_{eu}. Red dashed line is a linear best fit of the data to the Arrhenius expression. (**C**) P EDS signal across an n-type/intrinsic transition as a function of position along the NW axis for VSS (red trace) and VLS (blue trace) growth. Inset: high-resolution EDS map of P (green) across the VSS dopant transition; each tick mark corresponds to 2 nm.

We measured VSS growth kinetics by cooling the system below T_{eu}, which is the conventional method to solidify a NW catalyst and induce VSS growth.[19, 23] Fig. 4.2B displays an Arrhenius plot of the VSS growth kinetics both below T_{eu} and in the slow regime measured above T_{eu}. As apparent from the dashed line in Fig. 4.2B, both data sets are well fit to a single line over the entire temperature range, yielding an activation energy of 209 ± 54 kJ/mol. The linearity of the data indicates that both growth processes occur by the same mechanism. Moreover, the activation energy is more than two fold larger than the value measured for VLS growth,[22] consistent with a VSS mechanism in which the rate-limiting step is injection of Si species across the circumferential boundary between the catalyst and NW.[19, 24]

As shown by the P elemental line scans in Fig. 4.1C for n-type to intrinsic dopant transitions, an interface ~5 nm in width is encoded by VLS growth[20] whereas an ~2 nm interface is encoded in the slow growth regime. The inset of Fig. 4.2C depicts a high-resolution elemental map of the P dopants across the ~2 nm transition, the abruptness of which is a hallmark of the VSS mechanism.[17] The measurement of the transition width is approaching the instrument resolution limit under these conditions,[25] which suggests that the dopant transition may be atomically sharp. Taken together, the data in Fig. 4.2 conclusively indicate that the NW reversibly transitions between liquid and solid, and between VLS and VSS mechanisms, by the steps illustrated in Fig. 4.1B.

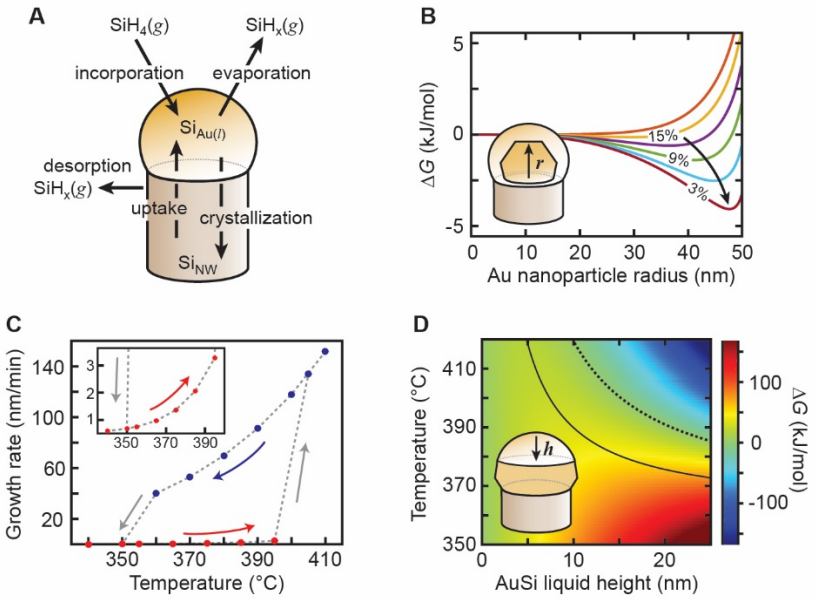

Figure 4.3: Mechanism of catalyst solidification and liquefaction

(A) Schematic illustration of the microscopic processes that govern the kinetics of NW growth, solidification, and liquefaction. (B) Plot of ΔG during catalyst solidification as a function of the solid Au particle radius at various Si concentrations. Concentrations range from 18 (top orange trace) to 3 (bottom red trace) atomic % Si in steps of 3%, and the model assumes a 100 nm catalyst diameter. Inset: schematic illustration of the solid Au nanoparticle with radius, r, that nucleates and grows during the solidification process. (C) NW growth rate as a function of temperature, showing hysteresis as the sample is heated or cooled. Blue, red, and gray arrows correspond to cooling, heating, and phase transitions, respectively. Blue and red marker symbols correspond to VLS and VSS growth, respectively. Inset: magnified plot of the VSS growth kinetics. (D) Heatmap of ΔG during catalyst liquefaction as a function of temperature and the Au-Si liquid height, h. Solid black contour corresponds to the nucleation barrier, ΔG^*, at each temperature, and black dashed contour corresponds to $\Delta G = 0$. Inset: schematic illustration of the liquid catalyst formed during liquefaction, which nucleates and grows as a liquid Au-Si cap on the solid Au particle.

4.3 Analysis, Thermodynamic Modeling, and Discussion

To understand why the catalyst can be reversibly switched between these states, we consider NW growth in the framework of the five microscopic processes—incorporation, evaporation, desorption, crystallization, and uptake—depicted in Fig. 4.3A.[22, 26] The solidification process consists of a subset of these reactions: evaporation, desorption, and uptake. Incorporation is disregarded because of the absence of SiH_4 and crystallization is suppressed because the catalyst is not supersaturated. Evaporation and desorption reactions serve to decrease the concentration of Si in the liquid catalyst. The uptake reaction, which corresponds to the dissolution of Si atoms from the crystalline NW into the catalyst, increases the concentration of Si in the liquid catalyst and has been observed during solid-liquid-vapor (SLV) etching of NWs [26].

Solidification of the catalyst can potentially be explained if the sum of the rates of the evaporation and desorption exceed the rate of uptake, causing the liquid catalyst to decrease in Si concentration until solidification occurs. To understand this effect, we developed a model in which a hemispherical solid Au nanoparticle nucleates and grows inside the liquid, as illustrated in Fig. 3B (see sections 4.5.3 and 4.5.4 for a full description). The change in Gibbs free energy, ΔG, can be expressed as:

$$\Delta G = m\,\Delta G_f\left(T,\, n_{Au}^{L},\, n_{Si}^{L}\right) + \Delta G_{surface}\,, \qquad \text{(eq. 4.1)}$$

where ΔG_f is the difference in Gibbs free energy of formation including ideal and excess mixing terms[21, 27] for a given state, n_{Au}^{L} is the moles of liquid Au, n_{Si}^{L} is the moles of liquid Si, T is the reactor temperature, $\Delta G_{\text{surface}}$ is the contribution to ΔG from surface energies, and m is either −1 or 1, corresponding to solidification or liquefaction, respectively. For Si concentrations below the liquidus line, for which $|\Delta G_f| >> |\Delta G_{\text{surface}}|$, the surface term can be neglected for the solidification process. Assuming concentric hemispheres, ΔG was plotted as a function of the Au nanoparticle

radius for different Si concentrations, as shown in Fig. 4.3B. When the percentage Si approaches ~12%, which is ~8% below the equilibrium concentration at 390 °C, it is thermodynamically favorable and near-barrierless to nucleate an Au nanoparticle that grows to a diameter of ~80 nm. As the Si content continues to decrease through evaporation and desorption, the size of the thermodynamically stable solid increases, eventually leaving only solid Au.

This model explains the solidification of the NW catalyst above T_{eu} but is predicated on the kinetics of Si uptake into the liquid being slow relative to evaporation and desorption. The kinetics of uptake can be evaluated by the rate of SLV etching, which has previously only been observed in Si at temperatures greater than 400 °C under a chlorine atmosphere.[28] In a series of control experiments in a hydrogen atmosphere, we observed no evidence for SLV etching at temperatures up to 390 °C (Fig. 4.4), indicating that the kinetics for uptake are slow and possess a high activation barrier. This effect is compounded by the geometry of the NW catalyst, for which the liquid-vapor surface area is 2-4 times higher than the liquid-solid surface area. Thus, the faster kinetics of evaporation and desorption, which deplete the catalyst of Si, explain the solidification of the catalyst upon removal of SiH_4.

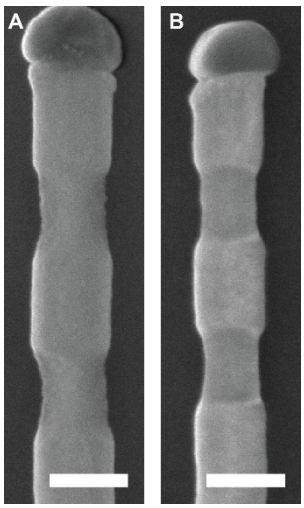

Figure 4.4: Absence of SLV etching under hydrogen atmosphere

SEM images of a modulation-doped and etched Si NWs (**A**) without SLV etching and (**B**) with one hour of SLV etching (*i.e.* no SiH_4 in the reactor) at 390 °C; scale bars, 100 nm. The similarity of each image indicates the uptake process (*cf.* Fig. 4.3A) is inhibited at these synthetic conditions.

After solidification and following reintroduction of SiH_4, the NW continues growing in a VSS growth mechanism with a superheated solid catalyst (*cf.* Fig. 4.1B) rather than returning to a VLS mechanism. Superheating and supercooling of solid and liquid phases are known to occur in nanocrystalline systems.[19, 29-30] To probe this effect, we examined the temperature-dependent hysteresis of the growth rate, as shown in Fig. 4.3C, by cycling the temperature from 410 to 345 and back to 410 °C with continuous flow of SiH_4. The liquid catalyst solidified at ~355 ºC, transitioning to a VSS growth mechanism. The catalyst continued to remain in the solid state until reheated to ~405 °C, at which point it liquefied and returned to a VLS growth mechanism. This data demonstrates a hysteresis window of ~50 °C in which the catalyst may exist in either the solid or liquid state depending on the reaction history. We observe minimal supercooling of the liquid catalyst below T_{eu} and ~40 °C of superheating above T_{eu}. This behavior is in sharp contrast to most

systems, both nanoscale and bulk, which typically exhibit significant super-cooling and minimal super-heating.[30]

To understand the observed superheating and supercooling, we developed a model of catalyst liquefaction that builds on the liquid nucleation and growth model in nanocrystalline systems.[31] As illustrated in the inset of Fig. 4.3D, our model considers the nucleation of the liquid phase by formation of a small liquid cap at the tip of the solid catalyst, which then propagates downward to liquefy the entire catalyst particle. The free energy difference, ΔG, between the solid catalyst and a catalyst with a liquid cap is given by eq. 1 with $m = -1$. For liquefaction, the $\Delta G_{\text{surface}}$ term may not be neglected and, assuming a hemispherical catalyst, can be expressed as:

$$\Delta G_{\text{surface}}(R, h) = \pi h(2R - h)\gamma_{\text{sl}} + 2\pi R(R - h)\gamma_{\text{sv}} + 2\pi Rh\gamma_{\text{lv}}\,, \qquad \text{(eq. 4.2)}$$

where R is radius of the catalyst, h is the height of the liquid cap, γ_{sl} is the Au-solid to liquid-AuSi surface energy, γ_{lv} is the liquid-AuSi to vapor surface energy, and γ_{sv} is the Au-solid to vapor surface energy.[22] The solid-Si to solid-Au and solid-Si to liquid-AuSi surface energies are assumed to be equal. The tip of the catalyst was chosen as the nucleation site for simplicity, but alternate geometries would give qualitatively similar results.

Fig. 4.3D depicts the value of ΔG for a range of T and h using literature values for the physical constants.[25] Even for temperatures well above T_{eu}, the transition from a solid to a liquid catalyst is activated, possessing a nucleation barrier, ΔG^*, of ~10-100 kJ/mol. This nucleation barrier reflects the non-wetting nature of AuSi-liquid on solid-Au, which results from the inequality $\gamma_{\text{sv}} < \gamma_{\text{sl}} + \gamma_{\text{lv}}$. Thus, a critical liquid height, h^*, must be exceeded before the liquid can be thermodynamically stabilized relative to the solid state. As a result, a solid catalyst may be kinetically trapped in the solid state even at temperatures well above T_{eu}, which enables and explains persistent VSS growth.

A brief pulse of HCl was found to reliably liquefy a solid catalyst at 390 °C, returning it to the VLS mechanism (*cf.* Fig. 4.1B). To probe this unexpected phenomenon, we attempted to measure the hysteresis data for NW growth in the presence of HCl by cooling below T_{eu}. As shown in Fig. 4.5A, we surprisingly observed no solidification of the catalyst at temperatures as low as 340 °C and instead observed continuous VLS growth and supercooling of the liquid catalyst by ~25 °C. Similar sub-eutectic VLS growth is known to occur when cooling Ge NWs grown with Au catalysts.[13] For Ge NWs, supersaturation and surface hydrogenation is thought to stabilize the catalyst in the liquid state.[13, 15]

We hypothesize that a similar effect stabilizes the liquid catalyst in our experiments. At the 340-400 °C temperatures used during NW growth, the Si NW and catalyst surface is expected to be chlorinated,[32] which could stabilize the catalyst, preventing a change in contact angle,[13] and create a diffusional barrier for Si species down the sidewall of the NW.[15] Additionally, the evaporation pathway will predominately involve $SiCl_x$ species, which have a lower vapor pressure compared to SiH_x species,[33-34] and thus should reduce the rate of evaporation. The cumulative effect is a higher concentration and supersaturation of Si in the catalyst, which stabilizes the liquid alloy.

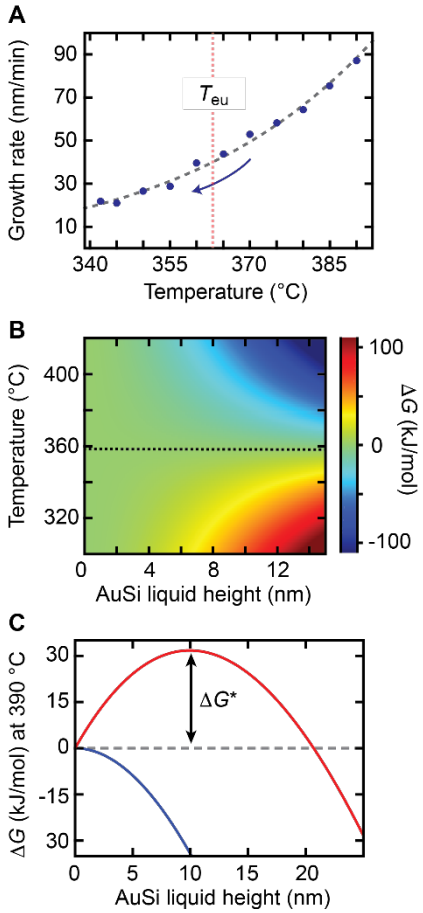

Figure 4.5: Catalyst liquefaction and sub-eutectic NW growth from surface chlorination

(A) NW growth rate as a function of temperature in the presence of HCl showing sub-eutectic Si NW growth. The catalyst becomes unstable and NW growth ceases below 340 °C. Dashed line is a fit to the Arrhenius equation, which produces an activation energy of 105 ± 8 kJ/mol. (B) Heatmap of ΔG during catalyst liquefaction in the presence of HCl as a function of temperature and the AuSi liquid height, h. Black dashed contour corresponds to $\Delta G = 0$. (C) ΔG during catalyst liquefaction at 390 °C as a function of the Au-Si liquid height, h, with HCl (blue trace) and without HCl (red trace).

For the catalyst to liquefy upon the introduction of HCl, the nucleation barrier that stabilizes the solid (*cf.* Fig. 4.3D) must be substantially lower. That energetic barrier originated from the non-wetting nature of liquid-AuSi on solid-Au. Thus, the rapid liquefaction upon introduction of HCl implies that the liquid alloy wets the solid-Au catalyst in the presence of HCl and that $\gamma_{sv} > \gamma_{sl} + \gamma_{lv}$, a reversal of the inequality observed without HCl. For our reaction conditions, γ_{ls} is unlikely to have changed because it corresponds to a buried interface and γ_{sv} is also unlikely to have changed because Cl is known to desorb from Au surfaces above ~360 °C [32]. Thus, the only surface energy likely to change as a result of surface chlorination is γ_{lv}, causing the reversal of the inequality.

We hypothesize Cl passivates the AuSi liquid surface and lowers γ_{lv}. Given the reversal of the surface energy inequality, we may place an upper bound on γ_{lv} of 0.45 J/m^2, which corresponds to the equality $\gamma_{sv} = \gamma_{sl} + \gamma_{lv}$. Fig. 4.5B depicts a heatmap of ΔG for liquefaction using eq. 1 at a range of T and h with the reduced γ_{lv}. In contrast to Fig. 4.3D, complete liquefaction of the catalyst is both spontaneous and barrierless for temperatures above ~360 °C.

The switching process illustrated in Fig. 4.1B can now be fully understood. As shown by the red curve in Fig. 4.5C, an energetic barrier to liquefaction of $\Delta G^* \approx 30$ kJ/mol is present in the absence of HCl, trapping the solid catalyst and explaining VSS growth above T_{eu}. Upon chlorination, the barrier disappears (blue curve in Fig. 4.5C), causing rapid liquefaction of the catalyst and returning NW growth to a VLS mechanism. When HCl is removed, the growth continues in the VLS mechanism, completing the reversible switch between liquid and solid catalysts, and VLS and VSS mechanisms.

4.4 Conclusion

In conclusion, we report a process that leverages the unique thermodynamics and kinetics

of the nanoscale catalyst-NW system to reversibly transition between a liquid and a super-heated solid catalyst under isothermal conditions above the T_{eu}. We also demonstrate the first instance of sub-eutectic VLS growth of Si NWs. These results add to the growing body of evidence that surface chemistry plays an integral role in controlling NW growth and should be considered equally alongside the bulk equilibrium phase diagrams when designing and optimizing NW growth conditions. Given the generality of the VLS mechanism, we anticipate that these results may be applied to other catalyst-NW systems, such as the growth of III-V or II-VI semiconductor NWs. Finally, this work demonstrates how the sometimes unexpected physics of nanoscale systems may be leveraged to develop new synthetic processes for nanoscale materials in emerging technologies.

4.5 Detailed Methods

4.5.1 Nanowire Growth and Etching

Nanowires (NWs) were grown in a hot-walled chemical vapor deposition system at 390 °C and 40 Torr total pressure in an atmosphere of H_2 except when noted otherwise in the manuscript. P dopant modulation during NW growth followed by post-growth etching produced diameter modulated regions, such as those in Fig. 4.1C, which were used to determine the NW growth rate. Additional details on the chemical vapor deposition system, NW growth, and NW etching may be found in ref. 20-22.

4.5.2 Electron Microscopy and Elemental Mapping

Samples for electron microscopy were prepared by drop-casting NWs directly on to lacey-carbon TEM grids (Ted-Pella #01895). STEM imaging was performed on a Tecnai Osiris operating at 200 kV with a sub-nm probe with a current of 1.5 nA (spot size 4, 3950k extraction voltage). Drift-corrected STEM-EDS maps were obtained using the Bruker Esprit software. The total collection times for each map were 15 minutes as longer collection times resulted in loss of

drift correction at high magnification. STEM images were obtained before and after map acquisition to note any change in the sample. The instrument resolution is ~5 angstroms. However, the final resolution of the elemental map in Fig. 4.2C is a convolution of the challenge of measuring the P signal, NW alignment relative to the electron beam, and the difficulty of drift correction on a featureless cylinder.

SEM imaging was performed with an FEI Helios 600 Nanolab dual beam system with an imaging resolution of less than 5 nm.

4.6 Thermodynamic Model of Catalyst-Nanowire System

Equation 1 from the main text describes the ΔG associated with phase and compositional changes in the catalyst-NW system. The free energy change was calculated using published thermodynamic data.[27] Specifically, the change in Gibbs free energy to create a given state when starting from the elemental solids was described using a simple substitutional model:

$$\Delta G_f (n_{Au}^L , n_{Si}^L , T) = n_{Au}^L \, {}^oG_{Au}^L + n_{Si}^L \, {}^oG_{Si}^L + \ldots$$
$$\left(n_{Au}^L + n_{Si}^L\right) RT(x_{Si} \, ln(x_{Si}) + x_{Au} \, ln(x_{Au})) + \left(n_{Au}^L + n_{Si}^L\right) \Delta^E G \, , \qquad \text{(eq. 4.3)}$$

where n_{Au}^L is the moles of liquid Au, n_{Si}^L is the moles of liquid Si, T is the absolute temperature, ${}^oG_{Au}^L$ is the Gibbs free energy of formation for liquid Au, ${}^oG_{Au}^L$ is the Gibbs free energy of formation for liquid Si, R is the ideal gas constant, x_{Si} is the mole fraction of Si, x_{Au} is the mole fraction of Au, and $\Delta^E G$ is the excess Gibbs free energy, which is given by a Redlich-Kister polynomial of the form:

$$\Delta^E G = x_{Au} x_{Si} \sum_{v=0}^{n} (x_{Au} - x_{Si})^v \, L_{Au,Si}^{(v)}(T) \, , \qquad \text{(eq. 4.4)}$$

where each coefficient, L, is a linear function of the temperature given by:

$$L_{Au,Si}^{(v)}(T) = a_{Au,\,Si}^{(v)} + b_{Au,\,Si}^{(v)} \, T \, , \qquad \text{(eq. 4.5)}$$

where the coefficients *a* and *b*, correspond to the excess enthalpy and entropy, respectively. The values of ${}^{o}G_{Au}^{L}$, ${}^{o}G_{Si}^{L}$, $a_{Au,\,Si}^{(v)}$, and $b_{Au,\,Si}^{(v)}$ were taken from ref. 27.

4.7 Thermodynamic Model of Catalyst Solidification

For solidification, our model considers the nucleation and growth of a solid Au nanoparticle as the Si content in a 100 nm diameter hemispherical liquid alloy catalyst is depleted. As illustrated in Fig. 4.3B, the solid particle is assumed to nucleate at the center of the catalyst-NW interface for simplicity. We calculate the change in Gibbs free energy to go from an undersaturated liquid alloy at the specified Si concentration to a liquid alloy and Au solid as a function of the solid nanoparticle radius.

The contributions from the various surface energies, γ_{sl}, γ_{lv}, and γ_{sv}, are also included in Equation 1 from the main text, but are insignificant relative to the free energies associated with the changes in composition/phase.[27, 35-37]

To produce the plots in Fig. 4.3B, we calculate the change in free energy as a function of solid particle size for a variety of starting Si concentrations in the liquid alloy using equation 1 from the main text with m = -1 and ignoring the surface term. This problem ultimately reduces to expressing n_{Au}^{L} as a function of the solid nanoparticle radius, r, then calculating $x_{Au}(r)$ and $x_{Si}(r)$ based on the initial amount of Si in the liquid alloy. For the simple hemispherical model we employed, this gives:

$$n_{Au}^{L}(r) = n_{Au}^{o} - \frac{2/3\pi r^{3}}{V_{m,Au}}, \qquad \text{(eq. 4.6)}$$

where n_{Au}^{o} is the initial amount of Au in the liquid catalyst and $V_{m,Au}$ is the molar volume of Au.

For each starting Si concentration, the amount of Au in the catalyst is the same, and for a given starting Si concentration the total amount of Au and Si is fixed. Thus, as the solid Au nanoparticle grows, the Si concentration in the liquid increases and returns the system closer to the

liquidus concentration, which leads to a $\Delta G < 0$ for Si concentrations below ~15%. As depicted in Fig. 4.3B, there exists a solid nanoparticle size for each starting concentration less than ~15% that produces a minimum in the ΔG vs. particle radius plot. This minimum corresponds to the Si concentration in the liquid alloy returning to the liquidus concentration. Once at the liquidus concentration, solidifying additional Au from the liquid supersaturates the alloy and increases the free energy of the system.

4.8 Thermodynamic Model of Catalyst Liquefaction

Our model of catalyst liquefaction considers the nucleation and growth of a liquid AuSi cap on a solid Au nanoparticle. The Gibbs free energy was calculated using equation 1 from the main text with $m = 1$. The surface energies (γ_{sl}, γ_{lv}, and γ_{sv}) used to calculate $\Delta G_{surface}$ were taken from the literature.[35-37] As illustrated in Fig. 4.3D of the main text, the liquid cap is assumed to nucleate at the tip of the catalyst for simplicity. We calculate the change in Gibbs free energy to go from a solid Au nanoparticle to a solid Au nanoparticle with a liquid alloy cap containing 18 atomic % Si of height, h, as a function of the liquid cap height and the temperature. Once again, this problem ultimately reduces to expressing n_{Au}^{L}, n_{Si}^{L}, and the various interfacial areas as a function of the liquid alloy cap height, h. The moles of Au and Si in the liquid cap are given by:

$$n_{Au}^{L}(h) = \frac{\pi h^2 (3R-h)}{3 V_{m\,Au}} x_{Au}\,, \qquad \text{(eq. 4.7)}$$

and

$$n_{Si}^{L}(h) = \frac{\pi h^2 (3R-h)}{3 V_{m,Si}} x_{Si}\,, \qquad \text{(eq. 4.8)}$$

where R is the catalyst radius, $V_{m,Au}$ is the molar volume of Au, x_{Au} is the mole fraction Au, $V_{m,Si}$ is the molar volume of Si, and x_{Si} is the mole fraction Si. Equation 4.2 describes how the interfacial areas scale with liquid cap height.

REFERENCES

1. Yin, Y.; Rioux, R. M.; Erdonmez, C. K.; Hughes, S.; Somorjai, G. A.; Alivisatos, A. P., Formation of Hollow Nanocrystals Through the Nanoscale Kirkendall Effect. *Science.* **2004,** *304* (5671), 711-714.

2. Beberwyck, B. J.; Surendranath, Y.; Alivisatos, A. P., Cation Exchange: A Versatile Tool for Nanomaterials Synthesis. *J. Phys. Chem. C* **2013,** *117* (39), 19759-19770.

3. Jacobsson, D.; Panciera, F.; Tersoff, J.; Reuter, M. C.; Lehmann, S.; Hofmann, S.; Dick, K. A.; Ross, F. M., Interface dynamics and crystal phase switching in GaAs nanowires. *Nature.* **2016,** *531* (7594), 317-322.

4. Kuykendall, T.; Ulrich, P.; Aloni, S.; Yang, P., Complete composition tunability of InGaN nanowires using a combinatorial approach. *Nat. Mater.* **2007,** *6* (12), 951-6.

5. Yang, C.; Zhong, Z. H.; Lieber, C. M., Encoding electronic properties by synthesis of axial modulation-doped silicon nanowires. *Science* **2005,** *310* (5752), 1304-1307.

6. Lu, W.; Lieber, C. M., Nanoelectronics from the bottom up. *Nat. Mater.* **2007,** *6* (11), 841-850.

7. Yan, R. X.; Gargas, D.; Yang, P. D., Nanowire photonics. *Nature Photon.* **2009,** *3* (10), 569-576.

8. Duan, X. F.; Huang, Y.; Agarwal, R.; Lieber, C. M., Single-nanowire electrically driven lasers. *Nature* **2003,** *421* (6920), 241-245.

9. Boukai, A. I.; Bunimovich, Y.; Tahir-Kheli, J.; Yu, J. K.; Goddard, W. A., 3rd; Heath, J. R., Silicon nanowires as efficient thermoelectric materials. *Nature* **2008,** *451* (7175), 168-71.

10. Hochbaum, A. I.; Chen, R.; Delgado, R. D.; Liang, W.; Garnett, E. C.; Najarian, M.; Majumdar, A.; Yang, P., Enhanced thermoelectric performance of rough silicon nanowires. *Nature* **2008,** *451* (7175), 163-7.

11. Kempa, T. J.; Cahoon, J. F.; Kim, S. K.; Day, R. W.; Bell, D. C.; Park, H. G.; Lieber, C. M., Coaxial multishell nanowires with high-quality electronic interfaces and tunable optical cavities for ultrathin photovoltaics. *P. Natl. Acad. Sci. USA* **2012,** *109* (5), 1407-1412.

12. Wagner, R. S.; Ellis, W. C., Vapor-Liquid-Solid Mechanism of Single Crystal Growth (New Method Growth Catalysis from Impurity Whisker Epitaxial + Large Crystals Si E). *Appl. Phys. Lett.* **1964,** *4* (5), 89.

13. Kodambaka, S.; Tersoff, J.; Reuter, M. C.; Ross, F. M., Germanium Nanowire Growth Below the Eutectic Temperature. *Science.* **2007,** *316* (5825), 729-732.

14. Gamalski, A. D.; Tersoff, J.; Sharma, R.; Ducati, C.; Hofmann, S., Formation of metastable liquid catalyst during subeutectic growth of germanium nanowires. *Nano Lett.* **2010,** *10* (8), 2972-6.

15. Sivaram, S. V.; Hui, H. Y.; de la Mata, M.; Arbiol, J.; Filler, M. A., Surface Hydrogen Enables Subeutectic Vapor-Liquid-Solid Semiconductor Nanowire Growth. *Nano Lett.* **2016,** *Article ASAP*, 10.1021/acs.nanolett.6b01640.

16. Panciera, F.; Chou, Y. C.; Reuter, M. C.; Zakharov, D.; Stach, E. A.; Hofmann, S.; Ross, F. M., Synthesis of nanostructures in nanowires using sequential catalyst reactions. *Nat. Mater.* **2015,** *14* (8), 820-5.

17. Wen, C. Y.; Reuter, M. C.; Bruley, J.; Tersoff, J.; Kodambaka, S.; Stach, E. A.; Ross, F. M., Formation of compositionally abrupt axial heterojunctions in silicon-germanium nanowires. *Science.* **2009,** *326* (5957), 1247-1250.

18. Wen, C. Y.; Reuter, M. C.; Tersoff, J.; Stach, E. A.; Ross, F. M., Structure, Growth Kinetics, and Ledge Flow during Vapor-Solid-Solid Growth of Copper-Catalyzed Silicon Nanowires. *Nano Lett.* **2010,** *10* (2), 514-519.

19. Chou, Y. C.; Wen, C. Y.; Reuter, M. C.; Su, D.; Stach, E. A.; Ross, F. M., Controlling the Growth of Si/Ge Nanowires and Heterojunctions Using Silver-Gold Alloy Catalysts. *ACS Nano* **2012,** *6* (7), 6407-6415.

20. Christesen, J. D.; Pinion, C. W.; Zhang, X.; McBride, J. R.; Cahoon, J. F., Encoding Abrupt and Uniform Dopant Profiles in Vapor-Liquid-Solid Nanowires by Suppressing the Reservoir Effect of the Liquid Catalyst. *ACS Nano* **2014,** *8* (11), 11790-11798.

21. Christesen, J. D.; Pinion, C. W.; Grumstrup, E. M.; Papanikolas, J. M.; Cahoon, J. F., Synthetically Encoding 10 nm Morphology in Silicon Nanowires. *Nano Lett.* **2013,** *13* (12), 6281-6286.

22. Pinion, C. W.; Nenon, D. P.; Christesen, J. D.; Cahoon, J. F., Identifying Crystallization- and Incorporation-Limited Regimes during Vapor-Liquid-Solid Growth of Si Nanowires. *ACS Nano* **2014,** *8* (6), 6081-6088.

23. Cohen-Karni, T.; Casanova, D.; Cahoon, J. F.; Qing, Q.; Bell, D. C.; Lieber, C. M., Synthetically Encoded Ultrashort-Channel Nanowire Transistors for Fast, Pointlike Cellular Signal Detection. *Nano Lett.* **2012,** *12* (5), 2639-2644.

24. Golovin, A. A.; Davis, S. H.; Voorhees, P. W., Step-flow growth of a nanowire in the vapor-liquid-solid and vapor-solid-solid processes. *J. Appl. Phys.* **2008,** *104* (7), 074301.

25. *Materials and methods are available in the supporting online material*.

26. Hui, H. Y.; Filler, M. A., Solid-Liquid-Vapor Etching of Semiconductor Nanowires. *Nano Lett.* **2015,** *15* (10), 6939-45.

27. Chevalier, P. Y., A thermodynamic evaluation of the Au-Ge and Au-Si systems. *Thermochim. Acta* **1989,** *141*, 217-226.

28. O'Toole, M.; Boland, J. J., A solid-liquid-vapor mechanism for anisotropic silicon etching. *Appl. Phys. Lett.* **2008,** *93* (26), 263107.

29. Xu, Q.; Sharp, I. D.; Yuan, C. W.; Yi, D. O.; Liao, C. Y.; Glaeser, A. M.; Minor, A. M.; Beeman, J. W.; Ridgway, M. C.; Kluth, P.; Ager, J. W.; Chrzan, D. C.; Haller, E. E., Large melting-point hysteresis of Ge nanocrystals embedded in SiO2 (vol 97, art no 155701, 2006). *Phys. Rev. Lett.* **2006,** *97* (20), 155701.

30. Mei, Q. S.; Lu, K., Melting and superheating of crystalline solids: From bulk to nanocrystals. *Prog. Mater. Sci.* **2007,** *52* (8), 1175-1262.

31. Couchman, P. R.; Jesser, W. A., Thermodynamic theory of size dependence of melting temperature in metals. *Nature* **1977,** *269* (5628), 481-483.

32. Kastanas, G. N.; Koel, B. E., Interaction of Cl2 with the Au(111) surface in the temperature range of 120 to 1000 K. *Appl. Surf. Sci.* **1993,** *64* (3), 235-249.

33. Jenkins, A. C.; Chambers, G. F., Vapor Pressures of Silicon Compounds. *Ind. Eng. Chem.* **1954,** *46* (11), 2367-2369.

34. Stull, D. R., Vapor Pressure of Pure Substances. Organic and Inorganic Compounds. *Ind. Eng. Chem.* **1947,** *39* (4), 517-540.

35. Cognard, J., Adhesion to gold: A review. *Gold Bull.* 1984, *17* (4), 131-139.

36. Naidich, Y. V.; Perevertailo, V. M.; Obushchak, L. P., Density and surface tension of alloys of the systems Au-Si and Au-Ge. *Sov. Powder Metall+* 1975, *14* (5), 403-404.

37. Naidich, Y. V.; Perevertailo, V. M.; Obushchak, L. P., Contact properties of the phases participating in the crystallization of gold-silicon and gold-germanium melts. *Sov. Powder Metall+* 1975, *14* (7), 567-571.

CHAPTER 5: HORIZONTAL SILICON NANOWIRES WITH RADIAL P-N JUNCTIONS: A PLATFORM FOR UNCONVENTIONAL SOLAR CELLS

5.1 Introduction

Nanostructured materials are the focus of most current efforts to design next-generation solar cells that could achieve high power conversion efficiencies at a relatively low total cost. These efforts include the development of organic bulk heterojunction devices,[1] dye-sensitized solar cells,[2] and quantum-dot solar cells.[3-7] As discussed in other recent perspectives,[1-7] the successful implementation of high-efficiency photovoltaic (PV) devices relies on careful design of the nanometer-scale morphologies and interfaces within these systems. The most unconventional devices aim to utilize third-generation solar cell concepts,[8] such as multiple exciton generation[4] (MEG) and hot carrier collection,[9] that would allow devices to exceed the Shockley-Queisser limit on power conversion efficiency.[10] For instance, a solar cell using PbSe quantum dots to enable MEG recently reported a quantum efficiency exceeding 100%.[11] Despite these promising research directions, no technology has been able to displace the reasonably good efficiency and low cost of conventional Si p-n junctions. In this perspective, we discuss the development of complex Si NWs as a technology that can combine the advantages of the well-known Si p-n junction with new materials and solar energy concepts, creating a new class of unconventional PV devices.

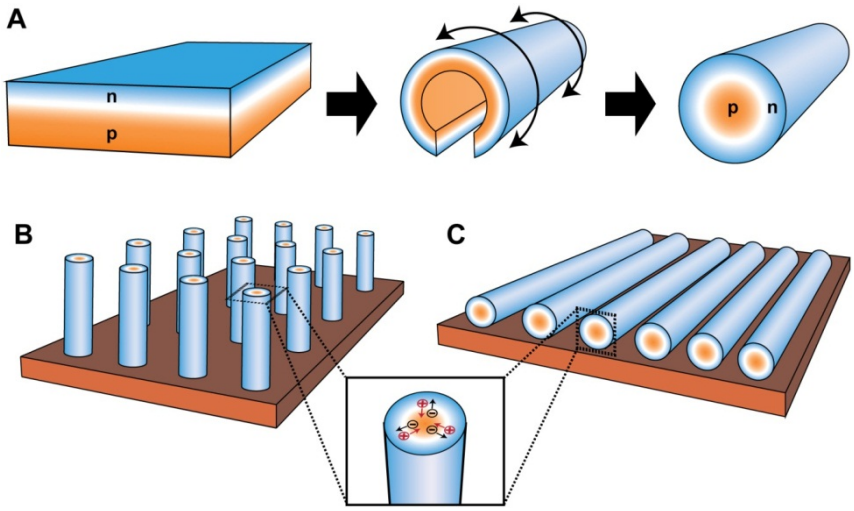

Figure 5.1: Overview of geometries used for semiconductor p-n junction PV devices

(A) Conventional planar p-n junction that can be conceptually rearranged into a cylindrical geometry to form a radial p-n junction NW (B) Wire-based PV device composed of vertically-oriented arrays that facilitate charge separation in the direction perpendicular to illumination (C) NW-based PV device composed of 200-300 nm diameter NWs oriented horizontally so NWs are illuminated perpendicular to the wire axis and charge separation occurs in the short, radial direction.

Semiconductor NWs have become a popular platform for the development of both PV and photoelectrochemical solar energy devices.[12-15] Conventional semiconductor PV devices are formed with planar p-type/n-type (p-n) homo- or hetero-junctions, and NW devices can be formed using the same junctions by rearranging the structure into a cylindrical geometry, as illustrated in Fig. 5.1A. The wire geometry can be formed using both bottom-up chemical synthesis,[16-18] such as VLS growth,[19] as well as top-down fabrication techniques,[20-21] such as lithographically-patterned deep reactive ion etching. These radial p-n junctions have been encoded in wires with diameters ranging from nanometers to microns and have been realized with a variety of

semiconductors, including groups II-VI, III-V, and IV materials such as CdS,[22-23] GaAs[24] or GaN,[25] and Si,[16-18, 21, 26-27] respectively. In this Chapter, we review the current paradigms for NW-based PV devices and provide our own perspective on how bottom-up synthesis and assembly of complex NW systems based on Si can be used as a transformative new platform for the development of next-generation, high efficiency PV structures.

The capability to separate the direction of light propagation from the direction of charge separation is one of the most frequently discussed motivations for developing wire-based PV structures, as illustrated in Fig. 5.1B. In this paradigm, the NW is oriented vertically such that illumination is parallel to the wire axis and charge carriers are separated in the perpendicular, radial direction. This geometry permits high performance to be realized even with low-quality, low-cost semiconductor materials if the wire diameter equals or is less than the minority carrier diffusion length of the material.[28] In addition, vertically-oriented arrays of wires have been shown to introduce anti-reflection, light scattering, and diffraction effects that enhance light absorption.[21, 29] For Si-based PV devices, this paradigm has led to the development of micron diameter wire arrays that approach the efficiency of conventional planar p-n junctions.[26-27] Here, we instead focus on a paradigm, illustrated in Fig. 5.1C, in which the NWs are oriented horizontally such that they are illuminated perpendicular to the wire axis. In this geometry, charge separation occurs in the short, radial direction and the NWs are illuminated uniformly along their total length. We also focus on mesoscopic NWs with diameters of 200-300 nm that are well-suited to exhibit unconventional effects related to their small size. We review the synthesis, electrical characteristics, and optical properties of the Si NW structures that can be used within this paradigm to create next-generation PV structures.

The construction of NW-based thin-film PV devices can be realized through the sequential

construction of increasingly complex device architectures, as depicted in Fig. 5.2. The simplest structures (top left, Fig. 5.2) are single-NW Si devices, which have the potential to meet high performance metrics, as discussed in the sections below. However, to move beyond these single Si structures, two parallel technologies must be developed. First, new strategies to design, synthesize, and fabricate advanced NW heterostructures that incorporate multiple components—semiconductors, dielectrics, and metals—can be developed to utilize advanced next-generation PV concepts[8] such as hot carrier collection,[9] multiple exciton generation,[4, 11] and surface plasmon mediated absorption enhancement.[30-33] Second, strategies to assemble, network, and integrate ensembles of individual NWs into one monolithic PV device can be developed to scale NW technology to large-area PV devices. These two directions can be pursued in parallel to develop next-generation devices based on Si NWs. Here, we primarily discuss the first challenge but note that there have been substantial advancements on the problem of NW directed- and self-assembly.[34-35]

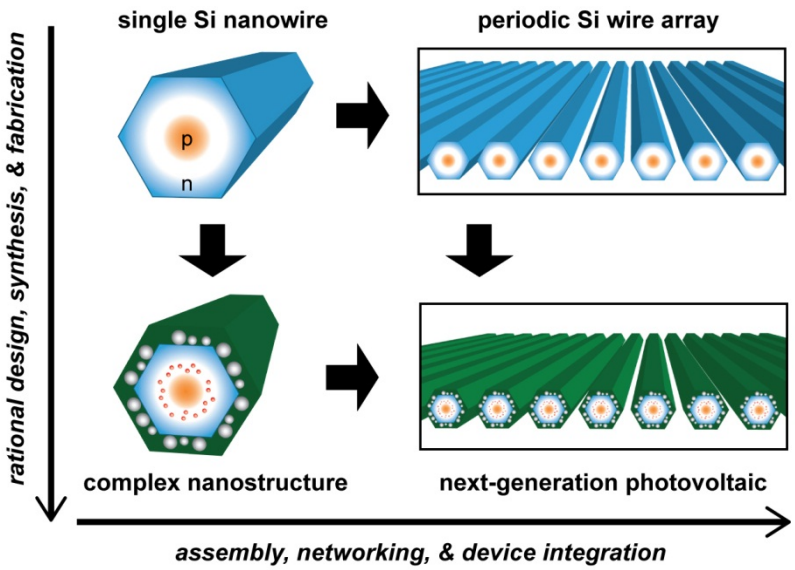

Figure 5.2: Overview of the general strategy for development of NW PV devices that use radial Si p-n junctions as the charge-separating scaffold for advanced solar cell architectures

Recently, well-controlled methods for bottom-up synthesis of Si NWs with radial p-n junctions have been developed,[16-18, 36] enabling synthesis of the high-quality core/shell PV NW structures illustrated in Fig. 5.3. In this approach, NWs are grown by a VLS mechanism using a metal nanoparticle to catalyze growth of p-type NW cores, as shown in the SEM image in Fig. 5.3B. Following core growth, intrinsic and n-type shells are sequentially grown by a vapor-solid (VS) mechanism to create core/shell p-type/intrinsic/n-type (p-i-n) PV structures, as shown in Fig. 5.3C. These core/shell structures exhibit faceted surfaces with an approximately hexagonal cross section (see Fig. 5.3D) that is indicative of a highly crystalline shell structure.[16] Details of the procedures used to synthesize NWs are provided in the Supporting Information (SI).

5.2 Experimental

To understand the potential PV performance of the core/shell p-i-n NW structures, we have used finite-element modeling to probe the electrical characteristics of the radial junctions. Building

on our previous modeling efforts,[17] we analyzed, as illustrated in Fig. 5.3E, the charge density, electric field, electrostatic potential, and internal quantum efficiency (IQE) values within the hexagonal cross section of the NWs. These simulation results demonstrate that with n- and p-type doping levels of 10^{18} cm^{-3} or larger, the ~250 nm diameter NW geometry yields well-defined depletion regions, intense built-in electric fields of ~10^7 V/m, and IQE values approaching unity throughout the structure. The high IQE values are a result of the short distance minority carriers must diffuse to reach the p-n junction (< 50 nm) as well as the short width (~40 nm) and high electric field strength within the intrinsic region. Interestingly, these short length scales and strong electric fields are sufficient to induce charge-carrier separation on ultrafast time scales of a picosecond or less (see Fig. 5.3). The combination of short length- and time-scales suggests that these NWs could be interesting structures to exploit unconventional third-generation PV concepts,[8] as discussed in sections below.

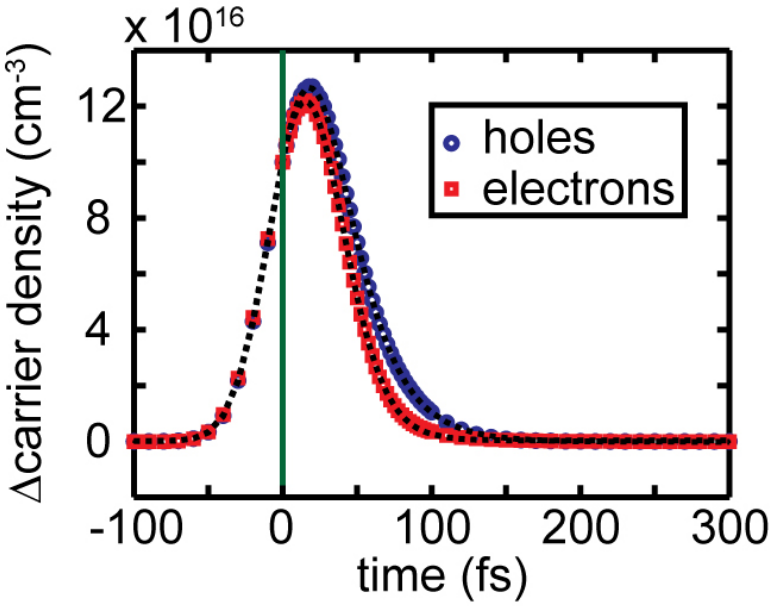

Figure 5.3: Time-scale of carrier separation in radial p-i-n devices

Simulation was performed by injecting 7 x 10^{17} carriers into the intrinsic region of the hexagonal 2D electrostatic simulation domain with a doping level of 1 x 10^{18} in both the p- and n-type regions using a Gaussian temporal profile with FWHM of 50 fs centered at time t=0. The carrier density in the intrinsic region was then monitored as a function of time. Plotted above is the difference in the carrier density at a specific time and the equilibrium carrier density in the intrinsic region. The black dotted lines represent fits from the convolution of a Gaussian with an exponential decay from which the extracted time constants for the exponential decay are 24 fs (15 fs) for holes (electrons). These times correspond to carrier velocities of ~10^{8} cm/s—an order of magnitude larger than the saturation drift velocity in Si. The physics employed in this time-dependent simulation do not take into account saturation effects, which allows such short separation times. Nonetheless, it is very reasonable to assume carrier separation occurs on a sub-picosecond time-scale given carriers would need to be drifting at less than 10^{6} cm/s in order to observe charge separation on time-scales greater than 1 ps.

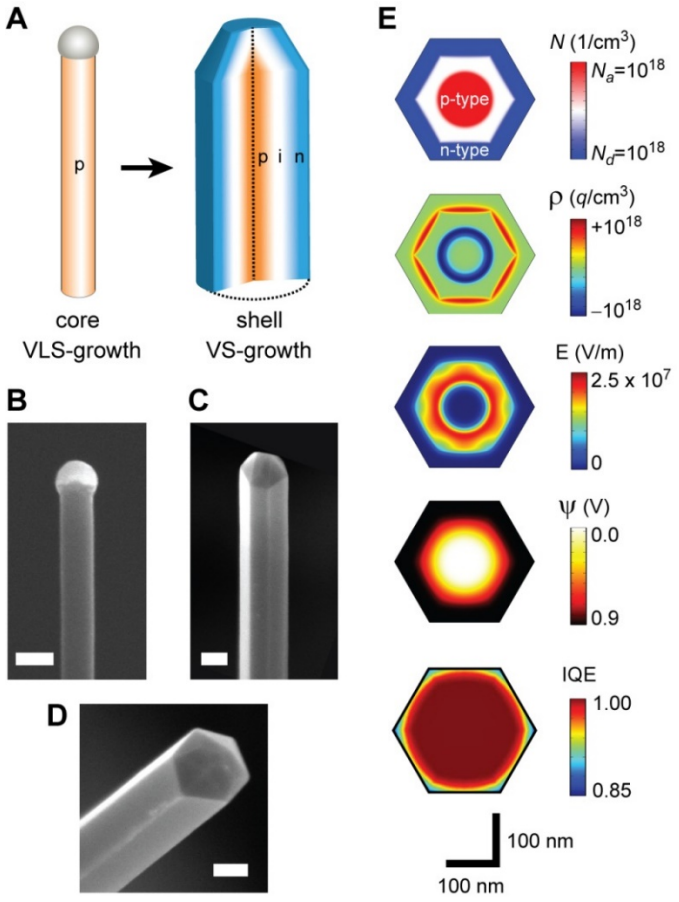

Figure 5.4: Synthesis and characteristics of core/shell p-i-n junction Si NWs

(**A**) Schematic of vapor-liquid-solid (VLS) growth of a p-type NW followed by vapor-solid (VS) growth of intrinsic and n-type shells to form p-i-n core shell/structures (**B**) SEM image of VLS-grown Si NW with an Au catalyst at the tip; scale bar, 100 nm (**C**) SEM image of a core/shell p-i-n NW; scale bar, 100 nm (**D**) End-on SEM image of a core/shell p-i-n NW showing a faceted, hexagonal shape with well-defined crystal planes; scale bar, 100 nm (**E**) Finite-element simulations of the core/shell p-i-n junction showing, from top to bottom, the doping distribution, N, charge density distribution ρ, electric field distribution, E, electrostatic potential, ψ, and internal quantum efficiency (IQE) under optical excitation. Simulations include Auger recombination, a surface recombination velocity of 10^5 cm/s, and a minority carrier lifetime of τ_{SRH} = 10 ns.

To experimentally evaluate the performance of the NWs, PV devices composed of single NWs have been fabricated following literature procedures.[16-17] An SEM image of a final device is depicted in Fig. 5.4A, which shows Ohmic metal contacts selectively defined to the p-type NW core and the n-type NW shell. As illustrated by the black curve in Fig. 5.4B, experimental current density-voltage (*J-V*) measurement on these single-NW devices under simulated 1-sun AM1.5G illumination yield *J-V* curves that are well fit to the ideal diode equation[37] and possess an open-circuit voltage (V_{OC}) of 0.485 V, fill-factor (FF) of 0.70, and short-circuit current density (J_{SC}) of 6.5 mA/cm^2. Note that J_{SC} values of up to ~10 mA/cm^2 have been reported for single nanowire devices[16-17] if they are coated with conformal dielectric shells,[38] as discussed in sections below.

5.3 Analysis and Discussion

To analyze the measured performance metrics, we have directly compared the experimental *J-V* curve to simulated *J-V* curves (red dashed lines in Fig. 5.5B) that include values for the Shockley-Read-Hall (SRH) minority carrier lifetime, τ_{SRH}, ranging from 1 ns to 1 μs.[17] The accuracy of the device simulations has been verified by the excellent agreement with experimental *J-V* curves[17] as well as by independent measurement of device metrics using ultrafast microscopy.[39] The simulated *J-V* curves indicate that the performance of the measured device is limited not by surface or Auger recombination processes but instead by a SRH minority carrier lifetime of τ_{SRH} = 10 ns.[17] While current device parameters fall short of bulk Si PV devices, if the minority carrier lifetime in the radial NWs can be improved by two orders of magnitude to 1 μs then the V_{OC} could be increased to values greater than 0.60 V. This value is comparable to those achieved in standard bulk Si solar cell modules. Recent experimental measurements have determined that minority carrier lifetimes exceeding 500 ns can be achieved in VLS-grown Si wires,[26] and experiments are in progress to achieve these values in radial p-i-n NWs.

To improve the 1-sun power conversion efficiency (η) of NW solar cells, it is also necessary to increase the J_{SC} of the devices by enhancing light absorption within the structures. In Fig. 5.5C, we project the η of NW devices for J_{SC} values ranging from 1 to 40 mA/cm^2. This projection demonstrates that with a J_{SC} of ~40 mA/cm^2, Si NW structures could achieve an η of ~16.7% with the current τ_{SRH} of 10 ns and an η of ~21.8% with an improved τ_{SRH} of 1 μs. Note that the upper limit on J_{SC} and η for Si under 1-sun illumination is ~42 mA/cm^2 and ~31%,[10] respectively; however, charge-carrier generation that utilizes unconventional third-generation PV concepts could potentially yield higher values, as discussed in sections below.

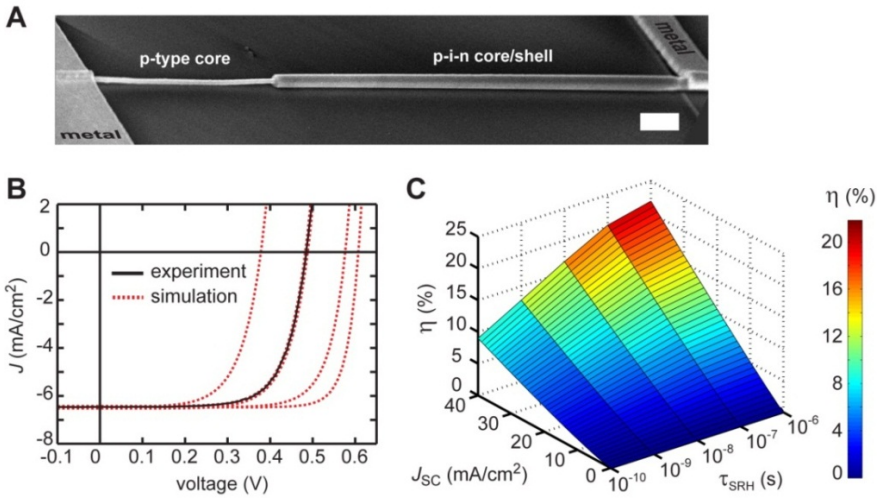

Figure 5.5: Performance of single core/shell p-i-n Si NW photovoltaic devices

(**A**) SEM image of a device showing selective metal contacts to the p-type core and n-type shell; scale bar, 1 μm (**B**) Experimental (black) and simulated (dashed red) *J-V* curves for NW devices under simulated 1-sun illumination. Simulation curves reflect, from left to right, minority carrier lifetimes of τ_{SRH} = 1, 10, 100, and 1000 ns, respectively, and all simulations include a surface recombination velocity of 100 cm/s. (**C**) Projected 1-sun power-conversion efficiency, η, for NW

devices with values of J_{SC} ranging from 0 to 40 mA/cm^2 and τ_{SRH} ranging from 100 ps to 1 μs including a surface recombination velocity of 100 cm/s.

To achieve enhanced light absorption in NW devices, the absorption characteristics of the structures can be controlled through careful modulation of shape and composition. Because the NWs are sub-wavelength in diameter, they behave as cavities that give rise to strong optical resonances,[36, 40] as illustrated by the finite-difference frequency-domain optical simulations in Fig. 5.6. In these simulations, 1-sun illumination is simulated with a vertically incident plane wave, which strongly interacts with the NWs at specific wavelengths, as exemplified in Fig. 5.6A. As reported previously,[16] these absorption modes can result in external quantum efficiency (EQE) values that exceed unity at specific diameters and wavelengths. This phenomena, termed an optical antennae effect, results from an absorption cross section that exceeds the physical cross section of the NW and is a unique feature of the sub-wavelength NW structures.[16, 36, 41] These resonances can be experimentally quantified by direct measurement of the EQE spectra of single-NW devices, as shown by the black curve in Fig. 5.6B (see section 5.5.5 for experimental details). The experimental EQE spectrum is in good agreement with optical simulations of the absorption efficiency, shown as the dashed red curve in Fig. 5.6B. The spectra show four prominent high-amplitude peaks, labeled 1-4, and the spatial absorption modes profiles for these peaks are illustrated in Fig. 5.6C. These profiles consist of complex modes that have attributes of both whispering gallery and Fabry-Perot optical resonances.[36] The spectral position and amplitude of these optical absorption resonances can be tuned throughout the visible wavelengths by subtle changes in the size and shape of the NW structure.[36] The alterations in shape—hexagonal, circular, or square—modify the wavelength and appearance of the absorption modes, as illustrated by a comparison of the modes in Figures 4C-E (also see Fig. 5.7 for full spectra for each geometry).

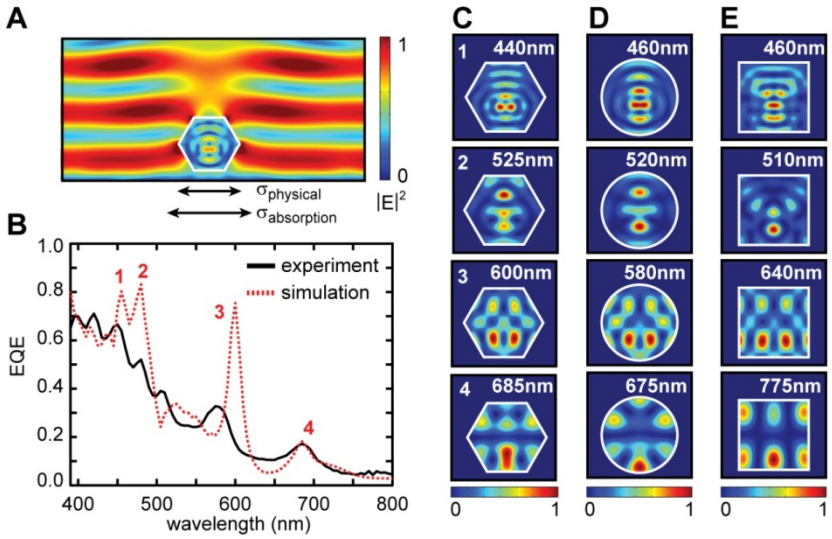

Figure 5.6: Optical absorption characteristics of individual Si NWs

(**A**) Normalized electric field ($|E|^2$) profile for an electromagnetic plane wave with a wavelength of 450 nm that is vertically incident on a single NW in which the absorption cross section ($\sigma_{absorption}$) exceeds the physical cross section ($\sigma_{physical}$) (**B**) Experimental (solid black) and simulated (dashed red) EQE spectra for a single Si NW with a diameter of 310 nm. (**C**) Resonant absorption mode profiles for the four peaks labeled 1-4 in panel B and a NW with hexagonal cross section (**D**) Absorption mode profiles for a NW with circular cross section (**E**) Absorption mode profiles for a NW with square cross section. For panels C-E, NW diameters (lateral widths) are 310 nm, the light polarization is transverse-electric (TE) for modes 1 and 3 and transverse-magnetic (TM) for modes 2 and 4, and the wavelength for each resonant mode is denoted in the top, right-hand corner of each image.

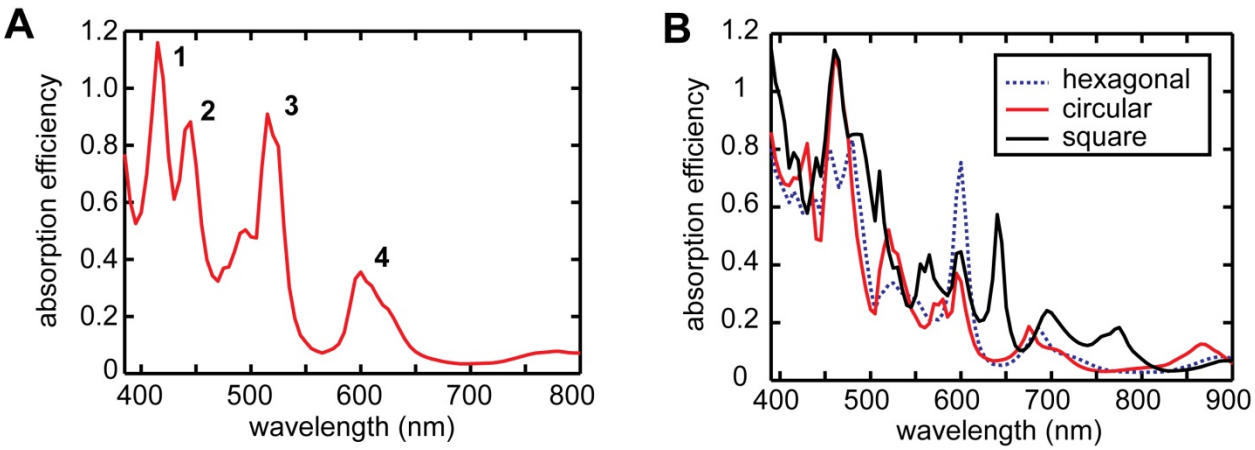

Figure 5.7: Absorption efficiency spectra of single NWs demonstrating EQE values greater than unity as a result of the optical antennae effect and effect of cross-sectional shape on NW absorption properties.

(A) Hexagonal NW with a diameter of 295 nm as is shown in Figure 4A. The solid red (solid black) trace in (B) corresponds to a NW with a circular (square) cross-section 310 nm in diameter (width). The dotted blue trace in (B) is the simulated spectra from Figure 5.6B with a hexagonal cross-section and 310 nm diameter.

To produce thin-film PV devices, the NWs can be arranged in periodic horizontal arrays as indicated in Fig. 5.2. As an instructive example, we consider here the simulated absorption efficiency of an array of 250 nm diameter Si NWs arranged with a pitch of 450 nm and a total areal filling fraction of ~55%, as shown in Fig. 5.8A. Despite the low filling fraction, the J_{SC} for this array, 6.26 mA/cm^2, is ~82% of the value for a single NW device and ~77% of the value for a close-packed array. To increase light absorption, individual NWs can be coated with dielectric shells[38] such as 50 nm thick Si_3N_4, and the array can be placed on a reflective substrate such as Ag. The addition of these two optical effects increases the J_{SC} value by ~72% to 10.78 mA/cm^2. As evident from a comparison of the absorption efficiency plots in Figure 5.8A, the improved J_{SC}

value is a result of both an increase in amplitude of nearly all absorption modes as well as the appearance of prominent absorption modes at longer wavelengths. The electric field profiles for two of these long-wavelength modes are illustrated in Fig. 5.8B, and these modes result from resonance effects from the reflective Ag substrate. Further design of complex reflective substrates and metallic nanostructures that support plasmon resonances[30-33] could be a promising direction to further boost light absorption within these NW structures using optical effects.

Despite the promising optical properties of Si NWs, the extent of light absorption in these PV structures will eventually be limited by the absorption coefficient of the material. This issue is a substantial limitation for Si because it is an indirect bandgap semiconductor. As a result, the typical thickness of a planar bulk Si solar cell is 100 microns or more in order to achieve complete absorption from the ultraviolet through near-infrared wavelengths. To overcome the limitations imposed by a single material, the Si NW structures can be blended with other semiconductors to form complex heterostructure or alloy materials. For instance, the Si shell can be alloyed with Ge to create Si_xGe_{1-x} structures in which the bandgap is continuously tunable between the value for Si, 1.12 eV, and Ge, 0.66 eV. Si_xGe_{1-x} alloys have been successfully used in multi-junction amorphous Si solar cell devices,[42] and the synthesis of crystalline Ge shells on Si NWs has been reported.[43-44] As illustrated in Fig. 5.9A, we consider here the incorporation of a 5-25 nm layer of crystalline $Si_{0.5}Ge_{0.5}$ alloy within the intrinsic region of the NW devices to create a Si/SiGe/Si core/shell/shell structure. Although the experimental implementation of this structure would require careful consideration of band alignments and band bending at the heterojunction, we assume for the purposes of this discussion that the devices would have an IQE of unity. As indicated by the absorption efficiency spectra in Fig. 5.9A, the presence of this thin layer substantially enhances the absorption efficiency for wavelengths greater than ~500 nm. The

incorporation of a 25 nm thick $Si_{0.5}Ge_{0.5}$ shell increases the J_{SC} of a single NW by 235% to a value of 18.0 mA/cm^2. If incorporated in the horizontal NW array discussed above, the Si/SiGe/Si NW would produce a J_{SC} value of 20.7 mA/cm^2. Thus, an alloyed NW structure represents a promising route to create a single-junction Si PV device that is not limited by the absorption characteristics of one material.

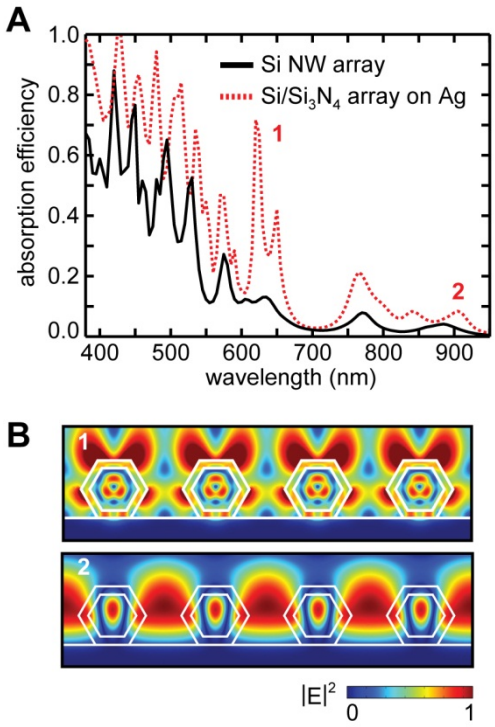

Figure 5.8: Optical absorption characteristics of extended arrays of Si NWs

(**A**) Absorption efficiency spectra of NWs on substrates composed of Si_3N_4 (black curve) and Ag (dashed red curve). Simulations reflect an infinite array of 250 nm diameter Si NWs with a gap of 200 nm between each wire (**B**) Normalized electric field ($|E|^2$) profiles for the absorption resonances labeled 1 and 2 in panel A.

There has also been widespread interest in the development of unconventional solar cell devices that could achieve high efficiencies by exploiting third generation solar cell concepts such as hot carrier collection and MEG.[8] In particular, research efforts have focused on the potential of semiconductor quantum dots (QDs) to facilitate efficient MEG processes.[4, 11] In the context of Si NWs, we suggest that QD materials such as PbS or PbSe could be embedded within the Si shell, as illustrated in Fig. 5.9B. QDs could be deposited on Si NWs by physical vapor deposition processes or, as recently reported, atomic layer deposition.[45] Experimental implementation of this structure would require careful consideration of the Si/chalcogenide interface to avoid recombination centers and diffusion of chalcogenide material into the Si NW. Depositing QD structures affords the two-fold advantage of introducing a direct bandgap semiconductor absorber as well as a material that could enable MEG effects. If embedded within the intrinsic region of core/shell p-i-n NWs, the strong built-in electric field of ~10^7 V/m, as illustrated in Figure 7B, could be used to rapidly and efficiently separate hot charge carriers within QDs on a sub-picosecond time scale.

If high-efficiency devices based on Si NWs with radial p-n junctions are developed, these materials might be most effectively used in a micro-concentrator solar cell design,[46] which would focus light onto a series of horizontal Si NW arrays. This design uses a lenticular lens composed of an array of cylindrical lenses to concentrate 1-sun illumination, as illustrated in Fig. 5.9C. For mild solar concentration, this design would represent an approximately ten-fold reduction in the amount of NW material needed to cover a macroscopic area. This design would also permit the fabrication of metal contacts to the NW p-type core and n-type shell that do not shadow the active, illuminated device region.

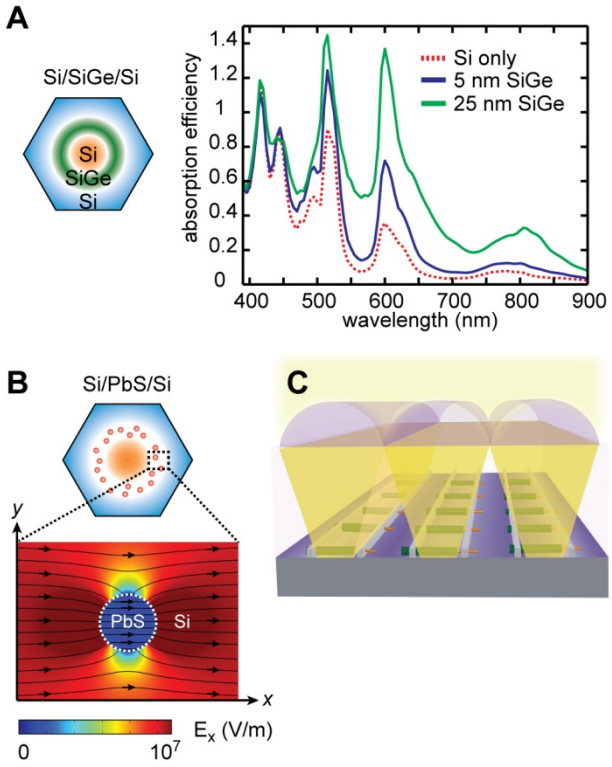

Figure 5.9: Concepts for PV devices using more complex nanostructures based on a Si NW platform

(A) Left, schematic of a core/shell Si NW in which the shell has been alloyed with Ge. Right, absorption efficiency spectra for NWs with no Ge (dashed red) as well as 5 nm (blue) and 25 nm (green) of $Si_{0.5}Ge_{0.5}$ alloy incorporated in the intrinsic region of the NW shell (B) Left, schematic of a core/shell Si NW in which PbS quantum dots have been embedded within the intrinsic region of the core/shell p-i-n Si NW structure. Right, plot of the electric field lines surrounding a quantum dot embedded in a Si NW (C) Schematic (not to scale) of a large-area micro-concentrator NW array PV device, which utilizes a lenticular lens array to focus incoming 1-sun radiation onto periodic horizontal arrays of NWs.

5.4 Conclusion

In this chapter, we have presented a new paradigm for NW-based solar energy devices that uses horizontal arrays of high-efficiency Si NW structures. In addition, we have summarized the synthetic methods to create these structures, analyzed the current and hypothetical performance of NW devices, evaluated the unique optical characteristics of the structures, and speculated about potential future structures that could exploit the novel features of NW systems. Substantial progress on the development of NW PV devices has been made over the last several years, and substantial work still remains to realize the full potential of these systems. The combination of material flexibility and unique optical characteristics makes Si NWs an exciting platform for the development of unconventional solar energy devices.

5.5 Detailed Methods

5.5.1 Hexagonal 2D Electrostatics Finite-Element Modeling

All finite-element modeling was implemented within the COMSOL Multiphysics 4.3 package.

The physics incorporated into the electrostatics model has been described in detail elsewhere. Briefly, the hexagonal cross-section of a NW was represented as a two-dimensional simulation domain. For each simulation point, we solved for the drift and diffusion of charge carriers in the presence of Shockley-Read-Hall, Auger, and surface recombination until converged points were found. The simulations account for band gap renormalization in degenerately doped Si with the associated effects on built-in voltage and intrinsic carrier concentration.

Unlike our previous modeling efforts, these simulations employ a 2D geometry without an axis of symmetry. In order to create external electrical connection to the p-type core a 10nm diameter circle was defined at the center of the wire in which a potential w.r.t ground could be

applied. Contact to the n-type shell was made through the top facet of the hexagonal geometry, which served as the ground electrode.

5.5.2 Optical Simulations

Absorption characteristics of both single NWs and NW arrays were simulated by impinging a normally incident plane wave with either transverse-electric (TE) or transverse-magnetic (TM) polarization. The absorption cross section at a particular wavelength was calculated by integrating the time-averaged electromagnetic power loss and dividing it by the time-averaged Poynting vector of the incident plane wave. The absorption cross section was then integrated over one optical cycle for each simulation element within the NW and the wavelength was scanned from 350nm to 1100nm in 5nm increments. The absorption efficiency at each wavelength was calculated as the NW absorption cross-section scaled by the NW physical cross-section. From the absorption efficiency the theoretical short-circuit current density at a particular wavelength was calculated as:

$$J_{SC}(\lambda) = \frac{(Abs.\ Eff.) * IQE * S(\lambda) * \lambda}{1.24}$$

where λ is the wavelength of the incident plane wave, IQE is the internal quantum efficiency of the device (assumed to be unity) and $S(\lambda)$ is the AM1.5 spectral irradiance at wavelength λ. Finally, the total J_{SC} was found by integrating $J_{SC}(\lambda)$ over the simulated wavelength range of 350nm to 1100nm. All simulations included a conformal 5nm SiO_2 layer over the NWs to represent a native oxide, unless noted otherwise. Non-reflective substrates consisted of a 600nm Si/100nm SiO_2/200nm Si_3N_4 wafer. Reflective substrates replaced the Si_3N_4 with Ag. For single NW simulations the entire simulation domain was wrapped in perfectly match layers (PMLs) to prevent scattering effects. NW arrays were simulated by employing periodic boundary conditions along the x-axis. For NW arrays the physical cross-section was taken to be the width of the simulation

domain for absorption efficiency and total J_{SC} calculations. Both the top and bottom of the simulation domain retained PMLs for the array simulations.

5.5.3 Si Nanowire growth

Radial p-type/intrinsic/n-type (p-i-n) NW structures were synthesized following a modification of literature procedures[47-48]. Au colloids (BBI International) with nanoparticle diameters of 100 nm were dispersed onto silicon oxide substrates (Nova Electronic Materials; p-type Si wafers with 600 nm thermal oxide) for NW growth by a vapor-liquid-solid (VLS) mechanism. The wafers were inserted into a single-zone quartz tube furnace (Lindbergh Blue M) with 1" bore. For radial p-i-n structures, the p-type NW core was grown at 460 ^{o}C and 40 Torr total reactor pressure for 150 min with 60 standard cubic centimeters per minute (sccm) H_2 (Matheson Tri-Gas; 5N semiconductor grade), 1 sccm SiH_4 (Voltaix) and 10 sccm B_2H_6 (Voltaix; 100 ppm in H_2). In the same reactor, the intrinsic shell was grown at 770 ^{o}C and 25 Torr for 25 min with 0.15 sccm SiH_4, followed by the n-type shell at the same temperature and pressure for 15 min with 0.15 sccm SiH_4 and 0.75 sccm PH_3 (Voltaix; 1,000 ppm in H_2). The growth chip was coated with 25 nm SiO_2 amorphous shell with Vision 310 Plasma Enhanced Chemical Vapor Deposition system (Advanced Vacuum) at 300 ^{o}C.

5.5.4 Device fabrication

NWs from the growth chip were transferred to the silicon-nitride wafers (Nova Electronic Materials; p-type Si wafers with 100 nm thermal oxide and 200 nm silicon nitride) as the device substrate. 500 nm of SU-8 2000.5 (MicroChem) was spin-coated on the device substrate, prebaked (95°C) and electron-beam lithography (EBL) was performed to define SU-8 etch masks on the NWs. The SU-8 was later postbaked (95°C), developed and hardbaked (185 °C) for 10 min. The device substrate was etched 30 s in Buffered Oxide Etchants (Transene) to remove the SiO_2 shell,

then immediately etched 10~18 s in potassium hydroxide (KOH 38 vol.% in water) at 60 ^{o}C to expose the core of the Si NWs outside of SU-8 masks. PMMA 950 A2 (MicroChem) photoresist was spin-coated on the device substrate and EBL and electron beam evaporation (Thermionics VE-100) was performed to lay down Ti/Pd (3/330 nm) metal contacts at the pressure of 5 x 10^{-8} Torr on the Si NWs core/shell region respectively.

5.5.5 Device measurements

Dark current-voltage (I-V) curves were measured using a Keithley 2636A SourceMeter in conjunction with Signatone micropositioners (S-725) and probe tips (SE-TL). *I-V* curves under 1-sun illumination were measured with the same SourceMeter and with metal contacts formed using a wire bonder (West Bond model 7476D) with 1% Si/Al wire. The solar simulator used for light measurements (Newport Oriel) contained an AM1.5G filter and was calibrated to 1-sun (100 mW/cm^2) using a calibrated reference solar cell (Newport, model 91150V).

The IPCE measurement was conducted using the following setup. Illumination was provided by a Newport 60100 Xenon Lamp (Oriel Instrument), combined with Cornerstone ™ 260 ¼ m grating monochromator (Newport). An orange filter with cutting wavelength at 570 nm was used when the illumination light wavelength was larger than 570 nm to eliminate the second order diffraction. A Glan Thompson uncoated calcite polarizer (Thorlabs GTH10M) was positioned after the filter to polarize the incident beam to obtain the polarization-resolved external quantum efficiency (EQE) spectra. The power density measurement of the illumination was performed by putting a spray-painted black aluminum sheet with 1/8 inch aperture before the UDT detector unit (UDT Instrument, UDT S370), where the illumination wavelength from 390 to 800 nm in 5 nm increments. The photocurrent data were collected by Keithley 2636A Dual-channel System SourceMeter Instrument. The TE and TM mode EQE were calculated by the photocurrent

collected described above and the projected area of the Si NWs were measured by FIB (Focus Ion Beam) Helios 600 Nanolab Dual Beam System (FEI). The area of the nanowire being illuminated was taken to be the entire exposed unetched shell region, excluding the 330 nm thick Ti/Pd metal covered contacts, when viewing from the normal direction to the plane of the chip substrate. The unpolarized EQE value was the averaged between the TM and TE mode EQE value.

REFERENCES

1. He, F.; Yu, L. P., How Far Can Polymer Solar Cells Go? In Need of a Synergistic Approach. *J. Phys. Chem. Lett.* 2011, *2* (24), 3102-3113.

2. Peter, L. M., The Gratzel Cell: Where Next? *J. Phys. Chem. Lett.* 2011, *2* (15), 1861-1867.

3. Kamat, P. V., Quantum Dot Solar Cells. The Next Big Thing in Photovoltaics. *J. Phys. Chem. Lett.* 2013, 908-918.

4. Beard, M. C., Multiple Exciton Generation in Semiconductor Quantum Dots. *J. Phys. Chem. Lett.* 2011, *2* (11), 1282-1288.

5. Toyoda, T.; Shen, Q., Quantum-Dot-Sensitized Solar Cells: Effect of Nanostructured TiO_2 Morphologies on Photovoltaic Properties. *J. Phys. Chem. Lett.* 2012, *3* (14), 1885-1893.

6. Mora-Seró, I.; Bisquert, J., Breakthroughs in the Development of Semiconductor-Sensitized Solar Cells. *J. Phys. Chem. Lett.* 2010, *1* (20), 3046-3052.

7. Hetsch, F.; Xu, X.; Wang, H.; Kershaw, S. V.; Rogach, A. L., Semiconductor Nanocrystal Quantum Dots as Solar Cell Components and Photosensitizers: Material, Charge Transfer, and Separation Aspects of Some Device Topologies. *J. Phys. Chem. Lett.* 2011, *2* (15), 1879-1887.

8. Green, M., A., *Third Generation Photovoltaics: Advanced Solar Energy Conversion*. Springer: Heidelberg, 2003.

9. Tisdale, W. A.; Williams, K. J.; Timp, B. A.; Norris, D. J.; Aydil, E. S.; Zhu, X. Y., Hot-Electron Transfer from Semiconductor Nanocrystals. *Science.* 2010, *328* (5985), 1543-1547.

10. Shockley, W.; Queisser, H. J., Detailed Balance Limit of Efficiency of p-n Junction Solar Cells. *J. Appl. Phys.* 1961, *32* (3), 510-519.

11. Semonin, O. E.; Luther, J. M.; Choi, S.; Chen, H. Y.; Gao, J. B.; Nozik, A. J.; Beard, M. C., Peak External Photocurrent Quantum Efficiency Exceeding 100% via MEG in a Quantum Dot Solar Cell. *Science.* 2011, *334* (6062), 1530-1533.

12. Kempa, T. J.; Day, R. W.; Kim, S.-K.; Park, H.-G.; Lieber, C. M., Semiconductor Nanowires: A Platform for Exploring Limits and Concepts for Nano-Enabled Solar Cells. *Energy Environ. Sci.* 2013, *6* (3), 719-733.

13. Garnett, E. C.; Brongersma, M. L.; Cui, Y.; McGehee, M. D., Nanowire Solar Cells. In *Annual Review of Materials Research, Vol 41*, Clarke, D. R.; Fratzl, P., Eds. Annual Reviews: Palo Alto, 2011, pp 269-295.

14. Hochbaum, A. I.; Yang, P. D., Semiconductor Nanowires for Energy Conversion. *Chem. Rev.* 2010, *110* (1), 527-546.

15. Peng, K. Q.; Lee, S. T., Silicon Nanowires for Photovoltaic Solar Energy Conversion. *Adv. Mater.* 2011, *23* (2), 198-215.

16. Kempa, T. J.; Cahoon, J. F.; Kim, S.-K.; Day, R. W.; Bell, D. C.; Park, H.-G.; Lieber, C. M., Coaxial Multishell Nanowires with High-Quality Electronic Interfaces and Tunable Optical Cavities for Ultrathin Photovoltaics. *Proc. Natl. Acad. Sci. U.S.A.* 2012, *109* (5), 1407-1412.

17. Christesen, J. D.; Zhang, X.; Pinion, C. W.; Celano, T. A.; Flynn, C. J.; Cahoon, J. F., Design Principles for Photovoltaic Devices Based on Si Nanowires with Axial or Radial p–n Junctions. *Nano Lett.* 2012, *12* (11), 6024-6029.

18. Tian, B. Z.; Zheng, X. L.; Kempa, T. J.; Fang, Y.; Yu, N. F.; Yu, G. H.; Huang, J. L.; Lieber, C. M., Coaxial Silicon Nanowires as Solar Cells and Nanoelectronic Power Sources. *Nature.* 2007, *449* (7164), 885-889.

19. Schmidt, V.; Wittemann, J. V.; Gosele, U., Growth, Thermodynamics, and Electrical Properties of Silicon Nanowires. *Chem. Rev.* 2010, *110* (1), 361-388.

20. Peng, K. Q.; Xu, Y.; Wu, Y.; Yan, Y. J.; Lee, S. T.; Zhu, J., Aligned Single-Crystalline Si Nanowire Arrays for Photovoltaic Applications. *Small* 2005, *1* (11), 1062-1067.

21. Garnett, E.; Yang, P. D., Light Trapping in Silicon Nanowire Solar Cells. *Nano Lett.* 2010, *10* (3), 1082-1087.

22. Fan, Z. Y.; Razavi, H.; Do, J. W.; Moriwaki, A.; Ergen, O.; Chueh, Y. L.; Leu, P. W.; Ho, J. C.; Takahashi, T.; Reichertz, L. A.; Neale, S.; Yu, K.; Wu, M.; Ager, J. W.; Javey, A., Three-Dimensional Nanopillar-Array Photovoltaics on Low-Cost and Flexible Substrates. *Nature Mater.* 2009, *8* (8), 648-653.

23. Tang, J.; Huo, Z.; Brittman, S.; Gao, H.; Yang, P., Solution-Processed Core-Shell Nanowires for Efficient Photovoltaic Cells. *Nat. Nanotechnol.* 2011, *6* (9), 568-572.

24. Colombo, C.; Heibeta, M.; Gratzel, M.; Fontcuberta i Morral, A., Gallium Arsenide p-i-n Radial Structures for Photovoltaic Applications. *Appl. Phys. Lett.* 2009, *94* (17), 173108.

25. Dong, Y.; Tian, B.; Kempa, T. J.; Lieber, C. M., Coaxial Group III-Nitride Nanowire Photovoltaics. *Nano Lett.* 2009, *9* (5), 2183-2187.

26. Kelzenberg, M. D.; Turner-Evans, D. B.; Putnam, M. C.; Boettcher, S. W.; Briggs, R. M.; Baek, J. Y.; Lewis, N. S.; Atwater, H. A., High-Performance Si Microwire Photovoltaics. *Energy Environ. Sci.* 2011, *4* (3), 866-871.

27. Putnam, M. C.; Boettcher, S. W.; Kelzenberg, M. D.; Turner-Evans, D. B.; Spurgeon, J. M.; Warren, E. L.; Briggs, R. M.; Lewis, N. S.; Atwater, H. A., Si Microwire-Array Solar Cells. *Energy Environ. Sci.* 2010, *3* (8), 1037-1041.

28. Kayes, B. M.; Atwater, H. A.; Lewis, N. S., Comparison of the Device Physics Principles of Planar and Radial p-n Junction Nanorod Solar Cells. *J. Appl. Phys.* 2005, *97* (11), 114302-11.

29. Kelzenberg, M. D.; Boettcher, S. W.; Petykiewicz, J. A.; Turner-Evans, D. B.; Putnam, M. C.; Warren, E. L.; Spurgeon, J. M.; Briggs, R. M.; Lewis, N. S.; Atwater, H. A., Enhanced Absorption and Carrier Collection in Si Wire Arrays for Photovoltaic Applications. *Nature Mater.* 2010, *9* (3), 239-244.

30. Ferry, V. E.; Munday, J. N.; Atwater, H. A., Design Considerations for Plasmonic Photovoltaics. *Adv. Mater.* 2010, *22* (43), 4794-4808.

31. Hägglund, C.; Apell, S. P., Plasmonic Near-Field Absorbers for Ultrathin Solar Cells. *J. Phys. Chem. Lett.* 2012, *3* (10), 1275-1285.

32. Atwater, H. A.; Polman, A., Plasmonics for Improved Photovoltaic Devices. *Nature Mater.* 2010, *9* (3), 205-213.

33. Cho, C. H.; Aspetti, C. O.; Turk, M. E.; Kikkawa, J. M.; Nam, S. W.; Agarwal, R., Tailoring Hot-Exciton Emission and Lifetimes in Semiconducting Nanowires via Whispering-Gallery Nanocavity Plasmons. *Nature Mater.* 2011, *10* (9), 669-675.

34. Long, Y. Z.; Yu, M.; Sun, B.; Gu, C. Z.; Fan, Z. Y., Recent Advances in Large-Scale Assembly of Semiconducting Inorganic Nanowires and Nanofibers for Electronics, Sensors and Photovoltaics. *Chem. Soc. Rev.* 2012, *41* (12), 4560-4580.

35. Wang, M. C. P.; Gates, B. D., Directed Assembly of Nanowires. *Mater. Today.* 2009, *12* (5), 34-43.

36. Kim, S.-K.; Day, R. W.; Cahoon, J. F.; Kempa, T. J.; Song, K.-D.; Park, H.-G.; Lieber, C. M., Tuning Light Absorption in Core/Shell Silicon Nanowire Photovoltaic Devices through Morphological Design. *Nano Lett.* 2012, *12* (9), 4971-4976.

37. Gray, J., L., The Physics of the Solar Cell. In *Handbook of Photovoltaic Science and Engineering*, Antonio Luque, S. H., Ed. 2004, pp 61-112.

38. Yu, Y.; Ferry, V. E.; Alivisatos, A. P.; Cao, L., Dielectric Core–Shell Optical Antennas for Strong Solar Absorption Enhancement. *Nano Lett.* 2012, *12* (7), 3674-3681.

39. Gabriel, M. M.; Kirschbrown, J. R.; Christesen, J. D.; Pinion, C. W.; Zigler, D. F.; Grumstrup, E. M.; Mehl, B. P.; Cating, E. E. M.; Cahoon, J. F.; Papanikolas, J. M., Direct Imaging of Free Carrier and Trap Carrier Motion in Silicon Nanowires by Spatially-Separated Femtosecond Pump–Probe Microscopy. *Nano Lett.* 2013, *13* (3), 1336-1340.

40. Cao, L.; White, J. S.; Park, J.-S.; Schuller, J. A.; Clemens, B. M.; Brongersma, M. L., Engineering Light Absorption in Semiconductor Nanowire Devices. *Nature Mater.* 2009, *8* (8), 643-647.

41. Cao, L. Y.; Fan, P. Y.; Vasudev, A. P.; White, J. S.; Yu, Z. F.; Cai, W. S.; Schuller, J. A.; Fan, S. H.; Brongersma, M. L., Semiconductor Nanowire Optical Antenna Solar Absorbers. *Nano Lett.* 2010, *10* (2), 439-445.

42. Reece, S. Y.; Hamel, J. A.; Sung, K.; Jarvi, T. D.; Esswein, A. J.; Pijpers, J. J. H.; Nocera, D. G., Wireless Solar Water Splitting Using Silicon-Based Semiconductors and Earth-Abundant Catalysts. *Science.* 2011, *334* (6056), 645-648.

43. Ben-Ishai, M.; Patolsky, F., A Route to High-Quality Crystalline Coaxial Core/Multishell Ge@Si(GeSi)$_n$ and Si@(GeSi)$_n$ Nanowire Heterostructures. *Adv. Mater.* 2010, *22* (8), 902-906.

44. Lauhon, L. J.; Gudiksen, M. S.; Wang, C. L.; Lieber, C. M., Epitaxial Core-Shell and Core-Multishell Nanowire Heterostructures. *Nature.* 2002, *420* (6911), 57-61.

45. Dasgupta, N. P.; Jung, H. J.; Trejo, O.; McDowell, M. T.; Hryciw, A.; Brongersma, M.; Sinclair, R.; Prinz, F. B., Atomic Layer Deposition of Lead Sulfide Quantum Dots on Nanowire Surfaces. *Nano Lett.* 2011, *11* (3), 934-940.

46. Yoon, J.; Baca, A. J.; Park, S. I.; Elvikis, P.; Geddes, J. B.; Li, L. F.; Kim, R. H.; Xiao, J. L.; Wang, S. D.; Kim, T. H.; Motala, M. J.; Ahn, B. Y.; Duoss, E. B.; Lewis, J. A.; Nuzzo, R. G.; Ferreira, P. M.; Huang, Y. G.; Rockett, A.; Rogers, J. A., Ultrathin silicon solar microcells for semitransparent, mechanically flexible and microconcentrator module designs. *Nature Mater.* 2008, *7* (11), 907-915.

47. Kempa, T. J.; Tian, B.; Kim, D. R.; Hu, J.; Zheng, X.; Lieber, C. M., Single and Tandem Axial p-i-n Nanowire Photovoltaic Devices. *Nano Letters* 2008, *8* (10), 3456-3460.

48. Kim, S.-K.; Day, R. W.; Cahoon, J. F.; Kempa, T. J.; Song, K.-D.; Park, H.-G.; Lieber, C. M., Tuning Light Absorption in Core/Shell Silicon Nanowire Photovoltaic Devices through Morphological Design. *Nano letters* 2012, *12* (9), 4971-6.

CHAPTER 6: CONCLUSION

6.1 Summary

This thesis focused on developing a detailed understanding of NW synthetic processes and physical properties to enable new NW-based technologies. To this end, we developed a bottom-up method that uses precise synthetic control and a selective chemical etch to encode morphology in Si NWs. Using this technique, morphological features as small as 10 nm were patterned over NWs more than 50 microns in length. After characterizing the NW growth rate and etch rate for various doping levels, we encoded a variety of shapes along the NW growth axis, such as nanorods, sinusoids, bow-ties, tapers, nanogaps, and gratings. We also demonstrated two distinct applications in the areas of resistive memory and plasmonics.

Next, our focus shifted to more fundamental studies of the VLS mechanism. To examine the rate-limiting step in the VLS mechanism, we collected a comprehensive set of Au-catalyzed Si NW growth rates over a range of temperatures, diameters, and pressures. To interpret this dataset, we developed a kinetic model of VLS growth that focused on the microscopic reactions of incorporation, evaporation, and crystallization. This simple model accurately explained our entire dataset and enabled the identification of two distinct regimes for VLS NW growth. Additionally, the kinetic model provided a framework for interpreting future studies on VLS and VSS NW growth.

While investigating the VLS mechanism, we noticed instances of unique catalyst behavior. Upon further study, we discovered that it is possible to instantaneously and reversibly switch the phase of the catalyst between a liquid and superheated solid state under isothermal conditions

above the eutectic temperature. To understand this unexpected phenomenon, we gathered experimental data on the hysteresis of NW growth kinetics as the temperature was cycled around the eutectic temperature and developed kinetic and thermodynamic models of catalyst solidification and liquefaction. We found the switching effect could be explained by the catalyst surface's ability to dictate the phase behavior in the catalyst-NW system.

Finally, we explored a promising application of NWs by investigating the potential for complex silicon nanowires with radial p-n junctions to serve as a platform for next-generation photovoltaic devices. Unique properties deriving from the NW geometry, such as optical antenna effects or ultrafast charge-carrier separation, make this a promising technology. Additionally, the precise synthetic control afforded by the VLS and VS growth mechanisms and other post-processing steps provide the flexibility to interface a variety of semiconductors, dielectrics, and metals to create a highly efficient photovoltaic device.

6.2 Future Work

6.2.1 Morphology Control: Si-Ge Heterostructures & Dry Etchants

The ENGRAVE technique described in Chapter 2 enables the fabrication of many exciting NW-based structures. However, the requirement of wet chemical etching severely limits the practical application of this technique to fabricate new NW-based technologies (even in a laboratory setting). Expanding the ENGRAVE technique to leverage dry etchants will circumvent many of the problems associated with a wet etchant, such as inhomogeneous etching, substrate effects (e.g. differences in etching on SiNx vs glass), or wire collapse/loss from capillary forces. Dry etchants also allow for etching immediately following NW growth to avoid exposure to ambient conditions.

Developing robust synthetic techniques for SiGe alloy heterostructures represents the most logical path to utilizing a dry etchant because all the necessary equipment and precursor gasses are available in the Cahoon lab. HCl gas, which is routinely utilized in the synthesis of Si NWs, is known to selectively etch Ge-rich SiGe alloys[1] and synthetic techniques for tuning the composition of SiGe NWs have been reported in the literature.[2-4] Moreover, SiGe alloys decouple the NW morphology from its doping profile without the requirement of additional processing steps (e.g. thermal oxidation). Decoupling morphology from doping will enable one to encode complementary electrical and morphological features along a NW, which should enable a wider variety of NW-based technologies.

6.2.2 Technological Applications: Si NW Thermoelectrics

Thermoelectric modules convert waste heat to usable electrical energy with an efficiency directly related to the thermoelectric figure of merit (*ZT*) of the materials comprising the module. *ZT* is a function of the materials electrical resistivity, thermal conductivity, Seebeck coefficient and absolute temperature (T). Despite being studied for over five decades, *ZT* values greater than 1 are difficult to achieve because the parameters comprising it are generally interdependent. The ideal thermoelectric material would be an 'electronic crystal', allowing excellent electrical conductivity, and a 'phonon glass', with poor lattice thermal conductivity to allow a larger temperature gradient to be maintained. With these concepts as guidelines, nano-structuring of thermoelectric materials has provided marked improvements in thermoelectric performance.[5] However, thermoelectric materials are typically comprised of heavy elements (Pb, Sb, Bi, Te, etc.) and require specialized processing, which prevents a scale-up to useful dimensions.

In contrast, Si is a ubiquitous semiconductor with a highly developed infrastructure. Bulk Si is known to be a poor thermoelectric material because of its high thermal conductivity arising

from a broad spectral distribution of phonons at elevated temperatures. This broad spectral distribution leads to acoustic phonons with long wavelengths and mean free paths. Thus, it stands to reason introducing phonon scattering elements at multiple length scales would decrease the thermal conductivity, thereby increasing *ZT*. Multiple examples of nanoscale Si with reduced thermal conductivity exist in the literature, with 'rough' or 'corrugated' Si NWs showing much promise.[6-10] Importantly, the rough NWs demonstrate high performance despite containing no rational design elements, with the exception of an intentionally roughened surface.

I propose to utilize the ENGRAVE technique introduced in Chapter 2 to encode rational morphologies at multiple length scales to serve as phonon-scattering elements in Si NWs. Utilizing ENGRAVE allows for the facile implementation of features as small as ~10nm over length scales exceeding 50 μm in both n-type and p-type Si NWs. In addition, the phonon-scattering elements utilized to reduce the thermal conductivity can be introduced while maintaining a high doping level ($>10^{18}$ cm^{-3}) throughout the entire NW, which ensures a high electrical conductivity. Finally, the ENGRAVE process naturally lends itself to both single NW studies for optimization of the morphology and macroscopic ($>cm^2$) device integration (*i.e.* arrays of epitaxial/vertical NWs).

Single NW devices to study the thermal properties of NWs have been reported,[8-9, 11-12] but are challenging to fabricate and often provide the 'device' thermal conductivity opposed to the NW thermal conductivity due to convolution from the external elements of the device (*e.g.* substrate effects, non-ohmic contacts). Recently, we reported an optical technique to characterize the thermal conductivity of individual Si NWs, which alleviates the problems deriving from an electrical measurement.[13] Combining this technique with standard procedures for measuring the electrical resistivity and Seebeck coefficient should allow for an accurate (and simple) determination of the NW thermoelectric performance.

In addition to developing an optimal Si NW thermoelectric material, the optical measurement technique could probe the general properties of heat transport in NWs. The literature in this area is surprisingly sparse. For instance, comprehensive studies on the effect of doping level, doping type, or NW diameter on thermal conductivity have yet to be reported. More advanced studies could probe the effect of rapid compositional changes on thermal transport (e.g. dopant modulation/band bending or Si/SiGe heterostructures).

REFERENCES

1. Bogumilowicz, Y.; Hartmann, J. M.; Truche, R.; Campidelli, Y.; Rolland, G.; Billon, T., Chemical vapour etching of Si, SiGe and Ge with HCl; applications to the formation of thin relaxed SiGe buffers and to the revelation of threading dislocations. *Semiconductor Science and Technology* 2005, *20* (2), 127-134.

2. Dailey, E.; Madras, P.; Drucker, J., Composition and growth direction control of epitaxial vapor-liquid-solid-grown SiGe nanowires. *Applied Physics Letters* 2010, *97* (14).

3. Potié, A.; Baron, T.; Latu-Romain, L.; Rosaz, G.; Salem, B.; Montès, L.; Gentile, P.; Kreisel, J.; Roussel, H., Controlled growth of SiGe nanowires by addition of HCl in the gas phase. *J Appl Phys* 2011, *110* (2), 024311.

4. Wu, Y.; Fan, R.; Yang, P., Block-by-Block Growth of Single-Crystalline Si/SiGe Superlattice Nanowires. *Nano Lett* 2002, *2* (2), 83-86.

5. Snyder, G. J.; Toberer, E. S., Complex thermoelectric materials. *Nat Mater* 2008, *7* (2), 105-14.

6. Park, K. H.; Martin, P. N.; Ravaioli, U., Electronic and thermal transport study of sinusoidally corrugated nanowires aiming to improve thermoelectric efficiency. *Nanotechnology* 2016, *27* (3).

7. Blanc, C.; Rajabpour, A.; Volz, S.; Fournier, T.; Bourgeois, O., Phonon heat conduction in corrugated silicon nanowires below the Casimir limit. *Applied Physics Letters* 2013, *103* (4).

8. Boukai, A. I.; Bunimovich, Y.; Tahir-Kheli, J.; Yu, J. K.; Goddard, W. A., 3rd; Heath, J. R., Silicon nanowires as efficient thermoelectric materials. *Nature* 2008, *451* (7175), 168-71.

9. Hochbaum, A. I.; Chen, R.; Delgado, R. D.; Liang, W.; Garnett, E. C.; Najarian, M.; Majumdar, A.; Yang, P., Enhanced thermoelectric performance of rough silicon nanowires. *Nature* 2008, *451* (7175), 163-7.

10. Zianni, X., Diameter-modulated nanowires as candidates for high thermoelectric energy conversion efficiency. *Applied Physics Letters* 2010, *97* (23), 233106.

11. Karg, S.; Mensch, P.; Gotsmann, B.; Schmid, H.; Das Kanungo, P.; Ghoneim, H.; Schmidt, V.; Bjork, M. T.; Troncale, V.; Riel, H., Measurement of Thermoelectric Properties of Single Semiconductor Nanowires. *Journal of Electronic Materials* 2013, *42* (7), 2409-2414.

12. Shi, L.; Li, D. Y.; Yu, C. H.; Jang, W. Y.; Kim, D. Y.; Yao, Z.; Kim, P.; Majumdar, A., Measuring thermal and thermoelectric properties of one-dimensional nanostructures

using a microfabricated device (vol 125, pg 881, 2003). *J. Heat Transfer.* 2003, *125* (6), 1209-1209.

13. Cating, E. E. M.; Pinion, C. W.; Van Goethem, E. M.; Gabriel, M. M.; Cahoon, J. F.; Papanikolas, J. M., Imaging Spatial Variations in the Dissipation and Transport of Thermal Energy within Individual Silicon Nanowires Using Ultrafast Microscopy. *Nano Lett* 2016, *16* (1), 434-439.